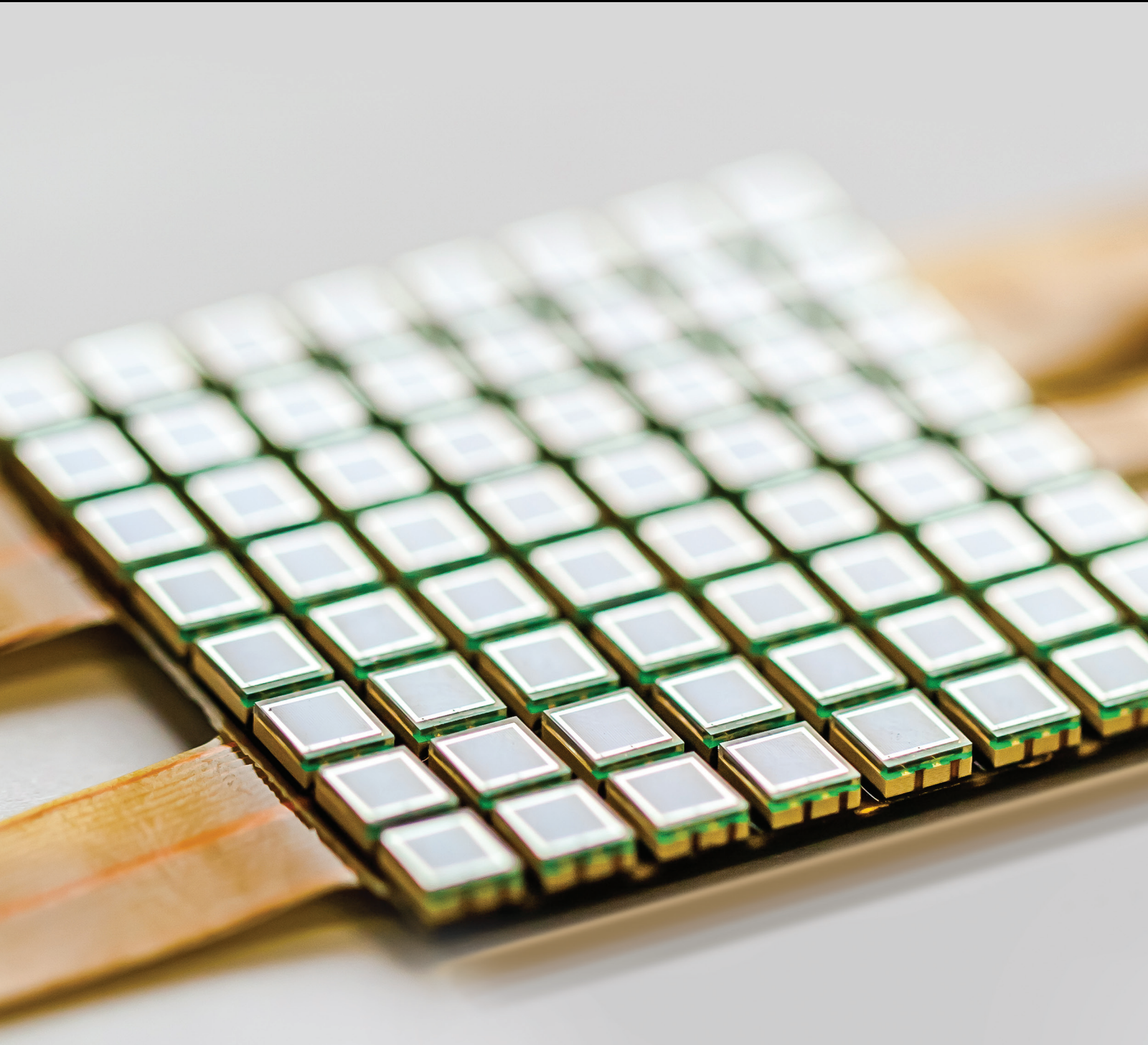


Sensors for Coastal Monitoring

Guest Editors: Francesco Serafino, Jochen Horstmann,
José Carlos Nieto Borge, Claudio Lugni, and Maurizio Brocchini





Sensors for Coastal Monitoring

Sensors for Coastal Monitoring

Guest Editors: Francesco Serafino, Jochen Horstmann,
José Carlos Nieto Borge, Claudio Lugni,
and Maurizio Brocchini



Copyright © 2016 Hindawi Publishing Corporation. All rights reserved.

This is a special issue published in "Journal of Sensors." All articles are open access articles distributed under the Creative Commons Attribution License, which permits unrestricted use, distribution, and reproduction in any medium, provided the original work is properly cited.

Editorial Board

Harith Ahmad, Malaysia
Francisco J. Arregui, Spain
Francesco Baldini, Italy
Fernando Benito-Lopez, Ireland
Romeo Bernini, Italy
Shekhar Bhansali, USA
Wojtek J. Bock, Canada
Hubert Brändle, Switzerland
Davide Brunelli, Italy
Belén Calvo, Spain
Stefania Campopiano, Italy
Jian-Nong Cao, Hong Kong
Sara Casciati, Italy
Chi Chiu Chan, Singapore
Nick Chaniotakis, Greece
Nicola Cioffi, Italy
Elisabetta Comini, Italy
Marco Consales, Italy
Jesus Corres, Spain
Andrea Cusano, Italy
Dzung V. Dao, Japan
Catherine Dehollain, Switzerland
Manel del Valle, Spain
Ignacio Del Villar, Spain
Utkan Demirci, USA
Junhang Dong, USA
Abdelhamid Errachid, France
Stephane Evoy, Canada
Vittorio Ferrari, Italy
Luca Francioso, Italy

Laurent Francis, Belgium
Mohammad Reza Ganjali, Iran
Wei Gao, Japan
Michele Giordano, Italy
Banshi D. Gupta, India
María del Carmen Horrillo, Spain
Wieslaw Jakubik, Poland
Hai-Feng Ji, USA
Kourosh Kalantar-Zadeh, Australia
Sher Bahadar Khan, KSA
Sang Sub Kim, Republic of Korea
Challa Kumar, USA
Hiroki Kuwano, Japan
Laura M. Lechuga, Spain
Chengkuo Lee, Singapore
Chenzhong Li, USA
Eduard Llobet, Spain
Yu-Lung Lo, Taiwan
Oleg Lupan, Moldova
Eugenio Martinelli, Italy
Jose R. Martinez-de Dios, Spain
Yasuko Y. Maruo, Japan
Mike McShane, USA
Igor L. Medintz, USA
Fanli Meng, China
Aldo Minardo, Italy
Joan Ramon Morante, Spain
Lucia Mosiello, Italy
Masayuki Nakamura, Japan
Marimuthu Palaniswami, Australia

Alberto J. Palma, Spain
Alain Pauly, France
Giorgio Pennazza, Italy
Michele Penza, Italy
Andrea Ponzoni, Italy
Biswajeet Pradhan, Malaysia
Ioannis Raptis, Greece
Christos Riziotis, Greece
Maria Luz Rodríguez-Méndez, Spain
Albert Romano-Rodriguez, Spain
Josep Samitier, Spain
Giorgio Sberveglieri, Italy
Luca Schenato, Italy
Michael J. Schöning, Germany
Andreas Schütze, Germany
Woosuck Shin, Japan
Pietro Siciliano, Italy
Vincenzo Spagnolo, Italy
Weilian Su, USA
Tong Sun, United Kingdom
Hidekuni Takao, Japan
Isao Takayanagi, Japan
Guiyun Tian, United Kingdom
Suna Timur, Turkey
Hana Vaisocherova, Czech Republic
Qihao Weng, USA
Matthew J. Whelan, USA
Stanley E. Woodard, USA
Hai Xiao, USA

Contents

Sensors for Coastal Monitoring

Francesco Serafino, Jochen Horstmann, José Carlos Nieto Borge, Claudio Lugni, and Maurizio Brocchini
Volume 2016, Article ID 1720563, 2 pages

Optimal Fair Scheduling in S-TDMA Sensor Networks for Monitoring River Plumes

Miguel-Angel Luque-Nieto, José-Miguel Moreno-Roldán, Javier Poncela, and Pablo Otero
Volume 2016, Article ID 8671516, 6 pages

A New Small Drifter for Shallow Water Basins: Application to the Study of Surface Currents in the Muggia Bay (Italy)

Carmelo Nasello and Vincenzo Armenio
Volume 2016, Article ID 6589636, 5 pages

Multifocus Color Image Fusion Based on NSST and PCNN

Xin Jin, Rencan Nie, Dongming Zhou, Quan Wang, and Kangjian He
Volume 2016, Article ID 8359602, 12 pages

Application of X-Band Wave Radar for Coastal Dynamic Analysis: Case Test of Bagnara Calabria (South Tyrrhenian Sea, Italy)

Michele Punzo, Chiara Lanciano, Daniela Tarallo, Francesco Bianco, Giuseppe Cavuoto, Rosanna De Rosa, Vincenzo Di Fiore, Giuseppe Cianflone, Rocco Dominici, Michele Iavarone, Fabrizio Lirer, Nicola Pelosi, Laura Giordano, Giovanni Ludeno, Antonio Natale, and Ennio Marsella
Volume 2016, Article ID 6236925, 9 pages

LG-Mod: A Modified Local Gradient (LG) Method to Retrieve SAR Sea Surface Wind Directions in Marine Coastal Areas

Fabio M. Rana, Maria Adamo, Guido Pasquariello, Giacomo De Carolis, and Sandra Morelli
Volume 2016, Article ID 9565208, 7 pages

Visibility of River Plume Fronts with an X-Band Radar

Satoshi Takewaka
Volume 2016, Article ID 6594847, 11 pages

Monitoring Individual Wave Characteristics in the Inner Surf with a 2-Dimensional Laser Scanner (LiDAR)

Kévin Martins, Chris E. Blenkinsopp, and Jun Zang
Volume 2016, Article ID 7965431, 11 pages

GNSS-R Delay-Doppler Map Simulation Based on the 2004 Sumatra-Andaman Tsunami Event

Qingyun Yan and Weimin Huang
Volume 2016, Article ID 2750862, 14 pages

Wave Height Estimation from Shipborne X-Band Nautical Radar Images

Xinlong Liu, Weimin Huang, and Eric W. Gill
Volume 2016, Article ID 1078053, 7 pages

Editorial

Sensors for Coastal Monitoring

**Francesco Serafino,¹ Jochen Horstmann,² José Carlos Nieto Borge,³
Claudio Lugni,⁴ and Maurizio Brocchini⁵**

¹*Institute for Electromagnetic Sensing of the Environment, CNR, Via Diocleziano 328, 80124 Naples, Italy*

²*Institute of Coastal Research, Helmholtz-Zentrum Geesthacht, Max-Planck-Straße, 121502 Geesthacht, Germany*

³*Universidad de Alcalá, Plaza de San Diego, s/n, 28801 Alcalá de Henares, Spain*

⁴*Marine Technology Research Institute, CNR, Via di Vallerano 139, 00128 Rome, Italy*

⁵*DICEA, Università Politecnica delle Marche, Via Brecce Bianche 12, 60131 Ancona, Italy*

Correspondence should be addressed to Francesco Serafino; serafino.f@irea.cnr.it

Received 3 March 2016; Accepted 3 March 2016

Copyright © 2016 Francesco Serafino et al. This is an open access article distributed under the Creative Commons Attribution License, which permits unrestricted use, distribution, and reproduction in any medium, provided the original work is properly cited.

The use of sensors for coastal monitoring is, nowadays, a very common and widespread practice due to their flexibility and capability of providing accurate and heterogeneous measurements of parameters that characterize the marine environment, even in the coastal area. Indeed, the capability of measuring coastal phenomena (waves, currents, plumes, morphology, etc.) in real time and with high accuracy makes these sensors extremely useful in improving the comprehension of the dynamic evolution of coastal phenomena. Examples are the proper understanding of the effects of severe weather conditions on the coastal morphodynamics and the real-time monitoring of the spill of pollutants.

In this theme issue, we have collected a series of works from international experts in their field, which describe advanced and innovative systems for coastal and riverine monitoring.

In the past, some significant works have summarized the state of the art in this field [1, 2]. However, the exponential growth of technology continuously provides new inputs and challenges towards the use of innovative and more accurate sensors, motivating the present issue. For the same reason, we have given main emphasis to the capability of the sensor technology rather than to the originality of the scientific contribution.

The paper entitled “Optimal Fair Scheduling in S-TDMA Sensor Networks for Monitoring River Plumes” proposes a scheduling procedure to obtain the optimal fair frame at the gateway of an underwater wireless sensor network to

be used in the monitoring of river plumes. Focus is on finding the theoretical maximum throughput by overlapping the transmissions of the nodes while keeping a balanced received data rate from each sensor of the network. Optimal performances are achieved if the gateway is at the center of the network; these decrease to 70% of the maximum normalized throughput if the gateway is at the edge of the network.

An investigation about a multifocus color image fusion algorithm based on nonsampled shearlet transform (NSST) and pulsed coupled neural networks (PCNN) is carried out in the contribution titled “Multifocus Color Image Fusion Based on NSST and PCNN.” The proposed algorithm is tested over a set of image couples and other, well assessed, algorithms, known in literature, are employed as benchmark; the proposed algorithm outperforms the traditional ones in terms of fusion performance.

The X-band radar technology has significantly contributed to providing a new insight in the real-time monitoring of sea waves, improving the ship navigation safety and the comprehension of medium-scale hydrodynamic phenomena.

The paper entitled “Visibility of River Plume Fronts with an X-Band Radar” investigates the opportunity to detect river plume fronts from marine X-band radar images. To this aim, a huge radar dataset acquired close to the mouth of the Tenryu river, in Japan, has been compared with a number of satellite and in situ datasets to prove the visibility of plume fronts in radar acquisitions. In addition, the author provides the results of a statistical analysis, which involves the “intensity” of river

plume fronts in radar data, the local wind vector, and the local water level, to assess the “detectability” of the plume fronts as function of the environmental conditions.

The published paper “Application of X-Band Wave Radar for Coastal Dynamic Analysis: Case Test of Bagnara Calabria (South Tyrrhenian Sea, Italy)” illustrates the applicability of conventional X-band marine radars to analyse the behaviour of waves in coastal waters. The analysis carried out in this work permits identifying the spatiotemporal evolution of incoming waves in coastal waters, including the local wave height, as well as identifying the rip currents as a result of the analysis. Using a different remote sensing sensor, the paper “Monitoring Individual Wave Characteristics in the Inner Surf with a 2-Dimensional Laser Scanner (LiDAR)” shows the use of a two-dimensional laser scanner (LiDAR), which operates in the optical domain of the electromagnetic spectrum, rather than the X-band, which works in the microwave range, to derive individual wave features and their temporal evolution. The work has been applied in the inner surf and swash zones of a microtidal beach. Parameters, such as wave height, wave periods, and wave celerity, are obtained with this technique. The paper “LG-Mod: A Modified Local Gradient (LG) Method to Retrieve SAR Sea Surface Wind Directions in Marine Coastal Areas” applies the Synthetic Aperture Radar system on board the ESA-Envisat satellite (ASAR) to derive wind directions in coastal areas. The proposed method to retrieve winds is based on the computation of local gradients over quasilinear and quasiperiodic structures detected by SAR imagery. The proposed wind estimation model is validated against in situ coastal wind measurements provided by anchored buoys with 63 Envisat ASAR images.

In the paper “GNSS-R Delay-Doppler Map Simulation Based on the 2004 Sumatra-Andaman Tsunami Event,” a new method for simulating Global Navigation Satellite System-Reflectometry Doppler maps is presented to analyse tsunami-dominant sea surfaces. The technique uses a Cox and Munk based model. The feasibility of Cox and Munk model under the tsunami scenario is compared with measurements having a correlation coefficient of 0.93. The analysis carried out in the work may permit retrieving in the future tsunami parameters using the techniques explained in the paper. Using different techniques, the paper “A New Small Drifter for Shallow Water Basins: Application to the Study of Surface Currents in the Muggia Bay (Italy)” uses Lagrangian drifters to analyse surface currents for coastal areas under different meteorological conditions. This paper describes a small drifter prototype that transmits its GPS location via GSM phone network. From the trajectories of the drifters, the local currents are derived; that analysis includes additional information, such as the surface circulation.

The manuscript “Wave Height Estimation from Shipborne X-Band Nautical Radar Images” describes some improvements of a shadowing-analysis-based algorithm for the wave height estimation from X-band radar images acquired from a radar on a moving ship. The algorithm involves first the extraction of the shadowed areas from radar images through an edge detection technique. Then, using the calculated illumination ratios in local areas, the root mean square (RMS) surface slope is derived by a curve fitting Smith’s

function. Finally, the significant wave height is estimated from the RMS surface slope and the average zero-crossing wave period.

This theme issue is a good opportunity for the interested readers to be updated on the most recent results of the research in the field of coastal monitoring achieved and described by the researchers who contributed to such research.

*Francesco Serafino
Jochen Horstmann
José Carlos Nieto Borge
Claudio Lugni
Maurizio Brocchini*

References

- [1] T. J. Malthus and P. J. Mumby, “Remote sensing of the coastal zone: an overview and priorities for future research,” *International Journal of Remote Sensing*, vol. 24, no. 13, pp. 2805–2815, 2003.
- [2] V. Klemas, “Remote sensing of coastal and ocean currents: an overview,” *Journal of Coastal Research*, vol. 28, no. 3, pp. 576–586, 2012.

Research Article

Optimal Fair Scheduling in S-TDMA Sensor Networks for Monitoring River Plumes

Miguel-Angel Luque-Nieto, José-Miguel Moreno-Roldán, Javier Poncela, and Pablo Otero

Departamento Ingeniería de Comunicaciones, University of Málaga, 29010 Málaga, Spain

Correspondence should be addressed to Miguel-Angel Luque-Nieto; luquen@uma.es

Received 24 September 2015; Revised 26 January 2016; Accepted 7 February 2016

Academic Editor: Maurizio Brocchini

Copyright © 2016 Miguel-Angel Luque-Nieto et al. This is an open access article distributed under the Creative Commons Attribution License, which permits unrestricted use, distribution, and reproduction in any medium, provided the original work is properly cited.

Underwater wireless sensor networks (UWSNs) are a promising technology to provide oceanographers with environmental data in real time. Suitable network topologies to monitor estuaries are formed by strings coming together to a sink node. This network may be understood as an oriented graph. A number of MAC techniques can be used in UWSNs, but Spatial-TDMA is preferred for fixed networks. In this paper, a scheduling procedure to obtain the optimal fair frame is presented, under ideal conditions of synchronization and transmission errors. The main objective is to find the theoretical maximum throughput by overlapping the transmissions of the nodes while keeping a balanced received data rate from each sensor, regardless of its location in the network. The procedure searches for all cliques of the compatibility matrix of the network graph and solves a Multiple-Vector Bin Packing (MVBPP) problem. This work addresses the optimization problem and provides analytical and numerical results for both the minimum frame length and the maximum achievable throughput.

1. Introduction

River-fed sediment plumes in estuaries and deltas are important to be monitored, because of their influence on water quality and the environment. The techniques employed to monitor nearshore environments can be classified into two main categories: remotely and in situ methods. For remote sensing, satellite devices (AVHR Radiometer [1], images from MODIS-Aqua [2]) or unmanned aerial vehicles [3] have been used. In situ measurements can be taken by means of underwater sensors (i.e., river drifters [4] or video remote sensing [5]). Underwater Wireless Sensor Networks (UWSNs) are a very promising and convenient instrument in oceanography, in particular for pollution monitoring and offshore exploration [6]. Sediment plumes may show different patterns due to currents and wind. Figure 1 presents a possible deployment of UWSN, intended to cover the area of interest. There are two types of nodes in the network: sensor and sink nodes. Sink nodes collect data from sensor nodes and serve as network gateways. The shallow water acoustic channel is highly hostile. Therefore, the choice of an

efficient MAC protocol is essential to the design of UWSN [7]. Two multihop transmission mechanisms from sensors to sink nodes are possible: broadcast or point-to-point. The latter is the chosen option for the present work. Concerning the choice between channel-partitioning or random access protocols [8, 9], time-division multiplexing (TDM) is the preferred technique, because of its simplicity and power efficiency. To overcome the limited throughput, Spatial Time-Division Multiple Access (STDMA), which is a collision-free multihop channel access protocol [10], is used in the present work.

Since all node locations are equally important in terms of data acquisition, transmission fairness [11] is a scheduling objective. In this analysis, fairness means that all nodes transmit the same amount of their own data in the long-term, regardless of their distance from the sink node.

In this paper, a network with a single sink will be analyzed. Two different gateway locations are considered and it will be shown how its location has a strong influence on the network throughput. Previous works by other authors deal with fairness scheduling in STDMA networks. Wang et al.

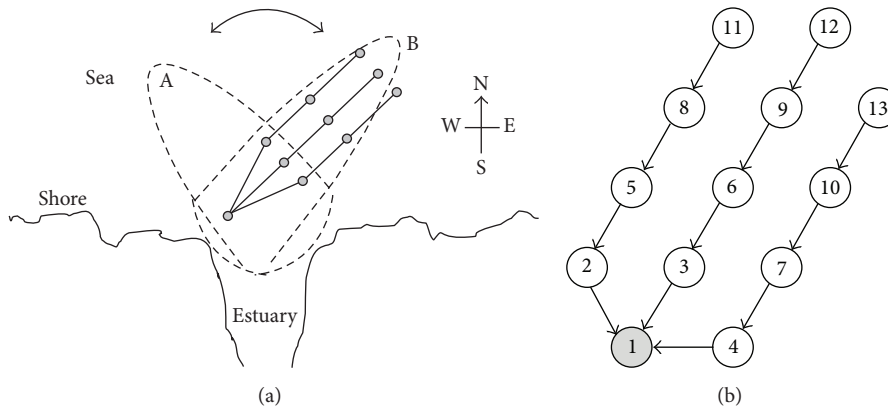


FIGURE 1: (a) Area of interest in an estuary: with West drift (A) or East drift current (B). (b) Proposed topology of a network with one gateway and 12 sensor nodes covering the area of interest (labeled B, in case (a)).

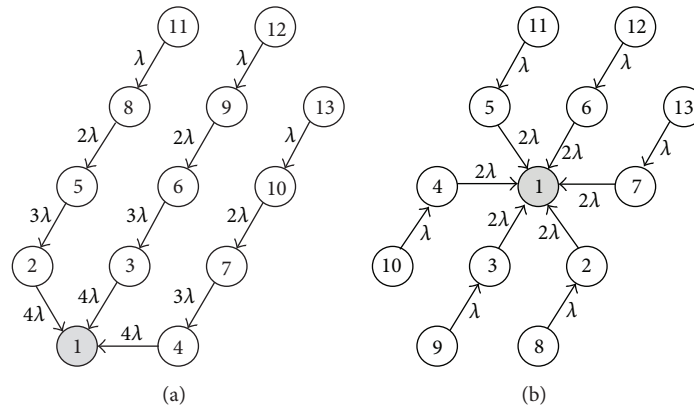


FIGURE 2: Example of network with twelve sensors: topology and throughput. Gateway node is node 1, in the gray circle, in both cases. Other nodes are clockwise numbered. (a) Gateway on the corner. (b) Gateway in the center.

proposed a scheduling algorithm, but they emphasized adaptive scheduling instead of shortest frame [12]. Concerning UWSNs, Diamant and Lutz proposed STDMA protocol for ad hoc UWSNs where fairness was considered but not uniformly achieved [13]. Chitre et al. demonstrated that the optimal schedule for random networks is periodic and presented a computationally efficient algorithm that finds good schedules [14] while our work presents a new procedure that finds the optimal scheduling when the location of the nodes is known. Xiao et al. also presented an algorithm to find optimal scheduling in TDMA networks, but only for linear (one-row) topology in UWSNs [15]. Our procedure determines the optimal fair scheduling for the case of saturated load condition (i.e., the sensor nodes have always data to transmit) in a network where the topology follows the estuary shape. Analytical expressions for the frame length and numerical results for the throughput are presented as well.

2. Network Description and Scheduling

Before analyzing in depth the STDMA network scheduling, some aspects should be considered. In the network topology shown in Figure 1(b) the nodes are located at the vertex of

an equilateral triangular mesh, and they are stationary. Two possible gateway locations are shown in Figure 2: gateway on the corner and in the center. The main reason to consider these two locations is that they are the two limiting cases for performance and cost of the network deployment. If a network with a central gateway is chosen, the maximum throughput is obtained at the expense of a higher cost, due to the larger distance from the gateway to the shore.

As the word indicates, a plume has the shape of a large feather; that is, it covers an area longer than wide, as shown in Figure 1(a). To fit this area of interest, the chosen network topology consists of three or six (depending on the gateway position) strings coming together to the gateway. Figure 2 also shows the throughput of every node in a 13-node network (12 sensor nodes and a gateway). Neighbor nodes are in the transmission range from each other, and nonadjacent nodes are not, because of transmission power control [15]. Transmit mode is simplex; that is, a node that is transmitting does not receive simultaneously, and vice versa. After an initial synchronization phase, the forwarding table (shown by the arrows in Figure 2) will be set and will remain static.

The amount of data acquired by sensors makes that every node always has a packet ready for transmission

(saturated load condition). Time is divided into equally long slots. Long propagation delays of acoustic waves and the associated spatiotemporal uncertainty are taken into account when considering a time slot that includes not only the transmission time but also the propagation time and a guard time. When a node transmits, it does so at a constant binary rate: the channel data rate, R_b , equal for all nodes. A fair frame is defined as the set of slots needed for all nodes to successfully send one and only one packet of its own data to the gateway. Thus, network operation is periodic, the period being the frame duration. Simultaneous transmissions are allowed, in order to minimize the frame length. This is the benefit of Spatial TDMA [10].

TDMA scheduling is the assignment of slots to nodes in order to find a suitable periodic frame. In TDMA scheduling, two types of assignments are possible: node-oriented [16] and link-oriented [17]. In acoustic networks, when transducers (projectors and hydrophones) are not directional, the node-oriented assignment is recommended. The first step in STDMA scheduling is to determine the compatible nodes, which are those nodes that can transmit simultaneously without causing any intranet interference. There are two possible types of transmission incompatibilities [17]: type 1 occurs when a node transmits while its neighbors in the same string are transmitting too; type 2 occurs when a node simultaneously receives from two, or more, different transmitting nodes. Scheduling will cope with the incompatibilities in the network. The next step for the STDMA scheduling is to find the shortest fair frame. This requires solving an optimization problem under two constraints: (i) only compatible nodes can be planned in the same slot and (ii) the number of transmissions of every node must fulfill a fairness operation in the network.

3. Fair Frame Optimization

This section details the proposed algorithm to find the optimal fair frame. Let N be the number of sensor nodes (labeled $2, \dots, N+1$; node 1 is the gateway), let λ_0 be the throughput of a single node, and let λ_i be the aggregated throughput of node i , that is, the throughput due to the data collected by node i plus the data received from upstream nodes and forwarded by node i . A frame is a particular set of z time slots, where every slot may contain simultaneous transmissions of compatible nodes. In order to set a fair behavior in the network, the gateway should have received exactly λ_0 from each node of the network by the end of the frame. This constraint forces a number of transmissions t_i for every node i in the frame, given by set $T = \{t_2, t_3, \dots, t_{N+1}\}$. For instance, in Figure 2(a), $T = \{4, 4, 4, 3, 3, 3, 2, 2, 2, 1, 1, 1\}$. The procedure used to find the shortest fair frame consists of two steps: (A) look for all sets of compatible nodes and (B) formulate and solve the combinatorial optimization problem to find the shortest fair frame. A third step, to remove the excess transmissions, is a prudent practice to avoid overloading the nodes which are closer to the gateway.

3.1. Compatible Nodes. Let $G = (V, E)$ be the network graph, where V is the set of nodes. The cardinal of V is $N + 1$ ($|V| = N + 1$), and E is the set of edges. As shown in Figure 2(a), in our network $|E| = N$ and there is a single edge leaving node n , the so-called edge e_{n-1} (because sensor nodes are numbered from 2 to $N + 1$). When a particular node is transmitting, elements M_{ij} of the compatibility matrix M [10] will be 1 if edges (e_i, e_j) can be active simultaneously and 0 otherwise. To enlighten the concept of compatibility matrix an example is provided in Figure 3, where we can note that node 6 has no compatible nodes ($M_{i,5} = M_{5,j} = 0$), since when node 6 is transmitting,

- (i) node 3 cannot transmit because it is receiving from node 6,
- (ii) neighbor node 9 cannot transmit because node 6 is not in the receiving mode,
- (iii) neighbor nodes 5 and 7 would interfere at node 3,
- (iv) neighbor nodes 8 and 10 cannot transmit because node 6 transmissions would interfere at nodes 5 and 7,
- (v) nodes 11, 12, and 13 (label “pn” in Figure 3(a)) cannot transmit because node 6 would interfere at nodes 8, 9, and 10,
- (vi) Nodes 2 and 4 (label “cn” in Figure 3(a)) cannot transmit because they would interfere at node 3.

The network relay scheme can be represented by an oriented graph. The cover of cliques, $\mathbb{C} = \{C_1, C_2, \dots, C_\ell\}$, is the set of maximal cliques in a graph. The natural number ℓ is unknown a priori. Many algorithms are available in the technical literature [18] to find \mathbb{C} . Our preferred algorithm is that in [19], due to its efficiency and simple implementation. Every clique C_i contains an edge or a group of edges that can be active without conflict; obviously, any subset of C_i also satisfies that requirement. Every edge in the graph is contained in at least one clique of the cover, and every time slot in the frame will contain one clique (or a subset of the clique) of the cover, which ensures the transmission compatibility in that slot.

3.2. Multiple-Vector Bin Packing Problem. We need to find the shortest frame, where each slot contains a set, or a subset, of edges in \mathbb{C} , subject to an exact number of instances of every active edge in the frame (to fulfill the requirement of fair operation), which is set T . This is a Multiple-Vector Bin Packing (MVBPP) problem [20], where the bins are the time slots and the items to pack are vectors, which are elements of \mathbb{C} or their subsets. This is a combinatorial optimization, which is widely accepted to be NP-complete problem [21]. We

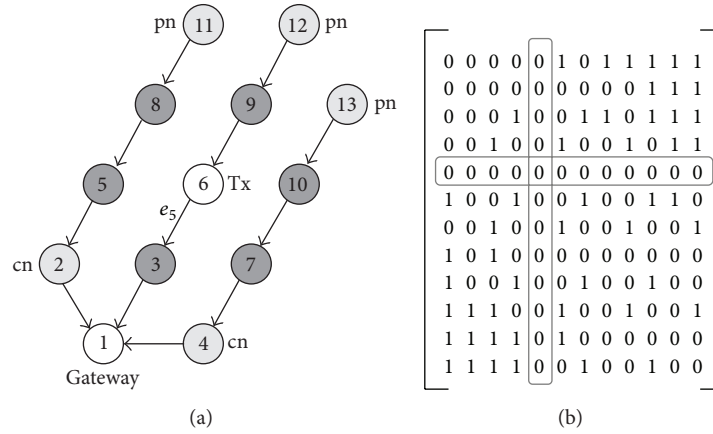


FIGURE 3: Network with 13 nodes and a corner gateway when node 6 is transmitting. (a) Dark gray: neighbor nodes, light gray: parent (pn) and child (cn) of neighbor nodes. (b) Compatibility matrix.

have particularized the general formulation for the present MVBP problem and obtained

$$\text{minimize } \sum_{j=1}^n y_j \quad (1)$$

$$\text{subject to } \sum_{j=1}^n x_{ij} \geq b_i, \quad i = 1, \dots, m \quad (2)$$

$$\sum_{i=1}^m w_i^k x_{ij} \leq y_j W^k, \quad j = 1, \dots, n, \quad k = 1, \dots, p \quad (3)$$

$$y_j \in \{0, 1\}, \quad j = 1, \dots, n \quad (4)$$

$$x_{ij} \in \{0, 1\}, \quad i = 1, \dots, m, \quad j = 1, \dots, n, \quad (5)$$

where the output variables are

y_j : 1 if time slot j is used or 0 otherwise;

x_{ij} : number of times that node i is assigned to time slot j (binary because one node can transmit only once in one slot);

n : length of the shortest frame.

The constraint for our frame searching problem is

b_i : demand for i node, $b_i = t_i$ for a fair frame;

m : number of sensor nodes (N) ($m = 1$ is node 2 and so on);

p : total number of C_i (compatible transmissions: \mathbb{C} and subsets);

w_i^k : weight of node i on the k th dimension. Each k -vector $w^k = (w_i^k)_{i=1, \dots, m}$ represents clique $C_k \in \mathbb{C}$; $w_i^k = 1$ if i node is an element of C_k , or 0 otherwise;

W^k : capacity of the k th dimension. In our case, W^k will be the number of elements of the largest clique in C_G , $W^k = \max(\{|C_1|, |C_2|, \dots, |C_\ell|\}) \forall k$.

It is important to note that every subset i of the clique C_k is assigned to a different vector $w^{(k_i)}$. For example, in Figure 3, every w^k will have $N = 12$ components. A maximal clique is $C_k = \{3, 12\}$, and three $w^{(k_i)}$ vectors are created: $w^{(k_1)} = (0, 1, 0, \dots, 0)$; $w^{(k_2)} = (0, \dots, 0, 1, 0)$; $w^{(k_3)} = (0, 1, 0, \dots, 0, 1, 0)$, meaning that both node 3 ($w^{(k_1)}$) and node 12 ($w^{(k_2)}$) are allowed to transmit on their own or simultaneously ($w^{(k_3)}$).

To find the optimum scheduling of transmissions x_{ij} in (1)–(5), an algorithm that solves MVBP problems, based on arc-flow graph formulation [22], is used.

3.3. Excess Transmissions. The constraints in (2) mean that the demand for transmissions (b_i) may exceed the initial set T . The workin [22] states that, otherwise, the MVBP solver algorithm may exclude other optimal solutions. In our case, the demand b_i should fulfill exactly t_i because of the expected fair behavior of the network. If it is exceeded, two inconveniences arise: (i) a possible traffic bottleneck, because the extra data cannot be delivered to the gateway in a frame and (ii) a waste of energy due to unnecessary transmissions, as the energy consumed by nodes is a critical parameter in UWSNs. The easiest solution is removing the excess of transmissions that exists in the frame.

4. Results

For the sake of simplicity, the STDMA protocol has been assumed to be ideal (error-free channel) and the performance of the network has been calculated under these circumstances. In a realistic channel, the packet error rate must be taken into account. Long propagation delays suggest that the preferred error detection and correction technique is FEC (Forward Error Correction). In this case, the throughput is decreased by a factor equal to the redundancy factor of

TABLE 1: Length of the optimal fair frame.

Network type	Symmetric network ($N \bmod 6 = 0$)	Asymmetric network ($N \bmod 6 \neq 0$)
Center	$L = N$	
Corner	$L = 7$ for $N = 6$ $L = \left(\frac{11}{6}N - 5\right)$ for $N > 6$	$L = \left(\frac{11}{6}N - \frac{9}{2}\right)$

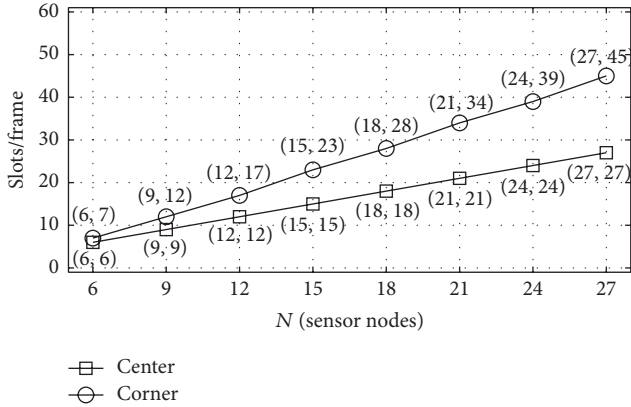


FIGURE 4: Length of the fair frame in optimal STDMA scheduling.

the FEC overhead, but the optimal fair scheduling remains unchanged.

The procedure described in the previous section has been used for networks of different sizes to obtain the shortest fair frame. Frame length L , shown in Figure 4, cannot be known a priori because the problem is NP-complete. We have analyzed networks with up to 42 nodes and used a polynomial fitting algorithm to find analytical expressions for L , which are shown in Table 1. These results can help to design a network since they allow calculating a lower bound for the time needed to get a complete data packet from every node. It is remarkable that when the gateway is in the center, the frame length always equals the number of sensors (N). This means that its scheduling has the shortest length.

The number of transmissions in a frame, $\sum_{i=2}^{N+1} t_i$, is an important figure concerning energy consumption. It depends only on set T . When the network has three or six branches and N is a multiple of three, the number of transmissions in the optimal fair frame follows a quadratic law in N , given by

$$\sum_{i=2}^{N+1} t_i \Big|_{\text{Corner}} = \frac{N^2}{6} + \frac{N}{2}, \quad (6)$$

$$\sum_{i=2}^{N+1} t_i \Big|_{\text{Center}} = \begin{cases} \frac{N^2}{12} + \frac{N}{2}, & \text{if } (N \bmod 6) = 0, \\ \frac{N^2}{12} + \frac{N}{2} + \frac{3}{4}, & \text{if } (N \bmod 6) = 3, \end{cases}$$

where “mod” stands for the modulo operation. These results are shown in Figure 5. It is noteworthy that the average number of transmissions per node, $\sum_{i=2}^{N+1} t_i/N$, follows a linear law with N .

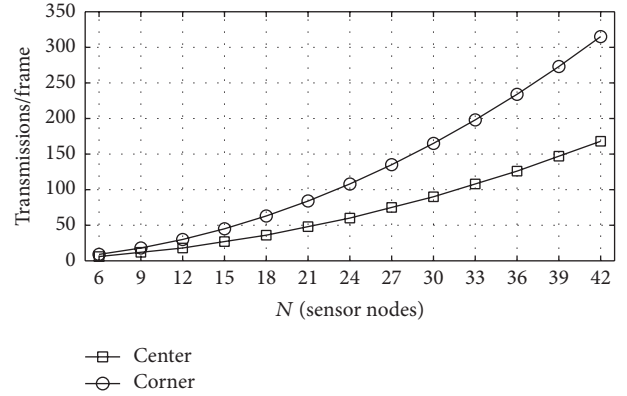


FIGURE 5: Total number of transmissions in a fair frame.

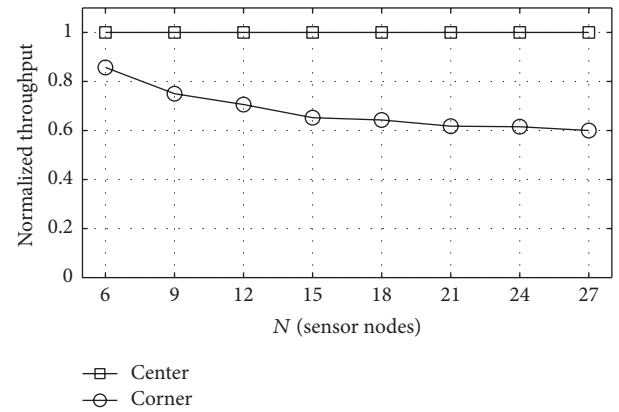


FIGURE 6: Normalized throughput.

The normalized throughput is defined as the ratio between the binary data rate through the gateway and the channel data rate, R_b . In the present case, this figure can be calculated as the ratio between the number of sensor nodes and the number of slots in a frame, N/L . Using the length of the optimal fair frame shown in Table 1, the normalized throughput is given in Figure 6. It can be seen that for networks with the gateway in the center the normalized throughput is 1 and that it is possible to get more than 70% of that ideal throughput in networks with up to 12 sensor nodes with the gateway on the corner. We consider that this is a manageable performance loss if we take into account that a gateway close to the shore is more convenient.

5. Conclusion

In this paper, a procedure that determines an optimal frame for STDMA UWSN with a fairness requirement has been presented. The network consists of three or six strings coming together to a gateway. The scheduling procedure uses two algorithms, one to find cliques in an oriented graph and MVB problem solver to find the shortest frame. Analytical expressions for the optimal frame lengths have also been presented. Two gateway locations were considered: at the center/edge of the network. Under ideal conditions, the

former has a maximum performance, whereas the latter reaches 70% of the maximum normalized throughput in networks with up to 12 sensor nodes.

Conflict of Interests

The authors declare that there is no conflict of interests regarding the publication of this paper.

References

- [1] A. Marsouin, P. Le Borgne, G. Legendre, S. Péré, and H. Roquet, "Six years of OSI-SAF METOP-A AVHRR sea surface temperature," *Remote Sensing of Environment*, vol. 159, no. 3, pp. 288–306, 2015.
- [2] M. J. Devlin, C. Petus, E. da Silva et al., "Water quality and river plume monitoring in the Great Barrier Reef: an overview of methods based on ocean colour satellite data," *Remote Sensing*, vol. 7, no. 10, pp. 12909–12941, 2015.
- [3] V. V. Klemas, "Coastal and environmental remote sensing from unmanned aerial vehicles: an overview," *Journal of Coastal Research*, vol. 31, no. 5, pp. 1260–1267, 2015.
- [4] M. Postacchini, L. R. Centurioni, L. Braasch, M. Brocchini, and D. Vicinanza, "Lagrangian observations of waves and currents from the river drifter," *IEEE Journal of Oceanic Engineering*, vol. 41, no. 1, pp. 94–104, 2016.
- [5] D. Morichon, D. Dailloux, S. Aarninkhof, and S. Abadie, "Using a shore-based video system to hourly monitor storm water plumes (Adour River, Bay of Biscay)," *Journal of Coastal Research*, vol. 24, no. 4, pp. 133–140, 2008.
- [6] D. Pompili and T. Melodia, "Research challenges in communication protocol design for underwater sensor networks," in *Underwater Acoustic Sensor Networks*, CRC Press, Boca Raton, Fla, USA, 2010.
- [7] I. F. Akyildiz, D. Pompili, and T. Melodia, "Underwater acoustic sensor networks: research challenges," *Ad Hoc Networks*, vol. 3, no. 3, pp. 257–279, 2005.
- [8] R. Otnes, A. Asterjadhi, P. Casari et al., *Underwater Acoustic Networking Techniques*, Springer, Heidelberg, Germany, 2012.
- [9] S. Shahabudeen, M. Chitre, and M. Motani, "Adaptive multimode medium access control for underwater acoustic networks," *IEEE Journal of Oceanic Engineering*, vol. 39, no. 3, pp. 500–514, 2014.
- [10] R. Nelson and L. Kleinrock, "Spatial TDMA: a collision-free multihop channel access protocol," *IEEE Transactions on Communications*, vol. 33, no. 9, pp. 934–944, 1985.
- [11] J. Mo and J. Walrand, "Fair end-to-end window-based congestion control," *IEEE/ACM Transactions on Networking*, vol. 8, no. 5, pp. 556–567, 2000.
- [12] Z. Wang, F. Yu, J. Tian, and Z. Zhang, "A fairness adaptive TDMA scheduling algorithm for wireless sensor networks with unreliable links," *International Journal of Communication Systems*, vol. 27, no. 10, pp. 1535–1552, 2014.
- [13] R. Diamant and L. Lampe, "Spatial reuse time-division multiple access for broadcast ad hoc underwater acoustic communication networks," *IEEE Journal of Oceanic Engineering*, vol. 36, no. 2, pp. 172–185, 2011.
- [14] M. Chitre, M. Motani, and S. Shahabudeen, "Throughput of networks with large propagation delays," *IEEE Journal of Oceanic Engineering*, vol. 37, no. 4, pp. 645–658, 2012.
- [15] Y. Xiao, M. Peng, J. Gibson, G. G. Xie, D.-Z. Du, and A. V. Vasilakos, "Tight performance bounds of multihop fair access for MAC protocols in wireless sensor networks and underwater sensor networks," *IEEE Transactions on Mobile Computing*, vol. 11, no. 10, pp. 1538–1554, 2012.
- [16] P. Björklund, P. Väbrand, and D. Yuan, "A column generation method for spatial TDMA scheduling in ad hoc networks," *Ad Hoc Networks*, vol. 2, no. 4, pp. 405–418, 2004.
- [17] A.-M. Chou and V. O. K. Li, "Slot allocation strategies for TDMA protocols in multihop packet radio networks," in *Proceedings of the the 11th Annual Conference of the IEEE Computer and Communications Societies (IEEE INFOCOM '92)*, vol. 2, pp. 710–716, Florence, Italy, May 1992.
- [18] E. R. Harley, "Comparison of clique-listing algorithms," in *Proceedings of the International Conference on Modeling, Simulation & Visualization Methods and the International Conference on Algorithmic Mathematics & Computer Science (MSV-AMCS '04)*, vol. 4, pp. 433–438, Las Vegas, Nev, USA, June 2004.
- [19] C. Bron and J. Kerbosch, "Algorithm 457: finding all cliques of an undirected graph," *Communications of the ACM*, vol. 16, no. 9, pp. 575–577, 1973.
- [20] B. Patt-Shamir and D. Rawitz, "Vector bin packing with multiple-choice," *Discrete Applied Mathematics*, vol. 160, no. 10–11, pp. 1591–1600, 2012.
- [21] M. R. Garey and D. S. Johnson, *Computers and Intractability, A Guide to the Theory of NP-Completeness*, Freeman, San Francisco, Calif, USA, 1979.
- [22] F. Brandão and J. P. Pedroso, "Bin packing and related problems: general arc-flow formulation with graph compression," Tech. Rep. DCC-2013-13, Faculdade de Ciências da Universidade do Porto, Porto, Portugal, 2013, http://www.optimization-online.org/DB_FILE/2013/10/4096.pdf.

Research Article

A New Small Drifter for Shallow Water Basins: Application to the Study of Surface Currents in the Muggia Bay (Italy)

Carmelo Nasello¹ and Vincenzo Armenio²

¹*Dipartimento di Ingegneria Civile, Ambientale, Aerospaziale, dei Materiali, Università di Palermo, Viale delle Scienze, 90128 Palermo, Italy*

²*Dipartimento di Ingegneria e Architettura, Università di Trieste, Piazzale Europa 1, 34127 Trieste, Italy*

Correspondence should be addressed to Carmelo Nasello; carmelo.nasello@unipa.it

Received 1 October 2015; Accepted 14 December 2015

Academic Editor: Jose C. Nieto-Borge

Copyright © 2016 C. Nasello and V. Armenio. This is an open access article distributed under the Creative Commons Attribution License, which permits unrestricted use, distribution, and reproduction in any medium, provided the original work is properly cited.

A new small drifter prototype for measuring current immediately below the free surface in a water basin is proposed in this paper. The drifter dimensions make it useful for shallow water applications. The drifter transmits its GPS location via GSM phone network. The drifter was used to study the trajectory of the surface current in the Muggia bay, the latter containing the industrial harbor of the city of Trieste (Italy). The analysis has been carried out under a wide variety of wind conditions. As regards the behavior of the drifter, the analysis has shown that it is well suited to detect the water current since its motion is marginally affected by the wind. The study has allowed detecting the main features of the surface circulation within the Muggia bay under different meteorological conditions. Also, the study has shown that the trajectory of the surface current within the bay is weakly affected by the Coriolis force.

1. Introduction and Drifter Prototype Description

The deployed drifters used to measure the surface current at sea are essentially of two types: drogued and undrogued [1]. The Surface Velocity Program (SVP) and the Coastal Ocean Dynamics Experiment (CODE) drifters are examples of drogued and undrogued drifters, respectively. The SVP has a subsurface holey-sock drogue centered at 15 m nominal depth [2, 3]. The CODE measures coastal currents in the first meter below the free surface [4, 5].

The position of a drifter can be inferred from the Doppler-based Argos tracking, or from a satellite GPS system [6]. The transmission of data uses terrestrial cellular phone networks (for coastal operations) or satellite global phone systems.

A former low cost (drogued) drifter, with GPS connection, but without data-transmission capability, has been employed to measure the mean subsurface currents between 2.5 and 8.5 m by Johnson et al. [7]. The instrument casing had a submerged area of 40 cm², and an emerged portion of 48 cm². Later on, Kōuts et al. [8] developed a low cost drifter,

GPS equipped and with GPRS communication, having a diameter of 0.11 m and a length of 1 m. These buoys had a percentage of fault GPS positioning up to 20% in presence of waves, or less than 10% in calm water. A third low cost drifter had a submerged depth of 0.40 m; the GPS (WAAS corrected) antenna emerged for 0.70 m; the buoy did not have a data-transmission system [9].

Due to their dimensions, the above-mentioned systems cannot be employed in lagoons with water depth smaller than 1 meter. Since it is often necessary to measure the water current immediately below the water surface, a novel small drifter prototype was developed and its own features are presented in the present paper. It is suited for coastal basins, lakes, shallow lagoons, and river reaches, in particular close to obstacles where the main stream is deviated due to the occurrence of downstream separated regions. Due to its own inertia, the drifter is not able to adapt its trajectory to the turbulent fluctuations of the surface current and it measures the mean current in the first 0.20 m below the free surface. Accurate measurements of the water velocity near the free surface are gathered by means of this instrumentation and

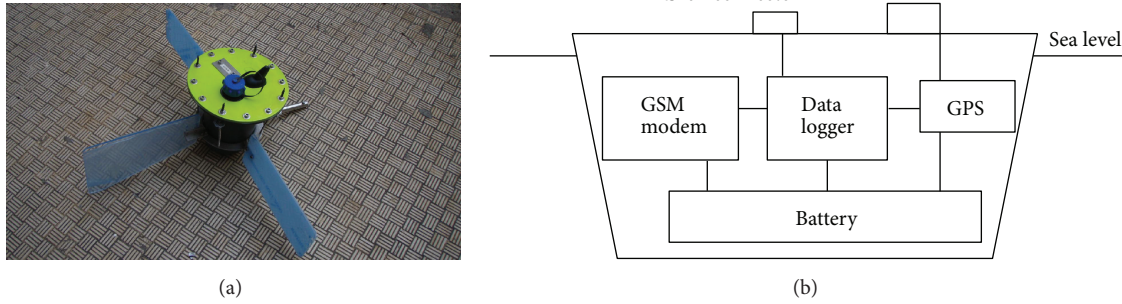


FIGURE 1: (a) Picture of the drifter equipped with the three wings; (b) schematic diagram of drifter.

used to detect trajectories of tracers transported at the free surface level.

The prototype drifters have a troncoconical shape, with a maximum diameter (at the top) of 0.30 m and height of 0.21 m (Figure 1(a)). Each drifter is equipped with three plastic wings to keep the trajectory stable during the motion and to avoid rotation around its own vertical axis. Two wings are rectangular (0.30×0.12 m) and they increase the section of the drifter perpendicular to the current. The width of this section is 0.80 m, bigger than twice the drifter diameter. The presence of the wings makes the drifter velocity very close to the local mean current velocity. The third wing has a trapezoidal shape since it operates as a helm. Overall, the depth of the system is of 0.20 m. The buoy is not completely submerged; for GPS and GSM communication purposes, the top of the buoy emerges over the surface by 0.010 m, the GPS antenna by 0.020 m, and the connector RS232 by 0.015 m. The part exposed to the wind is very small making its effect negligible in comparison to the mean current acting over the submerged part of the buoy. Inside, the drifter is equipped with a GPS satellite system, a GSM modem, a recording memory, and a battery (Figure 1(b)). Each trajectory is remotely sampled every 2 min by the GPS system and transmitted via GSM to the operator. GPS positions are corrected by means of the WAAS system, so that the overall error is smaller than $2 \div 3$ meters.

2. Field Campaigns

The drifters were used to sample the trajectory of the surface current in the Muggia bay under different meteorological conditions. The Muggia bay is inside the harbor area of the city of Trieste, Italy. The bay develops along the east–west axis for about 4 km and communicates with the Gulf of Trieste through the western section, about 3 km wide; there, the bay is delimited by three breakwaters that substantially affect water circulation. The bathymetry displays a shallow water basin, with a maximum depth of approximately 20 m in the western region close to the breakwaters, while in the eastern portion the depth decreases to about 5–10 m. The Northern side of the coast is characterized, from west to east, by docks of the harbor area of Trieste and by two wharfs belonging to an international oil terminal.

The drifters were released in the proximity of the wharfs close to the ships moored over there, and left in the water for a time interval of about 15 h. Some drifters landed either at the shore or at the floating oil barriers below the wharfs. In both cases, they were recovered by the operators.

The drifters were launched during different field campaigns; in this paper we focus on the late-summer one, carried out over 5 days in September 2011 [10].

The wind velocity and direction were measured every second at a meteorological station, located 28 m a.s.l. on the western wharf of the oil terminal. The Muggia bay is characterized by a diurnal ($270\text{--}330^\circ$ from Northwest) and nocturnal ($90^\circ\text{--}150^\circ$ from Southeast) breeze regime often interrupted by events of strong and cold wind blowing from Northeast (Bora) (Figure 2). Only one wind measurement station was available during the field campaigns, and since the largest distance achieved by the buoys from this station was about 2.5 km, it was assumed that the wind field is spatial homogeneous in the study area. The wharf of the oil terminal is formed by a linear steel platform placed on a series of steel piles, having little influence on the wind spatial homogeneity. Only in presence of ships, as we will show later on in the paper, the wind by the downward side can be considered absent.

During the first 3 days, the wind intensity was in the range $2 \div 5$ m/s. During the last 2 days of the field campaign, the wind blew from the first quadrant with a velocity of about 10 m/s.

The first buoy (labeled B6) was launched on September 12th, 2011, at 14:37. B6 was released near the stern of an oil tanker berthed at the eastern wharf, under Northwest wind conditions. After the release, the drifter initially moved parallel to the ship, and then it ran away following the wind direction (Figure 3). It was first directed towards the Southeast and then towards the Northeast and finally towards the Northwest landing on the shore after midnight. The wind is also plotted in Figure 3. It is first directed towards the Southeast and then the Northwest. The maximum wind intensity was $W_{\max} = 4.64$ m/s while the maximum drifter velocity was $V_{\max} = 0.29$ m/s. The buoy reached the furthest eastern point of its trajectory 5 hours after the release. After that, its velocity dropped down to zero for 3.5 hours. Then the drifter started moving again and it reached the shore in 1.5

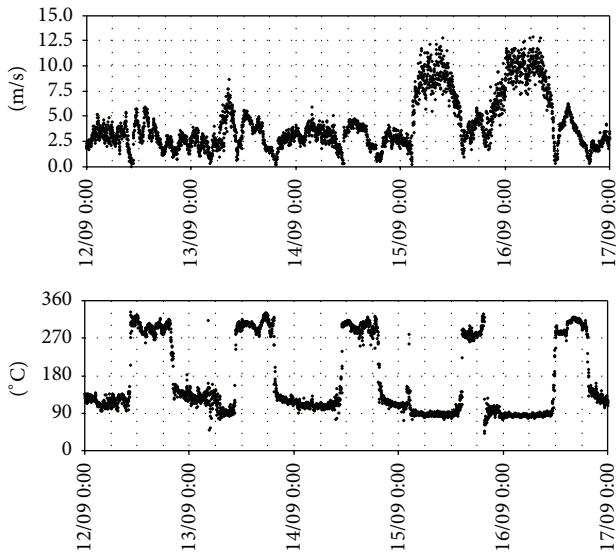
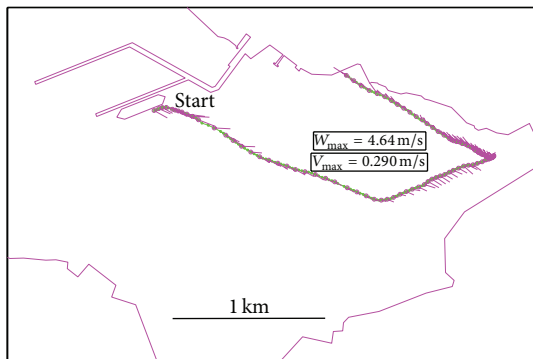


FIGURE 2: Wind intensity (m/s) and direction (0° from North, 90° from east) during the late-summer campaign considered in the present paper.



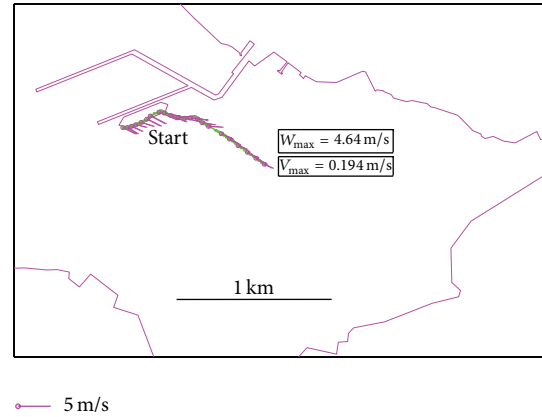
5 m/s

FIGURE 3: Drifter B6 released on September 12th, 2011, at 14:37, landed at shore at 24:40. The drifter positions are in green circles; the wind vectors are violet.

hours. The GPS coordinates of the trajectory are not filtered; the WAAS correction makes the position error negligible (Figure 3).

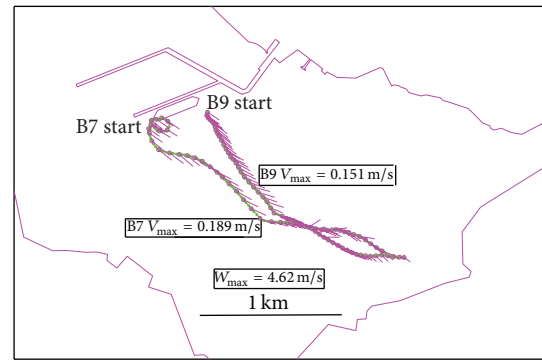
Comparison with velocity field obtained by means of high-resolution numerical simulations [10] clearly shows that the initial trajectory is related to the presence of a local circulatory motion developing down the ship. Overall, Figure 3 suggests that, in open area, where the free surface current is nearly aligned with the wind direction, the trajectory of the drifter is nearly aligned with the wind. On the other hand, downward of large structures or in the near-shore region, where the surface current has to deviate significantly from the wind direction, the drifter is essentially transported by the surface current.

Few minutes after the release of B6, another one (B12) was launched from a location close to the bow of the same



5 m/s

FIGURE 4: Drifter B12 released on September 12th, 2011, at 14:40, retrieval at 17:00.



5 m/s

FIGURE 5: Drifter B7 released on September 14th, 2011, at 11:15, retrieval at 16:05. Drifter B9 released on September 14th, 2011, at 11:30, retrieval at 17:15.

oil tanker. Similarly to B6, the drifter first moved parallel to the ship, according to the local current direction, ruled by the small downward gyre, and then it turned Southeast (Figure 4). The maximum velocity was $V_{\max} = 0.19$ m/s, typical of sea currents, while $W_{\max} = 4.64$ m/s. B12 was taken out at 17:00 while travelling Southeast.

Buoys B7 and B9 were launched on September 14th, 2011, at 11:15 and 11:30. At that time, the wind was blowing from Northwest with maximum wind intensity $W_{\max} = 4.62$ m/s. The drifter B7 first described a counterclockwise vortex and then moved towards the Southeast ($V_{\max} = 0.19$ m/s). It was finally taken out at 16:05 in the eastern part of the bay (Figure 5). The vortex is associated with the presence of a wake developing down the bow of an oil tanker berthed at the eastern wharf. Conversely, from its release B9 moved directly Southeast, showing the absence of circulatory motion in the region of the aft of the ship. The behavior of the two buoys suggests that, under Northwest wind conditions, the sea current is more intense toward the central part of the bay (bow region of the ship) due to the sheltering effect due to the coastline in the inshore region, where B9 was released.

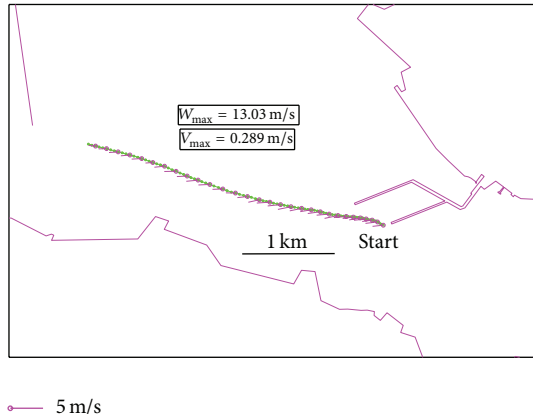


FIGURE 6: Drifter B6 released on September 15th, 2011, at 09:30, retrieval at 12:30.

From September 11th to 14th the wind was characterized by the typical breeze regime (diurnal from Northwest and nocturnal from the eastern quadrants) with low velocity. A wind with $W_{\max} = 13.03$ m/s from east was present on September 15th, 2011. In the morning the buoy B6, released in the eastern wharf, rapidly moved ($V_{\max} = 0.29$ m/s) west reaching the breakwaters of the harbor (Figure 6). The drifter traveled 2.5 km in 3 hours, with a mean velocity of 0.22 m/s, much larger than the mean values of previous days. Even in this case, the drifter trajectory did not exactly match the wind direction, confirming that the drifter trajectory is mainly influenced by the surface current.

Buoys B3 and B9 were launched on September 15th, 2011, at 14:10, when the wind was still blowing from east. Both buoys initially moved west (Figure 7). The wind turned and blew from the western quadrants at around 15:00. After that, the drifter B9 turned clockwise towards the Northeast and it was then stopped by artificial floating oil barriers placed under the wharfs and submerged by about 0.50 m. In this case it was necessary to rescue the drifter stopped by the artificial obstacle. On the other hand, as the wind turned the drifter B3 turned counterclockwise moving to the Southeast.

Wind blew from east with an intensity of $W = 8$ m/s when the buoys B9 and B6 were released on September 16th, 2011, at 10:10 and 10:25. At the beginning, both drifters were directed to the Southwest (Figure 8). The wind stopped blowing from east at around 11:00 and the typical diurnal breeze from west started. As the previous day it can be noticed that the drifters turned together with the wind, but their trajectories do not match the wind direction, confirming that the drifter trajectory is mostly dependent on the current direction with respect to the wind.

Maximum drifter velocity values and maximum wind intensities for each drifter release are shown in Table 1. Velocity values of 0.29 m/s were recorded with wind intensities of both 13 m/s and 5 m/s.

Finally, a question may be raised over the effect of Coriolis force on drifter trajectories. We cannot give a direct answer to the question, but we can give some argumentations based on dimensional analysis. The effect of Coriolis force is well known to be ruled by the Rossby number $R_o = V/Lf$, where V

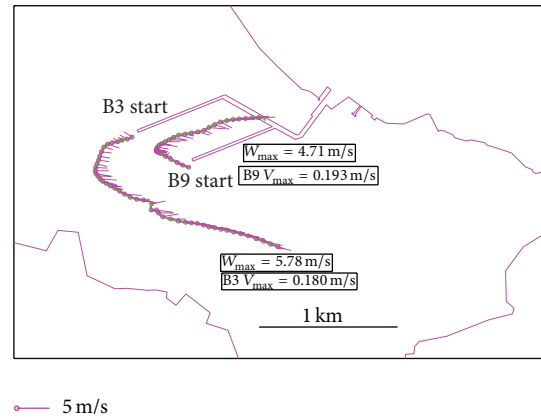


FIGURE 7: Drifter B3 released on September 15th, 2011, at 14:10, retrieval at 19:00. Drifter B9 released on September 15th, 2011, at 14:10, retrieval at 17:20.

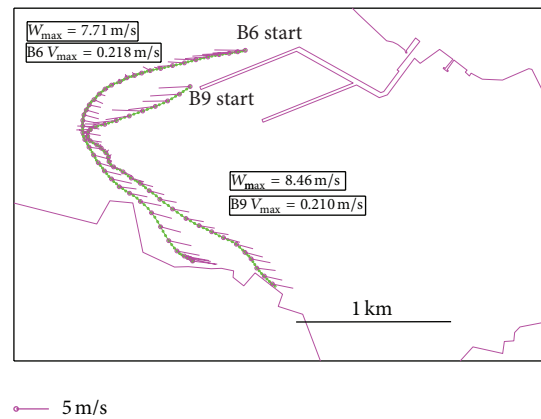


FIGURE 8: Drifter B9 released on September 16th, 2011, at 10:10, retrieval at 13:44. Drifter B6 released on September 16th, 2011, at 10:25, retrieval at 14:35.

is the velocity of the drifter, L is a length scale of the problem, for instance, the distance travelled by the drifter, and f is the Coriolis parameter of the order of 10^{-4} (s^{-1}) at the latitude of the Muggia bay. In the Northern Hemisphere the Coriolis force is known to deviate the trajectory by the right side. The Coriolis force is more active when the velocity is small, so, considering the smallest velocity recorded by our drifters we have an estimation of $R_o \sim 1$ when the drifter travels by few ($1 \div 2$) kilometers. In these situations, the effect of Coriolis force is very weak but still detectable.

3. Conclusions

In the present paper we present a new small drifter prototype, suited for shallow water conditions and able to trace the trajectory of the surface current, within the first 0.20 m below the free surface. The drifter was used to detect the trajectory of the surface current in the Muggia bay, the industrial harbor of the city of Trieste (Italy). They were released under different meteorological conditions, with wind direction and intensity varying in a wide range of values. As a general comment, we

TABLE I: Maximum drifter velocity values and maximum wind intensities.

Buoy	Release	Retrieval	V_{\max} (m/s)	W_{mean} (m/s)	W_{\max} (m/s)
B6	12.09.2011 14:37	12.09.2011 24:40	0.29	2.39	4.64
B12	12.09.2011 14:40	12.09.2011 17:00	0.19	3.14	4.64
B7	14.09.2011 11:15	14.09.2011 16:05	0.19	3.95	4.62
B9	14.09.2011 11:30	14.09.2011 17:15	0.15	3.63	4.62
B6	15.09.2011 09:30	15.09.2011 12:30	0.29	8.52	13.03
B3	15.09.2011 14:10	15.09.2011 19:00	0.18	3.72	5.78
B9	15.09.2011 14:10	15.09.2011 17:20	0.19	3.26	4.71
B6	16.09.2011 10:25	16.09.2011 14:35	0.22	3.81	7.71
B9	16.09.2011 10:10	16.09.2011 13:44	0.21	3.62	8.46

can say that since the drifter is only marginally exposed to the action of the wind, their motion is more likely driven by the surface current in the sea. Overall the trajectory of the drifters suggests that under the typical conditions of wind blowing from the western quadrants, the surface currents are driven east and then it turns due to the presence of the coastline. Under eastern wind conditions the surface currents develop primarily from east to west driving the surface internal water out of the bay.

Finally, dimensional considerations suggest that the Coriolis force may have a weak effect on the trajectory of the surface current within the bay.

Conflict of Interests

The authors declare that there is no conflict of interests regarding the publication of this paper.

Acknowledgments

Vincenzo Armenio has been supported by the University of Trieste under project FRA 2013 Modellistica Numerica e Sperimentale di Fenomeni di Erosione Localizzata in Alvei Fluviali and by the Flag project RITMARE, Action SP5-WP4-AZ3-UO06.

References

- [1] S. E. Pazan, "Intercomparison of drogued and undrogued drift buoys," in *Proceedings of OCEANS '96. MTS/IEEE. Prospects for the 21st Century*, vol. 2, Fort Lauderdale, Fla, USA, September 1996.
- [2] P. P. Niiler and J. D. Paduan, "Wind-driven motions in the northeast pacific as measured by lagrangian drifters," *Journal of Physical Oceanography*, vol. 25, no. 11, pp. 2819–2830, 1995.
- [3] R. Lumpkin and M. Pazos, "Measuring surface currents with SVP drifters: the instrument, its data and some results," in *Lagrangian Analysis and Prediction of Coastal and Ocean Dynamics*, A. Griffa, A. D. Kirwan Jr., A. J. Mariano, T. Özgökmen, and H. T. Rossby, Eds., pp. 39–67, Cambridge University Press, Cambridge, UK, 2007.
- [4] R. E. Davis, "Drifter observations of coastal surface currents during CODE: the method and descriptive view," *Journal of Geophysical Research*, vol. 90, no. 3, pp. 4741–4755, 1985.
- [5] J. P. Manning, D. J. McGillicuddy Jr., N. R. Pettigrew, J. H. Churchill, and L. S. Incze, "Drifter observations of the gulf of maine coastal current," *Continental Shelf Research*, vol. 29, no. 7, pp. 835–845, 2009.
- [6] P.-M. Poulain, A. Bussani, R. Gerin et al., "Mediterranean surface currents measured with drifters: from basin to subinertial scales," *Oceanography*, vol. 26, no. 1, pp. 38–47, 2013.
- [7] D. Johnson, R. Stocker, R. Head, J. Imberger, and C. Pattiaratchi, "A compact, low-cost GPS drifter for use in the oceanic nearshore zone, lakes, and estuaries," *Journal of Atmospheric and Oceanic Technology*, vol. 20, no. 12, pp. 1880–1884, 2003.
- [8] T. Kõuts, S. Verjovkina, P. Lagema, and U. Raudsepp, "Use of lightweight on-line GPS drifters for surface current and ice drift observations," in *Proceedings of the IEEE/OES US/EU Baltic International Symposium*, Riga, Latvia, August 2010.
- [9] J. MacMahan, J. Brown, and E. Thornton, "Low-Cost handheld global positioning system for measuring surf-zone currents," *Journal of Coastal Research*, vol. 25, no. 3, pp. 744–754, 2009.
- [10] A. Petronio, F. Roman, C. Nasello, and V. Armenio, "Large eddy simulation model for wind-driven sea circulation in coastal areas," *Nonlinear Processes in Geophysics*, vol. 20, no. 6, pp. 1095–1112, 2013.

Research Article

Multifocus Color Image Fusion Based on NSST and PCNN

Xin Jin, Rencan Nie, Dongming Zhou, Quan Wang, and Kangjian He

Information College, Yunnan University, Kunming 650091, China

Correspondence should be addressed to Dongming Zhou; zhoudm@ynu.edu.cn

Received 7 August 2015; Revised 29 October 2015; Accepted 5 November 2015

Academic Editor: Claudio Lugni

Copyright © 2016 Xin Jin et al. This is an open access article distributed under the Creative Commons Attribution License, which permits unrestricted use, distribution, and reproduction in any medium, provided the original work is properly cited.

This paper proposed an effective multifocus color image fusion algorithm based on nonsubsampled shearlet transform (NSST) and pulse coupled neural networks (PCNN); the algorithm can be used in different color spaces. In this paper, we take HSV color space as an example, H component is clustered by adaptive simplified PCNN (S-PCNN), and then the H component is fused according to oscillation frequency graph (OFG) of S-PCNN; at the same time, S and V components are decomposed by NSST, and different fusion rules are utilized to fuse the obtained results. Finally, inverse HSV transform is performed to get the RGB color image. The experimental results indicate that the proposed color image fusion algorithm is more efficient than other common color image fusion algorithms.

1. Introduction

Video technology is one of the important technologies for coastal monitoring, and image fusion is the basis of video technology. Color images contain color information and brightness information, so the color images are more suitable for coastal monitoring than gray images [1]. Besides, the identifiable degree of human vision to color information is higher than the gray image [2]. The whole procedure of the image fusion is to extract the significant and representative information from the source images of the same scene, which may come from different types of image sensors or the same one acting in different modes, and then attempt to fuse it into the final composite image with a better description of the scene than any of the individual source images. Thus, the study of suitable fusion technology in multisensor image is necessary and valuable [3].

Color image is the combination of different brightness and colors. Because color image is comprised of several components and the fusion image is the fusion of each color space component, there are some common algorithms, such as average, Intensity, Hue and Saturation (HIS), and principal component analysis (PCA) [4, 5], which are easy to implement but the performances are not good. Recently, image fusion methods based on multiresolution analysis have been widely studied; the first step is image transform and

then recombining the coefficients of the transformed image; at last the fused image can be obtained by inverse transform. According to the different ways of decomposition, these algorithms can be divided into pyramid transform, wavelet transform [6], curvelet [7], and contourlet [8]. In 2005, Labate et al. proposed a new multidimensional representation algorithm, which is called shearlet [9]. One advantage of this algorithm is that it can be constructed using generalized multiresolution analysis and efficiently implemented using a classical cascade algorithm. So shearlet has good performance in both time domain and frequency domain [10]. In order to combine the superiorities and overcome the defects of nonsubsampled contourlet transform (NSCT) and shearlet transform (ST), [11] proposed the theory of nonsubsampled shearlet transform (NSST) combining the nonsubsampled Laplacian pyramid transform with several different shearing filters. In comparison with current multiresolution geometric analysis (MGA) tools, NSST absorbs some recent developments in the MGA field and shows satisfactory fusion performance such as the better sparse representation ability and much lower computational costs. Besides, NSST also has the requirement of the shift-invariance property ST lacks. Therefore, it is hoped that further research on the area of image fusion based on NSST domain is promising and competitive [12]. In recent years, the image fusion method based on PCNN is getting more and more attention by many experts and scholars with

PCNN's characters in biological background. Compared with other artificial neural networks, PCNN has an incomparable advantage over other traditional artificial neural networks. So PCNN has been widely used in image processing fields and shows extremely superior performances [12–15].

In this paper, a new multifocus color image fusion algorithm is proposed based on NSST and PCNN. The paper absorbs some advantages of NSST and PCNN; it firstly converts RGB color image to HSV color image, and then H component is input into adaptive simplified PCNN (S-PCNN) model to get oscillation frequency graph (OFG) of S-PCNN; a new fused H component is obtained by comparing the OFG; S and V components are decomposed into low frequency subband and high frequency subband by NSST, and these subbands are fused by different methods to get new fused S and V components. At last, inverse HSV transform is performed to obtain a new fused RGB color image. The experimental results indicate that the proposed algorithm is more effective to save the color information of the source color images than other common algorithms; and the fused image contains more edges, texture, and detail.

This paper is arranged as follows. Section 2 introduces related theories of NSST and PCNN model. Section 3 explains the proposed algorithm, including framework and workflow. Section 4 presents the experimental results and analysis. Section 5 concludes this paper.

2. Related Theories

2.1. PCNN. PCNN model has three fundamental parts: the receptive field, the modulation field, and the pulse generator [13, 14]. In the receptive field, which consists of L and F channels and is described by (1), the neuron receives neighboring neurons' coupling input Y and external stimulus input S . In L and F channels of the neuron, the neuron links with its neighborhood neurons via the synaptic linking weights W and M , respectively; the two channels accumulate input and exponential decay changes at the same time; the decay exponentials are α^L and α^F , respectively, while the channel amplitudes are V^L and V^F , respectively:

$$\begin{aligned} F_{ij}(n) &= V^F \sum_{kl} M_{ijkl} Y_{kl}(n-1) + e^{-\alpha^F} F_{ij}(n-1) + S_{ij}, \\ L_{ij}(n) &= V^L \sum_{kl} W_{ijkl} Y_{kl}(n-1) + L_{ij}(n-1) e^{-\alpha^L}. \end{aligned} \quad (1)$$

In the modulation field, the linking input $L_{ij}(n)$ made by adding a bias to the linking; then, it is multiplied by the feeding input; the bias is unitary, β is the linking strength, and the total internal activity U is the result of modulation, which is described by

$$U_{ij}(n) = F_{ij}(n) [1 + \beta L_{ij}(n)]. \quad (2)$$

Pulse generator consists of a threshold adjuster, a comparison organ, and a pulse generator, which is described by (3). Its function is to generate the pulse output Y , and θ_{ij} is adjustment threshold; V_{ij}^θ is threshold coefficient. When

the internal state U is larger than the threshold θ , that is, the neuron satisfies the condition $U_{ij}(n) > \theta_{ij}(n)$, a pulse would be produced by the neuron; we call an ignition, which is described by (4):

$$\theta_{ij}(n) = e^{-\alpha^\theta} \theta_{ij}(n-1) + V_{ij}^\theta Y_{ij}(n-1), \quad (3)$$

$$Y_{ij}(n) = \begin{cases} 1, & U_{ij}(n) > \theta_{ij}(n) \\ 0, & \text{otherwise,} \end{cases} \quad (4)$$

where the subscripts i and j represent the neuron location in PCNN and n denotes the current iteration (discrete time step), where n varies from 1 to N (N is the total number of iterations). In particular, "a neuron ignition" means a PCNN's neuron generates a pulse. The total times of ignitions represent image information of the corresponding code sequences after N iterations.

When PCNN is used for image processing, a pixel is connected to unique neuron. The number of neurons in the network is equal to the pixel number of the input image; namely, there exists one-to-one correspondence between the image and neurons network, and the pixel value is taken as the external input stimulus of the neuron in F channel. A neuron outputs results in two states, namely, pulse (status 1) and nonpulse (status 0), so the output status of neurons composes a binary image. More information about PCNN will be found in [12–15].

2.2. S-PCNN. Simplified PCNN (S-PCNN) model [15] is composed the same as the original PCNN model, but the input of F channel is only related to image gray value and has no relationship with external coupling and exponential decay characteristics, and its parameters are less than original PCNN model, and the input channel of the receptive field is simple and effective. In S-PCNN model, the variables of a neuron N_{ij} satisfy the following:

$$\begin{aligned} F_{ij}(n) &= S_{ij}, \\ L_{ij}(n) &= V_{ij}^L \sum_{kl} W_{ijkl} Y_{kl}(n-1) + L_{ij}(n-1) e^{-\alpha^L}, \\ U_{ij}(n) &= F_{ij}(n) [1 + \beta L_{ij}(n)], \\ \theta_{ij}(n) &= e^{-\alpha^\theta} \theta_{ij}(n-1) + V_{ij}^\theta Y_{ij}(n-1), \end{aligned} \quad (5)$$

$$Y_{ij}(n) = \begin{cases} 1, & U_{ij}(n) > \theta_{ij}(n) \\ 0, & \text{otherwise.} \end{cases}$$

2.3. The OFG of PCNN. Capture characters of PCNN neurons will cause a similar brightness to the surrounding neurons to capture the ignition.. The capture characters can be automatically coupled to transmit information. In this paper, we use PCNN to extract image features; PCNN also can extract the information of the image's texture, edge, and regional distribution and has a good effect on image processing. In an iteration of PCNN, a binary image will be obtained

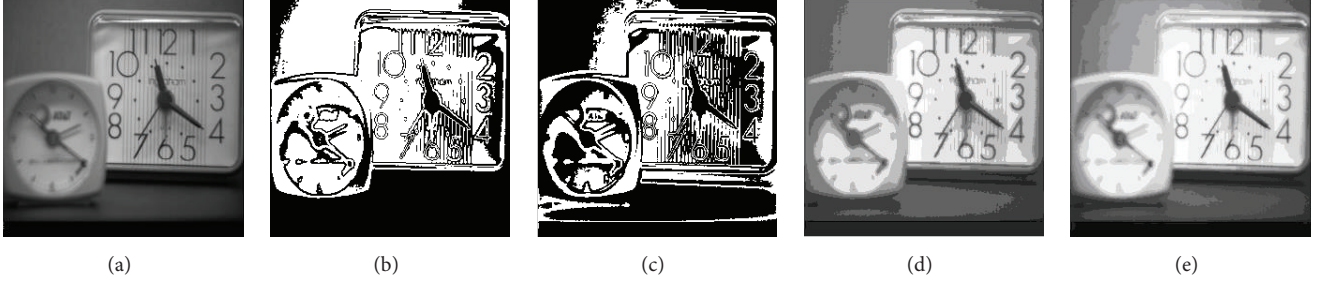


FIGURE 1: An illustration of the binary map and OFG. (a) Source image. (b) Binary map at 4th time iteration. (c) Binary map at 8th time iteration. (d) OFG at 10th time iteration. (e) OFG at 15th time iteration.

by recording the neuron fires or not. The binary images effectively express the features of the image such as texture, edge, and regional distribution; the binary map and OFG are shown in Figures 1(b) and 1(c). After the global statistics of the binary image of the neurons, we get an oscillation frequency graph (OFG), which is shown in (6) and Figures 1(d) and 1(e):

$$\text{OFG}^N(i, j) = \sum_{n=1}^N Y_{ij}(n), \quad (6)$$

where N denotes the iteration times, Y_{ij} denotes the pulse output of the neuron (i, j), and n is the current iteration.

2.4. Nonsampled Shearlet Transform. Shearlet transform was proposed based on wavelet by Labate et al. [9, 11]. In dimension $n = 2$, affine system

$$\psi_{AS}(\psi) = \{\psi_{j,l,k}(x) = |\det A|^{j/2} \psi(S^l A^j x - k) : l, j \in \mathbb{Z}, k \in \mathbb{Z}^2\}, \quad (7)$$

where ψ is a collection of basis functions and satisfies $\psi \in L^2(\mathbb{R}^2)$; A represents anisotropy matrix for multiscale partitions; S is a shear matrix for directional analysis. j, l , and k are scale, direction, and shift parameter, respectively. A and S are both 2×2 invertible matrices and $|\det S| = 1$. For $\forall a > 0$ and $s \in \mathbb{R}$, the matrices of A and S are given by

$$A = \begin{pmatrix} a & 0 \\ 0 & \sqrt{a} \end{pmatrix}, \quad (8)$$

$$S = \begin{pmatrix} 1 & s \\ 0 & 1 \end{pmatrix}.$$

Let $a = 4$ and $s = 1$, from (8), be further modified:

$$A = \begin{pmatrix} 4 & 0 \\ 0 & 2 \end{pmatrix}, \quad (9)$$

$$S = \begin{pmatrix} 1 & 1 \\ 0 & 1 \end{pmatrix}.$$

For $\forall \xi = (\xi_1, \xi_2) \in \widehat{\mathbb{R}}^2$, $\xi_1 \neq 0$, the mathematical expression of basic function $\widehat{\psi}^{(0)}$ for shearlet transform can be given according to [11]

$$\widehat{\psi}^{(0)}(\xi) = \widehat{\psi}^{(0)}(\xi_1, \xi_2) = \widehat{\psi}_1(\xi_1) \widehat{\psi}_2\left(\frac{\xi_2}{\xi_1}\right), \quad (10)$$

where $\widehat{\psi}$ is the Fourier transform of ψ , $\widehat{\psi}_1 \in C^\infty(\mathbb{R})$ and $\widehat{\psi}_2 \in C^\infty(\mathbb{R})$ are both wavelets, and supplement $\psi_2 \subset [-1/2, -1/16] \cup [1/16, 1/2]$, $\text{supp } \widehat{\psi}_2 \subset [-1, 1]$. It implies that $\widehat{\psi}_0 = C^\infty(\mathbb{R})$ and compactly supported with $\text{supp } \psi_0 \subset [-1/2, 1/2]^2$. In addition, we assume that

$$\sum_{j \geq 0} |\widehat{\psi}_1(2^{-2j}\omega)|^2 = 1, \quad |\omega| \geq \frac{1}{8}, \quad (11)$$

and for each $j \geq 0$, $\widehat{\psi}_2$ satisfies

$$\sum_{l=-2^j}^{2^j-1} |\widehat{\psi}_2(2^j\omega - l)| = 1, \quad |\omega| \leq 1. \quad (12)$$

From the conditions on the support of $\widehat{\psi}_1$, and $\widehat{\psi}_2$, one can obtain that function $\psi_{j,l,k}$ has the frequency support listed in

$$\text{supp } \widehat{\psi}_{j,l,k}^0 \subset \left\{ \xi_1, \xi_2 \left| \xi_1 \in [-2^{2j-1}, -2^{2j-4}] \right. \right. \\ \left. \left. \cup [-2^{2j-4}, -2^{2j-1}], \left| \frac{\xi_2}{\xi_1} + l2^{-j} \right| \leq 2^{-j} \right\}. \quad (13)$$

That is, each element $\widehat{\psi}_{j,l,k}$ is supported on a pair of trapeziform zones, whose sizes all approximate to $2^{2j} \times 2^j$. The tiling of the frequency by shearlet and the size of the frequency support $\psi_{j,l,k}$.

In NSST algorithm, in order to remove the influence of upsampling and subsampling, nonsampled Laplacian pyramid filters are used as a substitute in the shearlet transform, so it has excellent performance in terms of shift-invariance, multiscale, and multidirectional properties. The discretization process of NSST has two phases: multiscale factorization and multi-directional factorization. Nonsampled Laplacian pyramid filters complete multiscale factorization. The first phase uses k classes two-channel nonsampled filter to get one low frequency image and

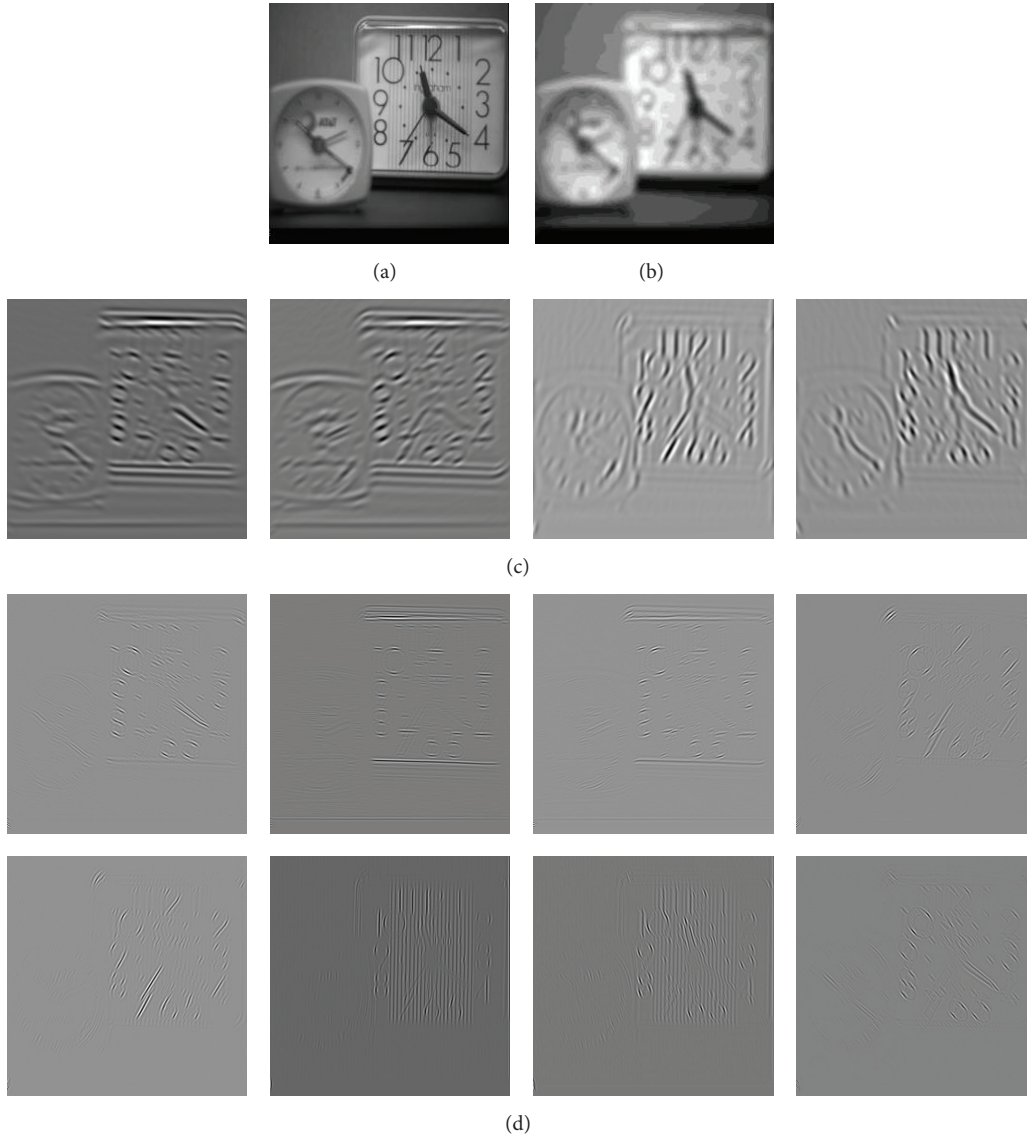


FIGURE 2: An illustration of NSST. (a) Source image. (b) The approximate NSST coefficients. (c) Images of the detailed coefficients at level 1. (d) Images of the detailed coefficients at level 2.

k high frequency images. The multidirectional factorization in NSST is realized via improved shearlet transform. These filters are formed by avoiding the subsampling to satisfy the property of shift-invariance. Shearlet transform allows the direction decomposition with l stages in high frequency images from nonsubsampled Laplacian pyramid at each level and produces 2^l directional subimages with the same size as the source image [16, 17]. Figure 2 shows the two-level NSST decomposition of an image.

3. The Proposed Algorithm

In this section, the proposed multifocus color image fusion algorithm is presented in detail. The framework of the proposed algorithm is shown in Figure 3. In this algorithm, the RGB color images are transformed into HSV color space

[18], NSST is used to decompose the image and PCNN is used to extract the features and fuse these features using different rules. Besides, it is important to note that two kinds of PCNN model are used in the algorithm; adaptive S-PCNN is used to fuse H component and original PCNN is used to fuse high frequency coefficients of NSST.

3.1. RGB Color Image Transform to HSV. RGB color image contains almost all basic colors that can be perceived by human vision; however, the correlation among the components is very strong; it is shown in Figures 4(b), 4(c), and 4(d); this makes it difficult for RGB color image to deal with the fact that the color of the image will be changed if a component changes. HSV image can be obtained by the RGB transform. The values of R, G, and B correspond to unique H, S, and V values, as the values of H, S, and V components depend on the

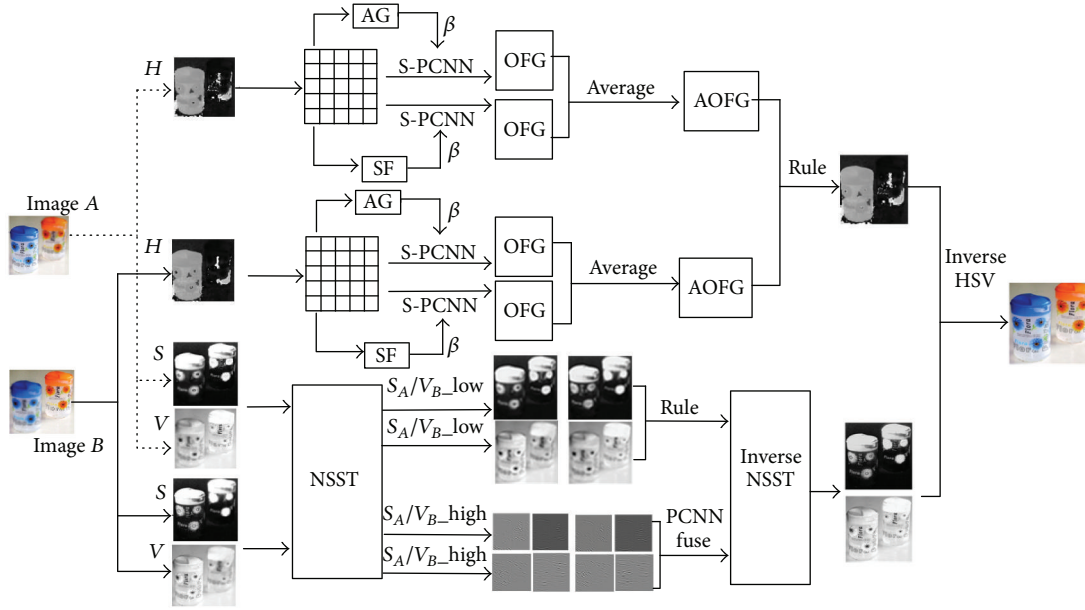


FIGURE 3: The schematic diagram of the proposed image fusion method.

values of R, G, and B in RGB color space. This color system is closer than the RGB color system to human experience and perception of the color; this is shown in Figures 4(e), 4(f), and 4(g).

The distribution of H component is concentrated, and its pixel value generally is small; see Figure 4(h). So its edge is obvious, and S-PCNN is sensitive to edge and regional distribution of the image. In this algorithm, H component is partitioned into blocks and input into adaptive S-PCNN to get OFG of the H component; we fuse the H component according to the OFG. The distribution of S and V components is dispersive; see Figures 4(i) and 4(j), which contain lots of details of the image in different grayscale, so S and V components are decomposed into multiscale and multidirectional subband by NSST to get different information of the images, and then according to the characters of new S and V components, new S and V components are fused using different rules.

3.2. H Component Fusion Using Adaptive S-PCNN. β is the linking strength of S-PCNN, and it is a key determinant to the ignition behavior of S-PCNN. Spatial frequency (SF) and average gradient (AG) are very important indicators of the image definition, which represent the quality of the image. So S-PCNN should be adaptively adjusted by SF and AG to make it work well. In S-PCNN model, H component is divided into several blocks, and then SF and AG of the blocks are calculated as linking strength β of S-PCNN, respectively, so this can adaptively adjust β of S-PCNN; see (14) and (15). The block images are input into S-PCNN to get two kinds of OFG according to different β , which can effectively express the quality of the block images. The two types of indexes will change with the content of the image and produce a certain range of changes. The index itself and its change range are

suitable for adjusting the parameter β of S-PCNN, which can affect the OFG of S-PCNN, so that the two types of OFG can reflect different details of the image. If one type of OFG is only used, as the size of OFG for different quality of pixel is the same, this cannot select appropriate pixels. However, the combination of two types OFG can reflect the image information from different angles; thus, this reduces the possibility of different pixels with the same OFG. It can make the algorithm more effective.

SF and AG of the image are described in (16) to (19):

$$\beta_1 = \eta_1 * SF, \quad (14)$$

$$\beta_2 = \eta_2 * AG, \quad (15)$$

where η is adjusted factor. Consider

$$SF = \sqrt{RF^2 + CF^2}, \quad (16)$$

$$RF = \sqrt{\frac{1}{M \times N} \sum_{i=1}^M \sum_{j=2}^N [F(i, j) - F(i, j-1)]^2}, \quad (17)$$

$$CF = \sqrt{\frac{1}{M \times N} \sum_{i=1}^M \sum_{j=2}^N [F(i, j) - F(i, j-1)]^2}. \quad (18)$$

SF is composed of row frequency (RF) and column frequency (CF), where M is the row of the image, N is the column of the image, and $F(i, j)$ is grey level of the image F at pixel (i, j) :

$$AG = \frac{1}{M \times N} \cdot \sum_{i=1}^M \sum_{j=1}^N \sqrt{\frac{1}{2} ((F(i, j) - F(i+1, j))^2 + (F(i, j) - F(i, j+1))^2)}. \quad (19)$$

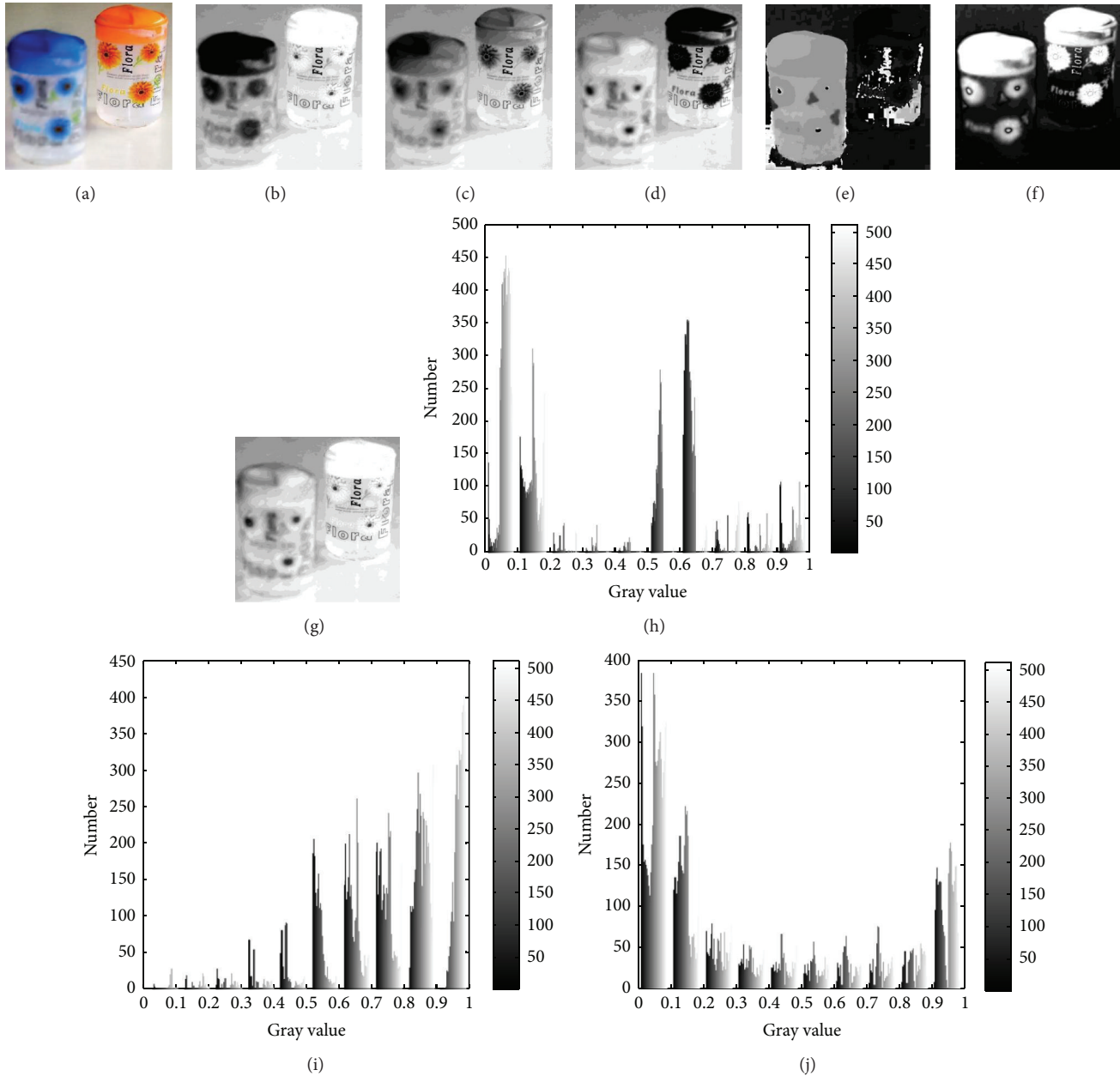


FIGURE 4: An illustration of HSV. (a) Source image. (b) R component. (c) G component. (d) B component. (e) H component. (f) S component. (g) V component. (h) Histogram of H. (i) Histogram of S. (j) Histogram of V.

3.3. S and V Components Fusion Using NSST and PCNN.

S and V components contain lots of details of the image, and the gray values of S and V components are dispersive, respectively. S and V components are decomposed by NSST to make it easy to extract, and then we will get one low frequency subband and several high frequency subbands in multiscale and multidirection. The higher values of the low frequency coefficients are used into the new fused low frequency subband. The high frequency subbands contain abundant detailed information of the S and V components; these components are input into original PCNN model to get OFG, which shows the statistics of the ignition times of the pixels. Compared with the OFG of the high frequency

subbands from different S and V components, we will get the new fused high frequency subbands. At last, inverse NSST is performed to get the fused S and V components according to the new fused low frequency subbands and high frequency subbands.

3.4. Algorithm Steps. The proposed fusion algorithm processes are shown in Figure 3, and the steps are as follows.

Step 0. Given source images A and B .

Step 1. The color image in RGB color space is converted to HSV color space to get three components H, S, and V.

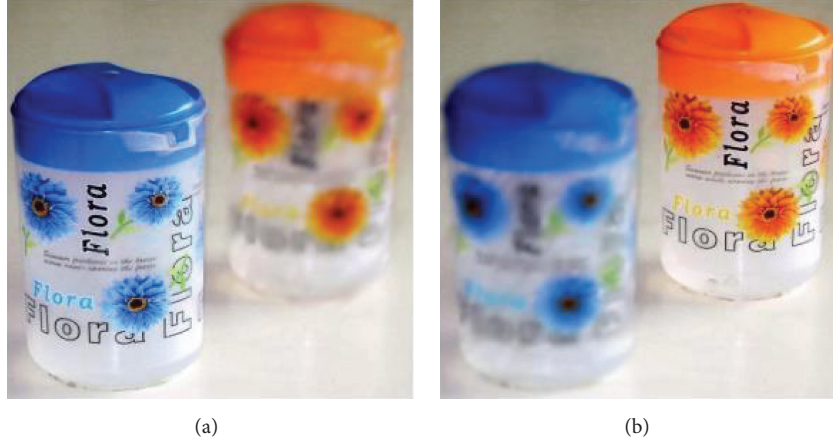


FIGURE 5: Source images. (a) Source image A. (b) Source image B.

Step 2. PCNN is utilized to deal with H component:

- (a) The H components of images A_{ij} and B_{ij} are divided into subblocks, and then the SF and AG of the subblocks are calculated using (16) to (19); the linking strengths β_1 and β_2 are gotten using (14) and (15); β_1 and β_2 acted as β value of S-PCNN, respectively.
- (b) The subblocks are input into S-PCNN model twice with different β to get two OFGs of the H components.
- (c) Get the average value of two OFGs using (20), and then F_{ij} of the fused H component can be decided by (21):

$$\text{AOFG} = \frac{(\text{OFG}_{\beta_1} + \text{OFG}_{\beta_2})}{2}, \quad (20)$$

$$F_{ij} = \begin{cases} A_{ij}, & (\text{AOFG}_{A_{ij}} > \text{AOFG}_{B_{ij}}), \\ B_{ij}, & (\text{AOFG}_{A_{ij}} < \text{AOFG}_{B_{ij}}), \\ \frac{(A_{ij} + B_{ij})}{2}, & (\text{AOFG}_{A_{ij}} = \text{AOFG}_{B_{ij}}), \end{cases} \quad (21)$$

where $\text{AOFG}_{A_{ij}}$ and $\text{AOFG}_{B_{ij}}$ are the average OFG of images A and B.

Step 3. Perform decomposition of source S and V components of image A_{ij} and B_{ij} using NSST to obtain the low-pass subband coefficients and the high-pass directional subband coefficients; different rules are utilized to deal with the S and V components.

- (a) The fused low-pass subband coefficients FC_{ij} can be decided by

$$FC_{ij} = \begin{cases} C_{A_{ij}}, & (C_{A_{ij}} > C_{B_{ij}}), \\ C_{B_{ij}}, & (C_{A_{ij}} < C_{B_{ij}}), \\ \frac{(C_{A_{ij}} + C_{B_{ij}})}{2}, & (C_{A_{ij}} = C_{B_{ij}}), \end{cases} \quad (22)$$

where $C_{A_{ij}}$ and $C_{B_{ij}}$ is the low-pass subband coefficients of images A and B.

- (b) The high-pass directional subband coefficients are input into PCNN model to get corresponding OFGs ($\text{OFG}_{A_{ij}}$, $\text{OFG}_{B_{ij}}$) according to the statistics of the ignition times of the pixels; the fusion rule of S and H components can be decided by

$$F_{ij} = \begin{cases} A_{ij}, & (\text{OFG}_{A_{ij}} > \text{OFG}_{B_{ij}}), \\ B_{ij}, & (\text{OFG}_{A_{ij}} < \text{OFG}_{B_{ij}}), \\ \frac{(A_{ij} + B_{ij})}{2}, & (\text{OFG}_{A_{ij}} = \text{OFG}_{B_{ij}}). \end{cases} \quad (23)$$

Step 4. Reconstruct the fused HSV image by an inverse NSST.

Step 5. Obtain the fused RGB color image by inverse HSV.

4. Experimental Results and Analysis

To verify the validity of the algorithm presented in this paper, we take several groups of experimental color images with different focus position test. The first group of color image is cups, which is shown in Figure 5. Image A focuses on the left and image B focuses on the right, and there are many words as details.

4.1. Evaluation Index System. In order to verify the effectiveness of this method, we consider the quantitative assessment of the fused images. For evaluation of the proposed fusion method, we have considered several common fusion performance metrics defined in this section. The final fused color images are composed of three components such as R, G, and B. Each component can be regarded as a grayscale image, and the quality of the fused color image strongly depends on the grayscale image quality. In this paper, we take the average of the three component's evaluation indexes as the final color image evaluation index, which is the basic indicators of image

TABLE 1: Fusion quality using different methods.

Method	SF	AG	EN	MV	SD	MI	Q^{ABF}
Weighted	12.7859	4.2004	7.4416	166.7102	65.1893	5.4941	0.5449
PCA	13.0306	4.2311	7.4408	166.5136	65.3166	5.5144	0.5525
PCNN	16.8538	4.9683	7.4449	167.3324	65.8106	5.5454	0.5986
PCNN + WT	17.7381	5.2384	7.2349	143.0606	57.6579	5.1952	0.6696
PCNN + LP	18.8702	5.4816	7.3187	150.6954	61.1962	5.2172	0.6795
This paper (HSV)	20.3181	5.8530	7.4487	175.4014	61.6361	5.6377	0.6886

TABLE 2: Fusion quality under different color spaces.

Color spaces	SF	AG	EN	MV	SD	MI	Q^{ABF}
NTSC	19.1768	5.5980	7.4530	171.1844	66.1808	5.8862	0.6547
YUV	19.1937	5.5983	7.4382	171.1177	66.2103	5.9109	0.6555
YCbCr	19.1805	5.6076	7.4743	171.6032	65.4123	5.7668	0.6496
HSV	20.3181	5.8530	7.4487	175.4014	61.6361	5.6377	0.6886
HIS	20.4130	5.8660	7.3967	172.0959	68.2812	5.8896	0.6989
LAB	20.5100	5.9280	7.42820	172.4920	67.6792	6.0364	0.7018

fusion quality. Tables 1 and 2 show the evaluation of the fused image quality with space frequency (SF), average gradient (AG), entropy (EN), mean value (MV), standard deviation (SD), and mutual information (MI), and Q^{ABF} indicates how much edge information is reserved in the fused image [19–23].

The space frequency (SF) is defined by (16) to (18), and the average gradient is defined by (19).

4.1.1. *Entropy.* The entropy (EN) of an image is defined by

$$H = - \sum_{i=0}^{L-1} P_i \log_2 P_i, \quad (24)$$

where P_i is the probability of the gray level i in the image and L is the gray level of the image from 0 to 255.

4.1.2. *Mean Value.* The mean value (MV) of the image is defined by

$$\mu = \frac{1}{M \times N} \sum_{i=1}^M \sum_{j=1}^N F(i, j), \quad (25)$$

where $F(i, j)$ is the pixel value of the fused image at the position (i, j) . MV represents the average brightness of the whole image.

4.1.3. *Standard Deviation.* The standard deviation (SD) of an image is defined by

$$SD = \sqrt{\frac{1}{M \times N} \sum_{i=1}^M \sum_{j=1}^N (F(i, j) - \mu)^2}, \quad (26)$$

where $F(i, j)$ is the pixel value of the fused image at the position (i, j) and μ is the mean value of the image. The larger the SD is, the better the result is.

4.1.4. *Mutual Information.* The mutual information MI between the source images A and B and the fused image F is defined by

$$MI = \sum_{i=0}^{L-1} \sum_{j=0}^{L-1} \sum_{k=0}^{L-1} P_{ABF}(i, j, k) \log_2 \frac{P_{ABF}(i, j, k)}{P_{AB}(i, j) P_F(k)}, \quad (27)$$

where $P_{ABF}(i, j, k)$ is the normalization union grey level histogram of images A and B and F , $P_{AB}(i, j)$ is the normalization union grey level histogram of images A and B , $P_F(k)$ is the normalization grey level histogram of F , L is the gray level of the image, and (i, j, k) represents the pixel value of images A and B and F , respectively.

4.1.5. *Edge Based on Similarity Measure.* The Q^{ABF} metric evaluates the sum of edge information preservation values and is defined by

$$Q^{ABF} = \left(\sum_{i=1}^M \sum_{j=1}^N (Q^{AF}(i, j) \times \omega_A(i, j) + Q^{BF}(i, j) \times \omega_B(i, j)) \right) \cdot \left(\sum_{i=1}^M \sum_{j=1}^N (\omega_A(i, j) + \omega_B(i, j)) \right)^{-1}, \quad (28)$$

where $Q^{AF}(i, j) = Q_{\beta}^{AF}(i, j) Q_{\alpha}^{AF}(i, j)$, $Q_{\beta}^{AF}(i, j)$, $Q_{\alpha}^{AF}(i, j)$, and $Q_{\alpha}^{AF}(i, j)$ are the edge strength and orientation preservation values, respectively, $Q^{BF}(i, j)$ is similar to $Q_{\beta}^{AF}(i, j)$, and $\omega_A(i, j)$ and $\omega_B(i, j)$ are weights to measure the importance of $Q_{\alpha}^{AF}(i, j)$ and $Q^{BF}(i, j)$, respectively. The dynamic range Q^{ABF} is $[0, 1]$, and it should be close to 1 as far as possible for the best fusion, as $Q^{ABF} = 1$. In addition, (i, j) represents the pixel location, and M and N are the sizes of images, respectively.



FIGURE 6: Fusion images from different methods. (a) Average method. (b) PCA method. (c) PCNN method. (d) PCNN + WT. (e) PCNN + LP. (f) This paper.

4.2. Experiment One. For comparison, this paper proposes the fusion scheme of the algorithm and presents several common fusion algorithms; for instance, take the average of the source images pixel by pixel (average), principal component analysis (PCA), pulse coupled neural network (PCNN), pulse coupled neural network and Laplacian pyramid transform (PCNN + LP), and pulse coupled neural network and discrete wavelet transform (PCNN + WT). The fusion images using different methods are shown in Figure 6. According to the contrast experiments, the fusion image of this paper is better than the others; see Figure 6. The algorithm of this paper does well in extracting the characteristics of the source images, and the fused image is closer to the natural color, which contains more edges, texture, and detail, so it is the closest to the source images. We can conclude that the method in this paper is an effective method.

From Table 1, the fusion image of this paper contains much more information. SF, AG, MV, and Q^{ABF} of this paper are larger than other methods, EN and MI are slightly better than other methods, and only SD is less than other methods.

4.3. Experiment Two. In other color spaces such as NTSC, YUV, YCbCr, HIS, and LAB, all have the similar histogram

distribution as the distribution of H, S, and V components in HSV color space, so all can use the proposed algorithm for color image fusion. In order to confirm the method that works best under the color space of fusion, we carry out the following experiments. The fusion images under different color space are shown in Figure 7; all can achieve the goal of the image fusion, but the fusion effects on HSV, HIS, and LAB color spaces are better than others.

From Table 2, it is indicated that the fusion image of this paper in LAB color space contains more information, and SF, AG, MI, and Q^{ABF} are better than others. Overall, the evaluation indexes in HSV, HIS, and LAB are better than others. In practical application, we suggest that the color image fusion of the proposed algorithm should focus on HSV, HIS, and LAB color spaces.

4.4. Experiment Three. More experimental results of coastal images in HSV color space are shown in Figure 8, the source images with different focus position, and there are a lot of textures in the source images.

It can be seen in Figure 8 that the edge of the fusion image is clear, and it retains most of the textures in the source images; besides, the details are also well preserved. This



FIGURE 7: Fusion images under different color spaces. (a) NTSC. (b) YUV. (c) YCbCr. (d) HSV. (e) HIS. (f) LAB.

method can extract the main features from the source images; it shows that the method in this paper also achieved effective results in these groups of color images.

The same conclusion as in Figure 6 can be concluded. Overall, the method presented in this paper is better than the traditional methods obviously. Compared with the other methods, this method reflects better performance and visual effect in terms of definition and detail.

5. Conclusions

We propose an effective multisensor color image fusion algorithm based on NSST and PCNN. PCNN's neurons capture character will cause the similar brightness of the surrounding neurons to capture the ignition. This character can be automatically coupled and transmitted information. Nonsubsampled Laplacian pyramid filters are used in NSST to remove the influence of upsampling and subsampling. NSST has excellent performance in terms of shift-invariance, multiscale, and multidirectional properties. In the proposed algorithm, RGB color image is converted into HSV color image. H component is fused by adaptive S-PCNN; S and V components are decomposed into different frequency subbands according to different scales and direction by

NSST and are fused by different rules. The experimental results show that the proposed color image fusion algorithm can fuse different focus position of the color images, and the fused image contains more information about color, texture, and detail. Compared with the traditional algorithms, this method embodies better fusion performance in many aspects. The paper also discusses the effect of the proposed algorithm on other color spaces, and the experiments show that the algorithm achieved better effects under HSV, HIS, and LAB color spaces, and we recommend three kinds of color spaces as the practical application color space.

Conflict of Interests

The authors declare that there is no conflict of interests regarding the publication of this paper.

Acknowledgments

The authors thank the editors and the anonymous reviewers for their careful works and valuable suggestions for this paper. The authors wish to express their gratitude

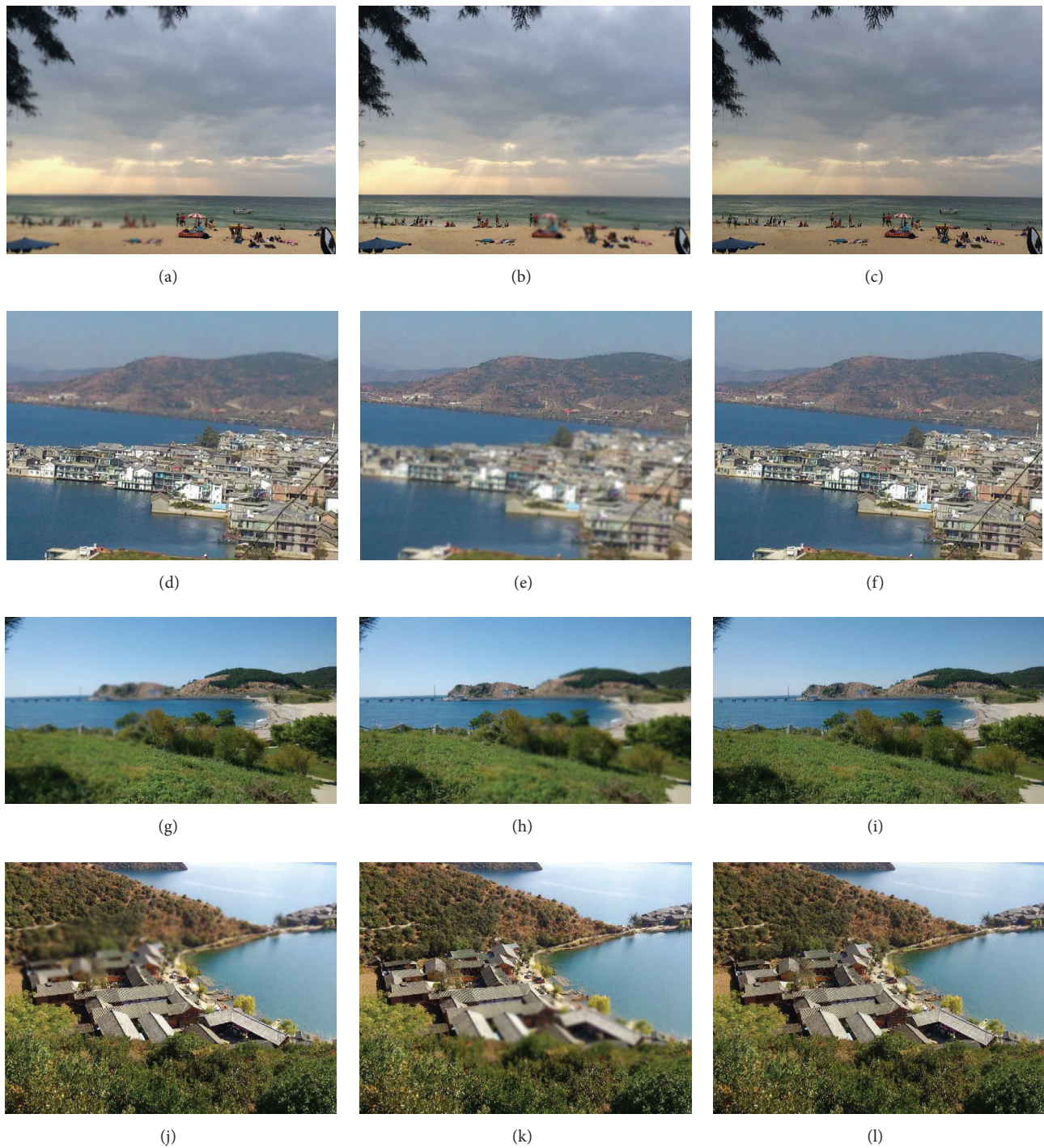


FIGURE 8: The fusion results of the coastal images. (a) Source image A. (b) Source image B. (c) Fusion image. (d) Source image A. (e) Source image B. (f) Fusion image. (g) Source image A. (h) Source image B. (i) Fusion image. (j) Source image A. (k) Source image B. (l) Fusion image.

to Zijun Wang, Shanshan Du, Jingxue Xu, and Shujuan Zhang for providing coastal images. The authors' work is supported by the National Natural Science Foundation of China (no. 61365001 and no. 61463052), the Natural Science Foundation of Yunnan Province (no. 2012FD003), and the Science and Technology Plan of Yunnan Province (no. 2014AB016).

References

- [1] V. Petrović and V. Dimitrijević, "Focused pooling for image fusion evaluation," *Information Fusion*, vol. 22, pp. 119–126, 2015.
- [2] Y. Xia and Sh. R. Qu, "Color image fusion framework based on improved (2D)2PCA," *Acta Optica Sinica*, vol. 34, no. 10, Article ID 1010001, 2014 (Chinese).

- [3] R. H. Miao, J. L. Tang, and X. Q. Chen, "Classification of farmland images based on color features," *The Journal of Visual Communication and Image Representation*, vol. 29, pp. 138–146, 2015.
- [4] S. Daneshvar and H. Ghassemian, "MRI and PET image fusion by combining IHS and retina-inspired models," *Information Fusion*, vol. 11, no. 2, pp. 114–123, 2010.
- [5] M. González-Audicana, J. L. Saleta, R. G. Catalán, and R. García, "Fusion of multispectral and panchromatic images using improved IHS and PCA mergers based on wavelet decomposition," *IEEE Transactions on Geoscience and Remote Sensing*, vol. 42, no. 6, pp. 1291–1299, 2004.
- [6] Y. Xin and L. Deng, "An improved remote sensing image fusion method based on wavelet transform," *Laser & Optoelectronics Progress*, vol. 50, no. 2, 2013.
- [7] E. J. Candes and D. L. Donoho, "Curvelets: a surprisingly effective nonadaptive representation of objects with edges," in *Curves and Surfaces Fitting*, pp. 105–120, Vanderbilt University Press, Nashville, Tenn, USA, 2000.
- [8] M. N. Do and M. Vetterli, *Contourlets Beyond Wavelets*, edited by: G. V. Welland, Academic Press, 2003.
- [9] D. Labate, W.-Q. Lim, G. Kutyniok, and G. Weiss, "Sparse multidimensional representation using shearlets," in *Wavelets XI*, vol. 5914 of *Proceedings of SPIE*, pp. 254–262, San Diego, Calif, USA, September 2005.
- [10] Z.-Y. Fan, Q.-S. Sun, Z.-X. Ji, and K. Hu, "An image filter based on multiobjective genetic algorithm and shearlet transformation," *Mathematical Problems in Engineering*, vol. 2013, Article ID 463760, 7 pages, 2013.
- [11] G. Easley, D. Labate, and W.-Q. Lim, "Sparse directional image representations using the discrete shearlet transform," *Applied and Computational Harmonic Analysis*, vol. 25, no. 1, pp. 25–46, 2008.
- [12] W. Kong, L. Zhang, and Y. Lei, "Novel fusion method for visible light and infrared images based on NSST-SF-PCNN," *Infrared Physics and Technology*, vol. 65, pp. 103–112, 2014.
- [13] R. C. Nie, D. M. Zhou, M. He, X. Jin, and J. Yu, "Facial feature extraction using frequency map series in PCNN," *Journal of Sensors*, In press.
- [14] M. M. Subashini and S. K. Sahoo, "Pulse coupled neural networks and its applications," *Expert Systems with Applications*, vol. 41, no. 8, pp. 3965–3974, 2014.
- [15] C. H. Zhao, G. F. Shao, L. J. Ma, and X. Zhang, "Image fusion algorithm based on redundant-lifting NSWMDA and adaptive PCNN," *Optik*, vol. 125, no. 20, pp. 6247–6255, 2014.
- [16] W. W. Kong, L. J. Zhang, and Y. Lei, "Novel fusion method for visible light and infrared images based on NSST-SF-PCNN," *Infrared Physics & Technology*, vol. 65, pp. 103–112, 2014.
- [17] M. Yuan, B. X. Yang, Y. D. Ma, J. Zhang, R. Zhang, and C. Zhang, "Compressed sensing MRI reconstruction from highly under-sampled k -space data using nonsubsampling shearlet transform sparsity prior," *Mathematical Problems in Engineering*, vol. 2015, Article ID 615439, 18 pages, 2015.
- [18] J.-F. Pekel, C. Vancutsem, L. Bastin et al., "A near real-time water surface detection method based on HSV transformation of MODIS multi-spectral time series data," *Remote Sensing of Environment*, vol. 140, pp. 704–716, 2014.
- [19] L. M. Dong, Q. X. Yang, H. Y. Wu, H. Xiao, and M. Xu, "High quality multi-spectral and panchromatic image fusion technologies based on Curvelet transform," *Neurocomputing*, vol. 159, pp. 268–274, 2015.
- [20] M. J. Kim, D. K. Han, and H. Ko, "Joint patch clustering-based dictionary learning for multimodal image fusion," *Information Fusion*, vol. 27, pp. 198–214, 2016.
- [21] P. Zhang, C. Fei, Z. M. Peng et al., "Multifocus image fusion using biogeography-based optimization," *Mathematical Problems in Engineering*, vol. 2015, Article ID 340675, 14 pages, 2015.
- [22] S. T. Li, J. T. Kwok, and Y. N. Wang, "Combination of images with diverse focuses using the spatial frequency," *Information Fusion*, vol. 2, no. 3, pp. 169–176, 2001.
- [23] J. Cheng, H. J. Liu, T. Liu, F. Wang, and H. Li, "Remote sensing image fusion via wavelet transform and sparse representation," *ISPRS Journal of Photogrammetry and Remote Sensing*, vol. 104, pp. 158–173, 2015.

Research Article

Application of X-Band Wave Radar for Coastal Dynamic Analysis: Case Test of Bagnara Calabria (South Tyrrhenian Sea, Italy)

Michele Punzo,¹ Chiara Lanciano,² Daniela Tarallo,¹ Francesco Bianco,² Giuseppe Cavuoto,¹ Rosanna De Rosa,² Vincenzo Di Fiore,¹ Giuseppe Cianflone,² Rocco Dominici,² Michele Iavarone,¹ Fabrizio Lirer,¹ Nicola Pelosi,¹ Laura Giordano,¹ Giovanni Ludeno,³ Antonio Natale,³ and Ennio Marsella¹

¹*Institute for Coastal Marine Environment (IAMC), Italian National Research Council (CNR), Calata Porta di Massa, Porto di Napoli, 80133 Naples, Italy*

²*Earth Science Department, University of Calabria, Via P. Bucci, Arcavacata di Rende, 87036 Cosenza, Italy*

³*Institute for Electromagnetic Sensing of the Environment (IREA), Italian National Research Council (CNR), Via Diocleziano 328, 80124 Naples, Italy*

Correspondence should be addressed to Michele Punzo; michele.punzo@iamc.cnr.it

Received 17 July 2015; Revised 5 October 2015; Accepted 11 October 2015

Academic Editor: Jose C. Nieto-Borge

Copyright © 2016 Michele Punzo et al. This is an open access article distributed under the Creative Commons Attribution License, which permits unrestricted use, distribution, and reproduction in any medium, provided the original work is properly cited.

Sea state knowledge has a key role in evaluation of coastal erosion, the assessment of vulnerability and potential in coastal zone utilization, and development of numerical models to predict its evolution. X-band radar measurements were conducted to observe the spatial and temporal variation of the sea-state parameters along a 3 km long sandy-gravelly pocket beaches forming a littoral cell on Bagnara Calabria. We produced a sequence of 1000 images of the sea state extending offshore up to 1 mile. The survey has allowed monitoring the coastline, the directional wave spectra, the sea surface current fields, and the significant wave heights and detecting strong rip currents which cause scours around the open inlets and affect the stability of the submerged reef-type breakwaters. The possibility to validate the data acquired with other datasets (e.g., LaMMA Consortium) demonstrates the potential of the X-band radar technology as a monitoring tool to advance the understanding of the linkages between sea conditions, nearshore sediment dynamics, and coastal change. This work proves the possibility to obtain relevant information (e.g., wave number, period, and direction) for evaluation of local erosion phenomena and of morphological changes in the nearshore and surf zone.

1. Introduction

Coastal areas are dynamic and changing environments, extremely sensitive to sea-land interactions and to hydrodynamic and sedimentary processes which both act on different temporal scale: short-times (tides, waves, currents, and winds) and larger temporary scales (sea level fluctuating during glacial and interglacial phases).

The sediment movement induced by wave motion, currents, tides, and meteomarine events produces deep and incisive changes in these zones. Seasonally, these areas are subject to extreme morphological changes as continuous

settlements of the shoreline and natural beach nourishment/retreat. Therefore, the study of the evolution trends of the coastal marine areas has become an indispensable tool to evaluate the quality and the degradation of these environments through the analysis of the marine currents, the effects of high-impact meteomarine events, and the consequent morphological variations.

In the last two decades, the use of remote sensing (e.g., satellite and SAR) allowed examining in real time the coastal morphodynamic and the morphological variations after storms to obtain a complete knowledge of the coastal system that allows an optimized management [1, 2].

Among the remote sensing techniques, the X-Band Wave Radars provide an alternative to the standard detection systems of the sea state (e.g., buoys and others) with some important advantages. It has a good operating flexibility resulting in a “plug and play” system situated on a mobile platform. If compared to traditional sea state systems monitoring, the X-Band Wave Radar is easier to install, manage, and maintain; the system returns real-time motion waves, wind field data, and near-surface current, usually underestimated by the traditional systems. The X-Band Wave Radar acquires sea state parameters such as wavelength, period and direction of the waves and the values of the significant wave heights, sea surface current fields, and the maps of the distribution of the wind on the sea surface. These data are useful for the reconstruction of the meteomarine climatology of the coastal sector but also for acquiring the bathymetric features and the morphologies of the seabed [3].

In general, the X-Band Radar system analyzes phenomena that occur on different scales of space and time: small-scale phenomena (transient phenomena as wave breaking interactions over the shallows morphology or structures, or rip currents observation linked to the sharp contrast dominant wave and superficial currents, bar movements during storms, and submerged structure interactions) and long scale phenomena (e.g., developing predictive models of coastal erosion and planning/monitoring the coastal defense works). Therefore, the system allows performing the accurate characterization of the meteomarine climatology of particular coastal sector without having to carry out the transposition of the data that, acquired through buoys, are almost always recorded in locations very distant from the site of study.

In many cases, it has been shown that the radar system is useful in assessing the effectiveness of the coastal defense works and in validating the level of exposure of the coast [4, 5].

In the radar images, in fact, the phenomena of interaction between the wave motion and the anthropogenic infrastructures (reflection and diffraction of the waves and rip currents) and between waves and seabed (refraction, shoaling, and wave breaking) are immediately visible. This latter aspect is particularly important because the system allows inferring valuable information for reproducing the beach morphology and for bathymetric reconstruction [4].

This paper presents an example of application of the X-Band Wave Radar under the actions of “Coastal Monitoring” provided in the SIGIEC PON Project (Integrated Management System for Coastal Erosion) [6], realized by the University of Calabria in partnership with some companies and with the National Research Council (IAMC and ISAC).

In general, the project studies causes and effects of erosion phenomena affecting beaches located in sample areas in the Italian regions of Calabria and Puglia, testing measures for its containment and developing quantitative methods for producing, evaluating, and implementing a correct coastal management policy.

For the choice of the test sites, a qualitative analysis integrating geomorphologic and weather-marine dataset taking into account the landscape and structural restrictions was preliminarily performed; this has allowed identifying

some macroareas which are subdivided into sedimentary cells.

Inside one of the sedimentary cells, some experimental sites have been selected to run tests of potential antierosion systems: among these sites, there is the coastal area of Bagnara Calabria (RC).

Four days of X-Band Wave Radar data, 24–27 February 2015, have been analyzed using the Remocean system developed at IREA-CNR.

A sequence of 1000 images of the sea state within one mile from the coast were produced. These images contain information regarding the wave field and its variation in time on a local scale.

2. Observation and Data Processing

2.1. Study Area and X-Band Radar REMOCEAN System. The study area of this research focuses on Bagnara Calabria village located in the western part of Calabria coast, southern Italy, facing Tyrrhenian Sea.

The study area is located in a sector of the “Costa Viola” mountain ridge, between Bagnara Calabria and Scilla (Figure 1).

From a morphological point of view, steep and uneven slopes, cut by deep canyons, characterize the test area in emerged sector [7]. Cliffs surrounding pocket gravel-sandy beaches are nourished by short high gradient torrents (the longest thereof are Favazzina and Sfalassà) which drain the western slope of the ridge. In the submerged sector, a discontinuous littoral wedge (LW in Figure 6), extending from coastline to 200 m offshore, characterizes the central part of site. Three channels indenting the LW as result of several coalescing landslide scars (up to 50–100 m wide) suggest very recent erosion [8]. In particular, the test area is connotated by coast-parallel erosion probably related to long shore currents and rip currents, which have formed shelf sand waves and small slope ward erosional channels, respectively [9]. Moreover, present day shoreline erosion is probably related to breakwaters structural defects.

There is a high percentage of high coast, with significant values of the wave energy flow concentrated around the sectors from the northwest, which are characterized by fetches with remarkable extension (over one thousand kilometers, along certain directions) [10].

Coastal erosion has been a serious problem for the entire coast of Calabria region, especially for its southwestern part. This area has been hit several times by coastal storms of high magnitude (e.g., 1928, 1980, 1984, 1985, 1986, 1987, 2008, and 2012), reef-type breakwaters have been built to protect the town center between the mouth of the Sfalassà Torrent and Promontory of Marturano (Figure 2). Regarding coastal erosion, the critical points are all areas, also with breakwaters and especially the beach situated at the south of Sfalassà Torrent, Promontory of Marturano, and Promontory of Cacili [10].

2.2. X-Band Radar Method. Retrieving information on the wave motion through X-Band Radar devices requires the processing of a temporal sequence of marine radar images. Such a processing is aimed at compensating the distortions

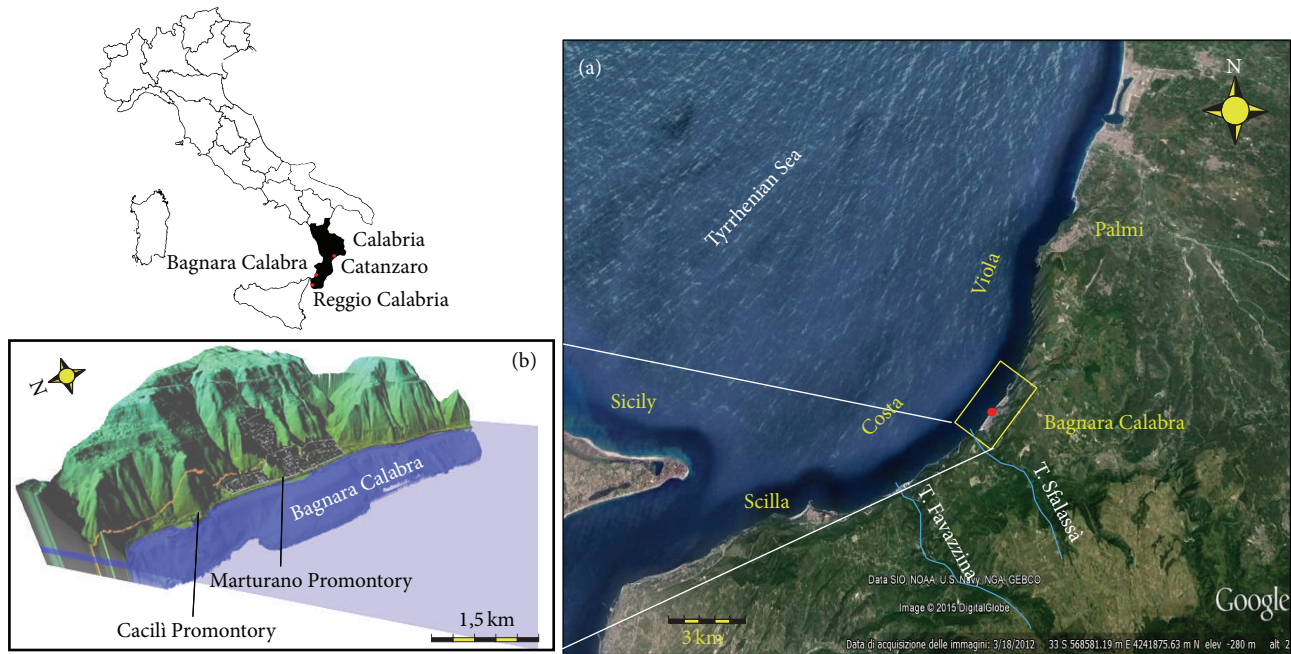


FIGURE 1: Bagnara Calabria village is located in the Italian region of Calabria at about 100 kilometers southwest of Catanzaro and about 25 kilometers northeast of Reggio Calabria. (a) Costa Viola geographical position; the red dot indicates the position of X-Band Radar antenna. (b) DEM of Bagnara Calabria.

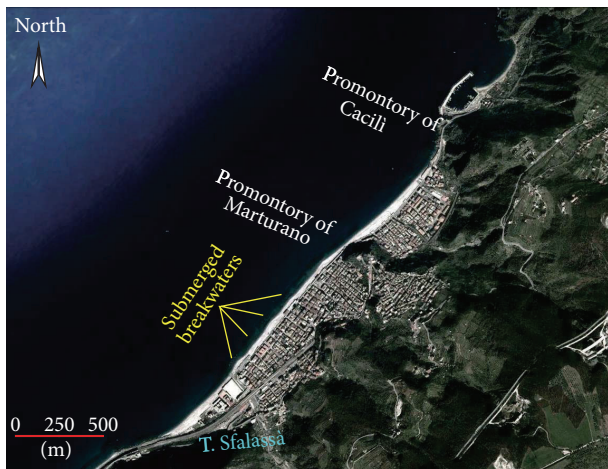


FIGURE 2: Google Earth image of Bagnara Calabria.

introduced by the radar acquisition process [11] and allows us to get the wave spectrum and the sea state parameters, as, for instance, the direction, the period, and the wavelength of the dominant waves, from the 3D spectrum of a raw radar sequence [12]. Based on the knowledge of the dispersion relation for the sea gravity waves, which rules the space-time behavior of a wave motion propagating over a given sea bottom with a prescribed sea surface currents field, it is indeed possible to extract the sea wave signal from the overall noisy data and reconstruct the bathymetry and currents fields [13–15]. However, achieving reliable estimates of the latter quantities from radar data is anything but a straightforward task, above all if the remote survey is carried out in a

TABLE 1: Remocean coastal monitoring system configuration parameters.

Acquisition range	2222.4 m
Rotation time of the antenna	1.97 s
Spatial resolution	5 m
Antenna height (over sea level)	20 m
Angular sector	180°

coastal zone, where a significant inhomogeneity in space can affect the considered parameters. Nevertheless, a number of inversion procedures to be applied on radar data acquired in nearshore areas have been developed in recent years [3, 4, 15, 16]. Among them, the one based on the Normalized Scalar Product (NSP) is the most accurate to get the sea surface current and bathymetry fields from a sequence of marine radar images [14, 17]. In particular, the main steps to deal with the surface current estimation in nearshore areas through the NSP method are summarized in the flow chart of Figure 3, while further details can be found in [3, 16, 18].

The radar used during the Bagnara Calabria survey is a Bridge Master (25 KW antenna with a 2.4 m antenna). Remocean Coastal Monitoring Mobile version measures real-time sea state parameters as wave direction, wavelength, period, significant wave height, sea surface current intensity and direction, and temporal-spatial images of the sea surface elevation. The analyzed data radar consisted of 32 individual images with an interval of 1.97 s between successive images.

Table 1 presents the system configuration parameters.

Radar system was installed on a hotel panoramic rooftop, with view on the sea and on the coast at a height of approximately 20 m from the mean sea level (Figure 4). The radar

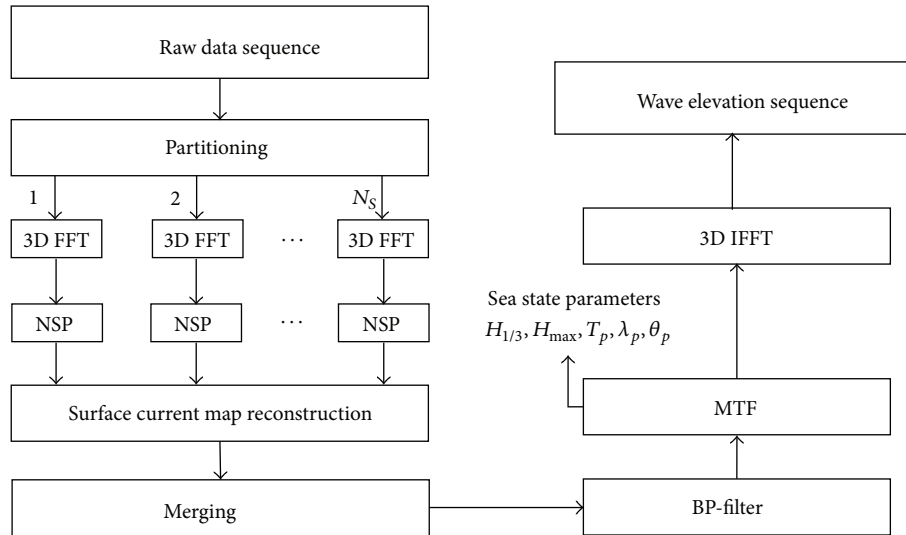


FIGURE 3: Block diagram of the inversion procedure.



FIGURE 4: Particular of Remocean “plug and play” system.

configuration in “mobile data acquisition modality” allows having a great flexibility in the choice of the observation point and is readily installed and operated in mobile modality acquisition.

Regarding the radar functionality, it must specify that, in rough sea conditions, the system can detect dominant wave motions and sea near-surface currents, while, in calm sea conditions, the system allows identifying exclusively the coastline. In fact, intense meteomarine events cause high wave reverberation that hides the shoreline, contrary to what happens in calm sea conditions.

Thanks to the ability to detect the coastline, the radar is a useful tool for comparing subsequent images in time and making both short-term and long-term comparisons and, consequently, to study coast erosion phenomena.

3. Results and Observations

The radar dataset has been collected in the period of 24–27 February 2015. The survey was planned during a period of very rough sea state to be taken as evidence for the near-shore and surf-zone morphological variations on Bagnara Calabria “sedimentary cell” [10]. This approach is normally

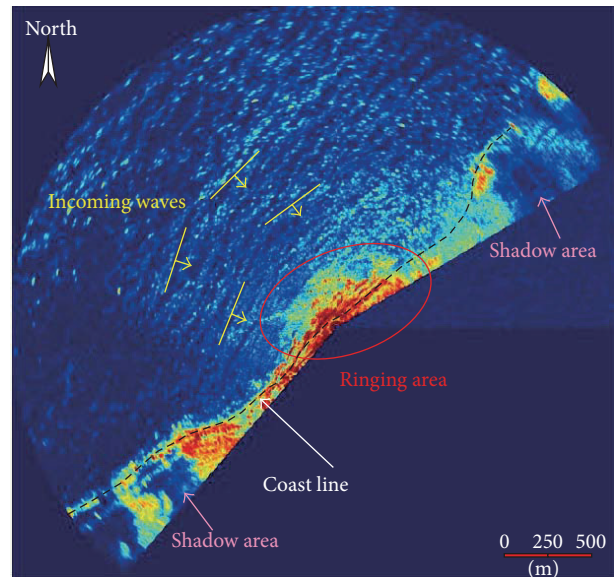


FIGURE 5: Bagnara Calabria instant radar image: the black dashed line underlines the coastline. The along shore bands with very strong signals are related to wave breaking and suggesting the presence of reef-type breakwaters.

used for standout wave propagation, wave run-up, and wave interaction with submerged or emerged structures at stormy conditions.

The radar antenna was located just on centre of cell, on a mobile platform installed at the following coordinates: latitude = $38^{\circ}17'12.80''N$ and longitude = $15^{\circ}48'8.23''E$. Radar data represents an area of $2\text{ km} \times 2\text{ km}$ centered on the test area.

Figure 5 is an example of radar image that provides information about the coastal area. The coastal sector analyzed has a length of about 3 Km.

The radar images interpretation allows us to characterize the test area coastal dynamics. The main wave motion

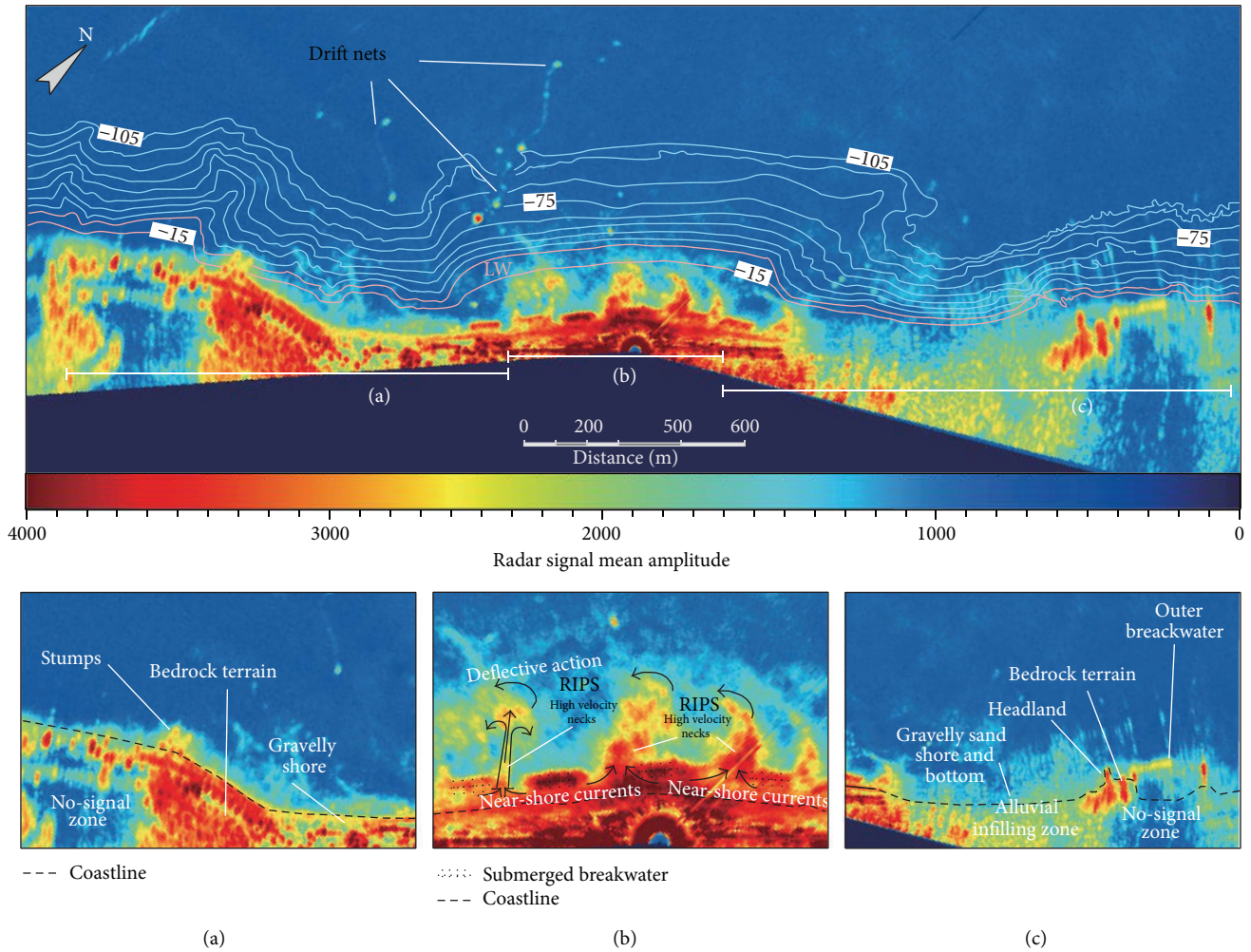


FIGURE 6: Radar image with articulated bathymetry offshore Bagnara Calabria (redrawn from [8]), showing three channels deeply indenting the littoral wedge from -15 to over -200 with headwalls very close to the shore. Coastal area subdivision: (a) southern sector, (b) central sector, and (c) northern sector.

detected by the radar (visible through the clutter in Figure 5) comes from the northwest, according to dominant wave motion listed in previous study performed by Calabria region [10]. The incoming waves approaching the coast with different angles of incidence are produced by their refraction. In fact, if the waves approach the coast obliquely, they will begin to feel the effects of the slowdown in their propagation only in part and the result is a wave fronts rotation that will tend to align the waves parallel to the coast. The red, high-intensity areas in the snapshot image (Figure 5) correspond to regions that are experiencing the greatest wave breaking from the front face of the waves with respect to the radar. Unbalanced wave height distribution around breakwaters induces rip currents and the submerged barriers become a trap for the wave energy content. Consequently, intense waves ringing runs in the stretch between the reef-type breakwaters and the shoreline (Figure 5). In fact, the radar signal reflection is greater in this area than in the others, as well as in all the areas in which there are hard objects as cliffs, buildings, and morphological highs (Figure 5). In general, the radar image shows a different

signal reflection related to the different coastal morphological elements (rocky coast and gravel sandy beach). This area, together with those in which there are “hard” objects (cliffs, buildings, and high grounds), is the one characterized by the greater amplitude of the radar signal.

Figure 6 depicts several morphohydro dynamic characteristics evidenced by the radar system and other important features, as the detection of drifting objects (fishing nets) on the sea surface.

The radar image was compared to the multibeam bathymetry acquired by [8]. This comparison illustrates a close link between the radar images and the bathymetric survey, since the waves, at local scale, are driven by water depth and currents. For example, the increase of the reflected signal intensity (due to the waves breaking) identifies an area characterized by lower depth (< -15 m), which coincides with the external boundary of LW.

Taking into account the different signal amplitude related to the dissimilar coastal morphological elements, we considered three sectors.

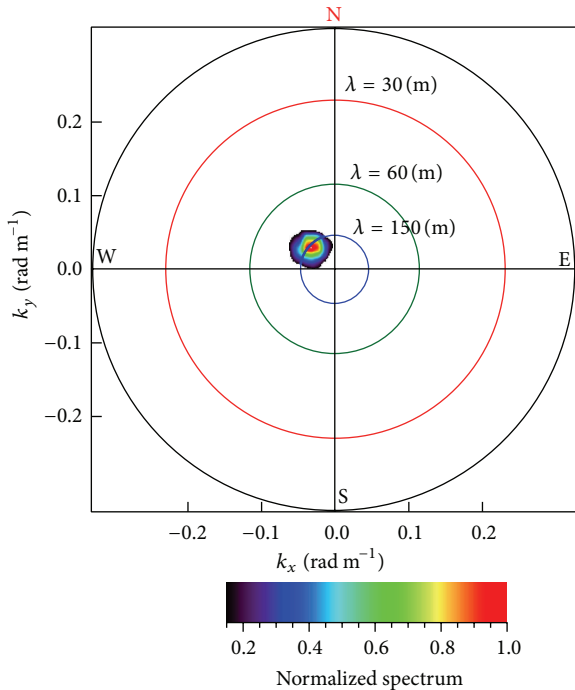


FIGURE 7: Directional spectrum of Bagnara Calabria area.

In the enlargement A, the main signal amplitude is related to the outcrop of the bedrock terrain; conversely “no-signal zone” is due to the shielding of the radar signal by the promontories. The gravelly shore and some stumps are also identified.

In the enlargement B, the image contains a long shore oriented feature of increased backscatter intensity that is connected to incident waves and submerged breakwaters. Consequently, intense rip currents take place (forced currents that move towards sea) at the gaps between the submerged breakwaters. Rip currents appear elongated northwestward with high velocity neck at about 40° with respect to the dominant waves. Moving seaward, the rip currents lose energy gradually and interact with small-scale near-surface current direction, which generate high radar returns as rip heads deflection represented by a plume. Near-shore currents are also well identified between the submerged breakwater and the coastline.

In the enlargement C, the different signal intensity permits discriminating the main principal morphological evidences as the gravelly sand shore, the alluvial infilling from the rocky headland, and the areas with submerged bedrock. There is an additional evidence, of high reflectivity located in proximity of outer breakwater of the harbour area. As the high grounds shield the reflected signal, there is an area with no radar signal.

Figure 7 depicts the directional spectrum obtained by the dataset collected on 25 February 2015 at about 13:00 am (UTC). The directional spectrum has one dominant spectral wave direction from about 300° (northwest).

The resolution of sea near-surface current was evaluated detecting drifting objects (as drift nets) on the sea surface (Figure 8).

Figure 8 illustrates the synchronous combination of sea near-surface current intensity and direction and a black/white radar image retrieved by X-Band Radar. In particular, we analyzed in detail a set of 527 images collected over a period of approximately 17 min starting at 11:14:37 to 11:31:56 for the day 25/02/2015. During this period, the presence of boats that release fishing nets is clearly identifiable; the nets, then, drift mainly towards SW. Subsequently, considering an acquisition time of 1.97 sec, we calculated the displacement of two drift nets. The big one in 1039 seconds shifted 278 m southwest, with a speed of 0.27 m/s; the smaller drift net in 1039 seconds shifted 201 m southwest, with a speed of 0.19 m/s. The map of the sea near-surface current (considering the same period analyzed for the displacement of the drift net) was superimposed on radar image. The sea near-surface current map (Figure 8(b)) shows a current intensity of about 0.3 m/s and about 0.18 m/s in the area of the big and of the small drift nets, respectively. Therefore, the differences between calculated and measured values of current intensity are comparable.

Figure 9 shows temporal variation of intensities rip current occurrence compared with sea conditions. The set of three mean images collected, depicts an example of variation of the rip patterns with identified rip intensities, which indicates that the rip patterns vary rapidly in a short time with the sea conditions. The intensities of rip were estimated by image analyses evaluating long shore pixel brightness distribution.

Radar system provides not only images but also real-time sea state information as the significant wave height (H_s), defined as the mean wave height (trough to crest) of the highest third of the waves ($H_{1/3}$). During the three acquisition days, the system measured H_s values ranging from about 0.5 to 4.5 meters (Figure 10(d)), with the maximum value reached on 25th February. The H_s value estimated by wave radar is a calibrated value. The calibration depends on a number of factors such as acquisition geometry and radar setting. With wave buoy measures not being available, in this case a measure provided by web forecast systems is used. The significant wave height recorded by the Consortium LaMMA (Figures 10(a), 10(b), and 10(c)) is in agreement with the recorded data. The main wave direction detected by LaMMA (Figure 10(a)) is not in agreement with radar measurement (Figure 8(b)): this is probably due to the different scales of measurement.

4. Conclusions

The paper presents the results carried out with the Remocean X-Band Radar system in the Project SIGIEC test site of Bagnara Calabria. From a technology perspective, the main interest lies in the “coastal” configuration of the system. This feature is important since it offers a good flexibility in the choice of the spatial and temporal observation modalities considering also the paucity of data related to hydrodynamics in the nearshore area.

The system, during the acquisition period, provides sea state images useful to characterize the Bagnara Calabria coastal area, such as dominant waves length, period and

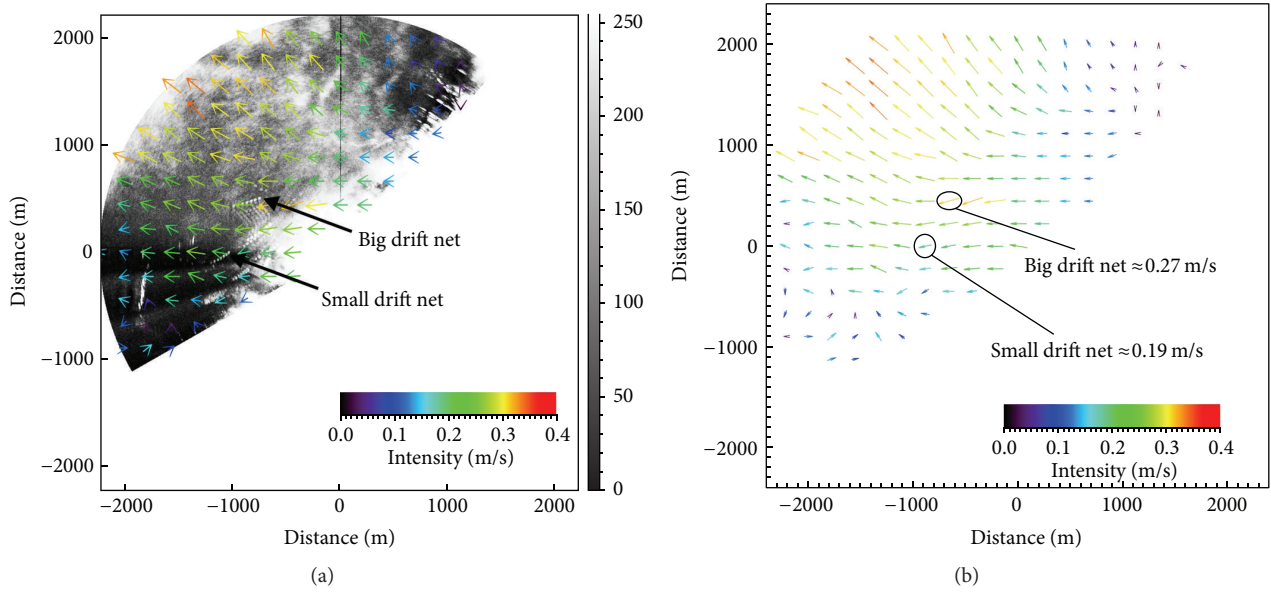


FIGURE 8: (a) Comparison between radar image integrated over time and the corresponding relative sea near-surface current field. (b) Sea near-surface current map: the system best evidences the current vectors oriented in the drifting objects displacement.

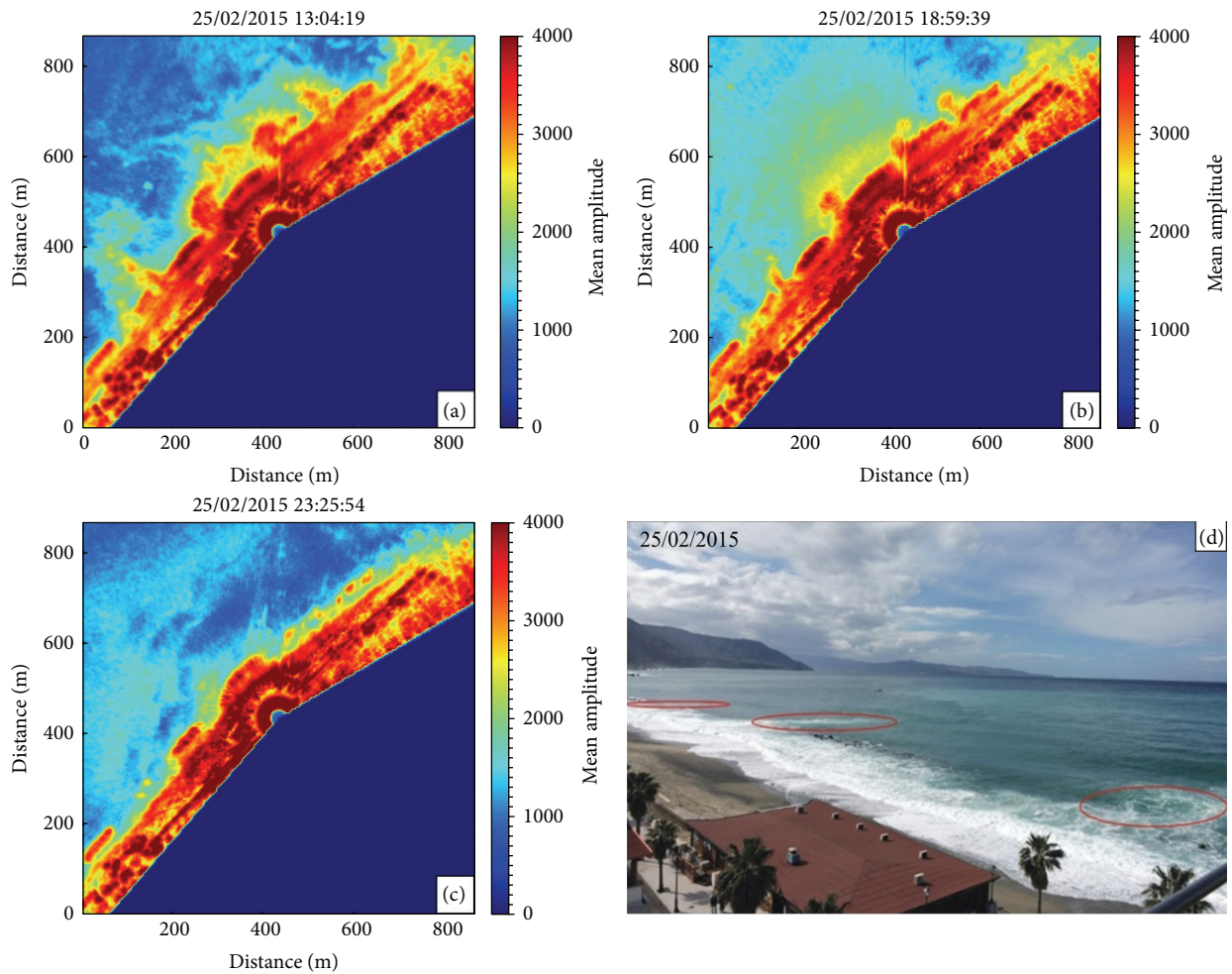


FIGURE 9: Temporal variation of intensities rip current occurrence: (a) very rough sea; (b) moderate sea; (c) smooth sea. (d) The rip currents can be seen in the photograph (red circle), identified by the region without breaking waves and foam transported outside of the surf zone.

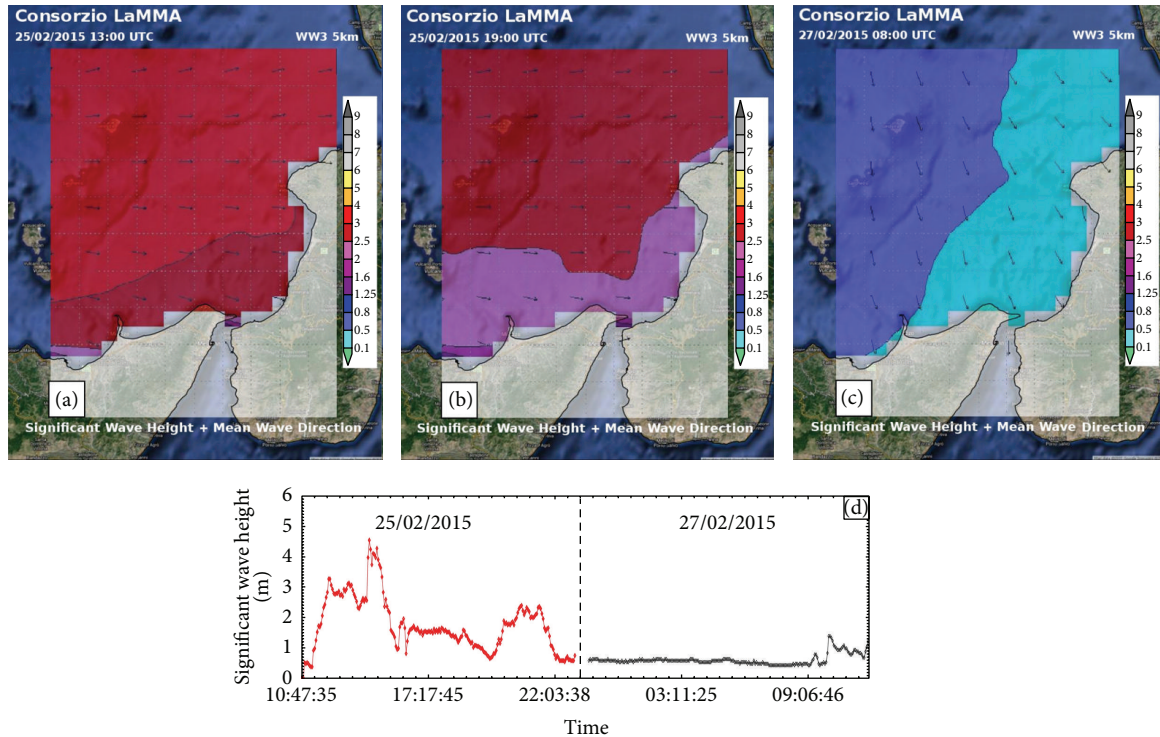


FIGURE 10: (a), (b), and (c) Maps of significant wave height recorded by the Consortium LaMMA in Bagnara Calabria (Data SIO, NOAA, US Navy, NGA, GEBCO ©2015 Google Image Landsat). (d) Significant wave heights measured by X-Band Radar system.

direction, significant wave height, surface current field intensity, and direction.

In particular, the system has allowed determining directional wave spectra, which show a dominant wave direction from the northwest, in agreement with the Master Plan of the Calabria region [10]. The sea surface current field has been validated calculating the speed of drifting objects (drift nets) located near the coast. Significant wave heights, for the acquisition period, are characterized by values ranging from about 0.5 m to 4.5 m.

In the test area, the X-Band Radar has detected anthropic elements as the harbour outer breakwater and the long shore reef-type breakwaters. The system has also permitted determining phenomena of interaction between waves and defense works as intense waves ringing concentration between reef-type breakwaters and coastline. These observations indicate that radar remote sensing can be an effective tool for detecting rip currents and provide a more synoptic picture of the rip current flow field outside the surf zone during high energy events.

Reef-type breakwaters, inducing strong wave breaking above the crown of the same structures, are able to reduce incoming wave energy to the shore. However, in Bagnara case study unbalanced wave height distribution around breakwaters induces intense rip currents and causes scars around the open inlets that affected breakwaters stability. Moreover, shoreline erosion is probably related to breakwaters structural defects.

Designing reef-type breakwaters to reduce the water surface elevation difference between front and rear sides of

the barriers (which determines rip current intensity), it is possible to obtain a reduction of rip currents. For existing reef-type breakwaters, three technologies can be used to limit rip currents: putting gravels on the bottom of the open inlet, installing a small-submerged structure on the onshore side of the open inlet, or installing a drainage channel inside the submerged breakwater to reduce water surface elevation at the rear side of the reef-type breakwater.

The results emphasize the potential of the X-Band Radar for cost-effective monitoring systems in coastal regions. The system, providing real-time wave parameters measures and detecting phenomena due to coastal hydrodynamics, as rip currents, represents a very important tool for coastal areas studies, sea state, and coastal defense works monitoring. It can be very useful especially when it is necessary to estimate coastal erosion phenomena evolution and to project eventual coastal defense works, as in the case of SIGIEC Project.

Conflict of Interests

The authors declare that there is no conflict of interests regarding the publication of this paper.

Acknowledgments

The authors wish to thank Dr. Rodolfo Baculo, IAMC Naples, for technical support during the field data acquisition. Thanks are due to Dr. Francesco Raffa, IAMC-Messina, who provided great supports in the data analysis. Thanks are due to LaMMA

Consortium which provided evolution and swell of the sea. Finally, they want to thank the anonymous reviewers for their useful comments and suggestions. X-Band Radar has been hosted by Grand Hotel Victoria whose hospitality is gratefully acknowledged. The research activity has been financially supported by PON (Operational National Plan) 2007–2013 from MIUR (Italian Research Ministry of Research) Project SIGIEC (Integrated Management System for Coastal Erosion) ID: PON01_02651 (<http://www.sigiec.sister.it/>).

References

- [1] A. Kroon, M. A. Davidson, S. G. J. Aarninkhof et al., “Application of remote sensing video systems to coastline management problems,” *Coastal Engineering*, vol. 54, no. 6-7, pp. 493–505, 2007.
- [2] J. P. Dugan, C. C. Piotrowski, and J. Z. Williams, “Water depth and surface current retrievals from airborne optical measurements of surface gravity wave dispersion,” *Journal of Geophysical Research C: Oceans*, vol. 106, no. 8, pp. 16903–16915, 2001.
- [3] G. Ludeno, F. Reale, F. Dentale et al., “An X-band radar system for bathymetry and wave field analysis in a harbour area,” *Sensors*, vol. 15, no. 1, pp. 1691–1707, 2015.
- [4] K. Hessner, K. Reichert, J. C. N. Borge, C. L. Stevens, and M. J. Smith, “High-resolution X-band radar measurements of currents, bathymetry and sea state in highly inhomogeneous coastal areas,” *Ocean Dynamics*, vol. 64, no. 7, pp. 989–998, 2014.
- [5] L. H. Holthuijsen, *Waves in Oceanic and Coastal Waters*, Cambridge University Press, 2007.
- [6] <http://www.sigiec.sister.it/>.
- [7] G. G. R. Iovine, R. Greco, S. L. Gariano, P. Iaquina, A. Pellegrino, and O. G. Terranova, “Shallow-landslide susceptibility in the Costa Viola Mountain Ridge (Italia),” in *Proceedings of the 2nd World Landslide Forum (WLF '11)*, pp. 81–87, Rome, Italy, October 2011.
- [8] D. Casalbore, A. Bosman, D. Ridente, and F. L. Chiocci, “Coastal and submarine landslides in the tectonically-active tyrrhenian calabrian margin (Southern Italy): examples and geohazard implications,” in *Submarine Mass Movements and Their Consequences*, S. Krastel, J.-H. Behrmann, D. Völker et al., Eds., vol. 37 of *Advances in Natural and Technological Hazards Research*, chapter 23, pp. 261–269, Springer, 2013.
- [9] L. Ferranti, C. Monaco, D. Morelli, F. Antonioli, and L. Maschio, “Holocene activity of the Scilla Fault, Southern Calabria: insights from coastal morphological and structural investigations,” *Tectonophysics*, vol. 453, no. 1–4, pp. 74–93, 2008.
- [10] Autorità di Bacino Regionale and Regione Calabria, *Masterplan degli interventi di mitigazione del rischio di erosione costiera in Calabria—Area 13*, Autorità di Bacino Regionale, Regione Calabria, 2013.
- [11] J. C. N. Borge, G. R. Rodríguez, K. Hessner, and P. I. González, “Inversion of marine radar images for surface wave analysis,” *Journal of Atmospheric and Oceanic Technology*, vol. 21, no. 8, pp. 1291–1300, 2004.
- [12] I. R. Young, W. Rosenthal, and F. Ziemer, “Three-dimensional analysis of marine radar images for the determination of ocean wave directionality and surface currents,” *Journal of Geophysical Research*, vol. 90, no. 1, pp. 1049–1059, 1985.
- [13] P. S. Bell, “Shallow water bathymetry derived from an analysis of X-band marine radar images of waves,” *Coastal Engineering*, vol. 37, no. 3-4, pp. 513–527, 1999.
- [14] F. Serafino, C. Lugni, and F. Soldovieri, “A novel strategy for the surface current determination from marine X-Band radar data,” *IEEE Geoscience and Remote Sensing Letters*, vol. 7, no. 2, pp. 231–235, 2010.
- [15] C. M. Senet, J. Seemann, S. Flampouris, and F. Ziemer, “Determination of bathymetric and current maps by the method DiSC based on the analysis of nautical X-band radar image sequences of the sea surface (November 2007),” *IEEE Transactions on Geoscience and Remote Sensing*, vol. 46, no. 8, pp. 2267–2279, 2008.
- [16] G. Ludeno, C. Brandini, C. Lugni et al., “Remocean system for the detection of the reflected waves from the costa concordia ship wreck,” *IEEE Journal of Selected Topics in Applied Earth Observations and Remote Sensing*, vol. 7, no. 7, pp. 3011–3018, 2014.
- [17] F. Serafino, C. Lugni, J. C. N. Borge, V. Zamparelli, and F. Soldovieri, “Bathymetry determination via X-band radar data: a new strategy and numerical results,” *Sensors*, vol. 10, no. 7, pp. 6522–6534, 2010.
- [18] G. Ludeno, S. Flampouris, C. Lugni, F. Soldovieri, and F. Serafino, “A novel approach based on marine radar data analysis for high-resolution bathymetry map generation,” *IEEE Geoscience and Remote Sensing Letters*, vol. 11, no. 1, pp. 234–238, 2014.

Research Article

LG-Mod: A Modified Local Gradient (LG) Method to Retrieve SAR Sea Surface Wind Directions in Marine Coastal Areas

**Fabio M. Rana,¹ Maria Adamo,¹ Guido Pasquariello,¹
Giacomo De Carolis,² and Sandra Morelli³**

¹*Institute of Intelligent Systems for Automation (ISSIA), National Research Council of Italy (CNR), Via Amendola 122/O, 70126 Bari, Italy*

²*Institute for the Electromagnetic Sensing of the Environment (IREA), National Research Council of Italy (CNR), Via Bassini 15, 20133 Milan, Italy*

³*Department of Physics, Computer Science, and Mathematics, University of Modena and Reggio Emilia, Via Campi 213/a, 41125 Modena, Italy*

Correspondence should be addressed to Fabio M. Rana; rana@ba.issia.cnr.it

Received 29 May 2015; Revised 25 September 2015; Accepted 28 September 2015

Academic Editor: Jose C. Nieto-Borge

Copyright © 2016 Fabio M. Rana et al. This is an open access article distributed under the Creative Commons Attribution License, which permits unrestricted use, distribution, and reproduction in any medium, provided the original work is properly cited.

This paper describes a novel SAR wind direction estimation method based on the computation of local gradients over quasi-linear and quasi-periodic structures detected by SAR imagery. The method relies upon the standard LG method for the part relevant to the computation of the local gradients. The novelty is that the dominant local wind direction and related accuracy are estimated using results derived from the Directional Statistics. The LG-Mod is validated against in situ coastal wind measurements provided by instrumented buoys with 63 ENVISAT ASAR images. Results show an overall agreement with RMSE values obtained for off-shore areas, but residual effects due to the complex phenomena occurring in the proximity of shoreline may degrade the performance when running in automated mode.

1. Introduction

Sea surface wind is a crucial parameter for studies of the several oceanographic applications such as marine meteorology [1, 2], marine oil spill monitoring [3, 4], and wind energy resources [5, 6] among others.

While mesoscale numerical weather models (NWMs) provide reliable wind fields for off-shore areas, in general their accuracy is drastically reduced in the proximity of the shoreline. This is due to the complex land/sea interactions which take place in coastal areas, whose phenomenology is generally poorly described within NWM schemes. In order to overcome such difficulty, accurate observations on regular spatial scale of sea surface winds should feed NWM in order to provide them with useful initial conditions and verification data for reliable coastal wind predictions.

Spaceborne microwave remote sensing of the sea surface has been proved to be effective in monitoring off-shore sea

surface phenomena and has reached technological maturity to provide quantitative coastal areas observations.

Surface winds from scatterometer observations are available and can improve NWM forecasts only off-shore.

While spaceborne scatterometry can provide wind vector measurements on global scale, the coarse spatial resolution (10–25 km) hampers application in coastal regions as a result of the obvious land contaminations.

Besides, synthetic aperture radar (SAR) sensors have demonstrated over the past decade their ability to provide accurate wind speed and direction measurements in the ocean. In contrast to scatterometer, the high spatial resolution of SAR imaging (1–10 m) has the potential to capture the typical complex wind fields which characterize coastal regions. Nevertheless, SAR wind field retrieval in marine coastal areas still remains an open issue.

It has been shown in [7] that SAR wind field retrievals which exploit guess wind information coming from NWMs

[8] show strong dependence on the goodness of the input wind vector used as guess. The information coming from SAR is in general unable to fully correct the input NWM wind direction. For this reason, it would be highly desirable to develop methods which provide wind direction independent of external information.

SAR imaging can detect atmospheric and oceanic phenomena which are able to modulate sea surface and hence the backscattered signal, such as boundary layer rolls (BLRs) and wind streaks (WSs).

BLRs are atmospheric roll vortices generated by thermal instabilities which develop within the marine atmospheric boundary layer [9–11]. They can persist over hours or days and are typically associated with unstable or neutral boundary layer conditions [12, 13]. The fluctuations of wind stress at the convergence and divergence zones between rolls [14, 15] make BLRs appear on SAR images as quasi-periodic linear modulation of backscattering with typical spatial scale ranging from 1 to 4 km. As the orientation of BLR axes is in general between the direction of the mean sea surface wind and that of the associated geostrophic wind [14], such directional signature is being widely used to estimate sea surface wind direction from SAR imaging.

WSs are characterized by a narrower spatial modulation (0.1–0.5 km), as showed for the first time in X-band nautical radar images [16]. These features are more closely aligned with the sea surface wind direction and evolve with a lifetime of several tens of minutes. For this reason, wind streaks have been exploited for wind direction retrieval from SAR images [17, 18].

Although BLRs and WSs can provide wind directions, it is an open issue what are the favourable conditions for their visibility on SAR images and, above all, if their rate of occurrence is enough for operational use. Indeed, as stated in [14], the visibility of BLRs on SAR images depends on several factors, such as the SAR operated frequency and polarization, incidence angle, wind speed regime, and wind direction with respect to SAR look geometry. Moreover, in [19] analysis on a large dataset of SAR images assessed that BLR visibility is subjected to an annual seasonality and that cold air flow conditions foster the formation of atmospheric rolls. However, cooccurrence of such factors does not guarantee the presence of related SAR signatures. In contrast, statistics of occurrence of WSs wait to be compiled and factors influencing their occurrence have to be investigated.

Research on SAR wind fields retrieval has focused on the development of methods which aim at extracting the main orientations of wind-induced features from SAR images. Commonly these algorithms identify the main wind directions with 180° ambiguity, which can be resolved by identifying areas of wind shadowing within the SAR image or by using ancillary wind direction information from NWM predictions or in situ data.

A number of SAR-based wind retrieval algorithms have exploited Fourier analysis [20–23] to provide wind direction from BLRs features with spatial resolution up to 10 km and accuracy ranging approximately from 10° to 40° [23, 24]. Working in the spatial domain, two families of algorithms have been developed, both providing high resolution winds

from BLR and WS signatures: one is based on the use of Wavelet Transforms [19, 25–28] and the second on the computation of local gradients [17]. The former methods rely on the ability of wavelets to detect linear structures on SAR images by performing a multiscale analysis. The LG method has been used for a number of applications such as operational SAR wind retrieval [29], wind resource assessment [6], and extreme events monitoring [30, 31], being part of observing and forecasting systems [32] as well. Therefore, LG method has been validated against in situ observations and NWM outputs to obtain wind direction retrievals with an accuracy of 20–30° [18], thereby showing a good performance on wind speed retrieval in offshore areas.

In this paper a modified version of LG, called LG-Mod [33], is proposed. In contrast to the standard LG method, LG-Mod approach is able to extract the dominant local wind direction directly from the set of the available local directions, thus avoiding time-consuming operations on histogram analysis (i.e., histogram binning, weighting, and smoothing), which are commonly required to perform such analysis. In addition, the presented method provides the accuracy related to each wind direction estimate by exploiting basic results from Directional Statistics [34–36].

The paper is structured as follows: the LG-Mod scheme is described in Section 2 and an example of processing is provided by comparing results from a TerraSAR-X image and wind data obtained by the Eta atmospheric model; then, the LG-Mod method is extensively validated against in situ wind data collected by instrumented buoys over coastal areas by using 63 Envisat SAR images. Finally, the main conclusions are drawn in Section 4.

2. LG-Mod Method

The LG-Mod method consists in the following basic steps.

(i) *Image Smoothing and Subsampling.* According to the LG algorithm [17], SAR image smoothing includes those operations aimed both at mitigating the SAR speckle noise of the input calibrated image and at enhancing the detection of wind-induced patterns (i.e., *wind rows*) on the SAR image. Such smoothing operations should be edge-preserving in order to preserve the directional information of the SAR detected wind structures. The latter is further accomplished by reducing the pixel size to values which are suitable to the best detection of the quasi-periodic, quasi-linear wind-induced features. Typical values range from 100 m to 400 m for the detection of wind rows, thus allowing a multiscale spatial analysis of the SAR signatures.

(ii) *Local Gradients (LGs) Computation.* An optimized derivative Sobel operator is applied on the SAR amplitudes to estimate the directional features through local gradients determination. This step is performed on pixel basis after removing from the SAR resized image all pixels which are deemed unusable, such as land pixels or those affected by unwanted border effects as a result of the processing performed at the previous step [17].

(iii) *Main Directions Extraction.* It represents the novel approach of the LG-Mod with respect to the standard LG method. The resized image of local directions is divided into specific size subimages (hereafter also referred to as ROIs), according to the spatial grid on which the wind direction is requested by the user. For each ROI, the dominant direction inside the ROI is directly retrieved by the whole set of the previously estimated directions. Then, the LG-Mod method provides a measure of accuracy for each estimate by developing basic results from Directional Statistics [34, 35]. In particular, as local direction θ and the opposite direction $\theta \pm \pi$ (radians) are equivalent in a circle, the local angles used for estimations should be intrinsically considered as *axial data* instead of *circular data*. The standard way of handling axial data is to convert them to circular data by “doubling the angles,” that is, transforming θ to 2θ and so ignoring the ambiguity in direction. Thus, given the set of the observed and usable LG directions $\{\beta_i^{\text{ROI}}\}_{i=1}^N$, the mean angle $\langle \beta^{\text{ROI}} \rangle$ and the related accuracy R^{ROI} are, respectively, provided by the following halved phase

$$\begin{aligned} \langle \beta^{\text{ROI}} \rangle & \\ &= \frac{1}{2} \arctan 2 \left(\langle \sin(2\beta_i^{\text{ROI}}) \rangle, \langle \cos(2\beta_i^{\text{ROI}}) \rangle \right) \text{ [rad]} \end{aligned} \quad (1)$$

and by the amplitude of the so-called *Mean Resultant Vector*, as expressed by

$$R^{\text{ROI}} = \sqrt{\langle \cos(2\beta_i^{\text{ROI}}) \rangle^2 + \langle \sin(2\beta_i^{\text{ROI}}) \rangle^2}. \quad (2)$$

The mean resultant length R^{ROI} is a nondimensional parameter which represents a measure of the alignment of the directions inside the ROI.

(iv) *Reliable ROIs Selection and Estimations.* Finally, specifications about the LG-Mod outcomes are fixed directly by the user by adopting a selection criterion to select reliable estimates. Regardless of the statistical distribution of the available directional (axial) data, to each direction estimate, $\langle \beta^{\text{ROI}} \rangle$, an $(1 - \alpha)$ interval of confidence, $\text{ME}_\alpha^{\text{ROI}}$, can be assigned according to the following expression [35, 36]:

$$\text{ME}_\alpha^{\text{ROI}} = \frac{1}{2} \arcsin \left(u_\alpha \sqrt{\frac{(1 - \alpha_2^{\text{ROI}})}{2N_{\text{ROI}} (R^{\text{ROI}})^2}} \right) \text{ [rad]}, \quad (3)$$

where u_α is the upper $(1/2)\alpha$ quantile of the standard normal distribution and $\alpha_2^{\text{ROI}} = \langle \cos(4(\beta_i^{\text{ROI}} - \langle \beta^{\text{ROI}} \rangle)) \rangle$ represents the second central trigonometric moment of the doubled local directions of the ROI. Expression (3) is valid for ROIs with a large size of samples, N_{ROI} .

Therefore, the LG-Mod method is able to discharge noisy ROIs (and related estimates) by setting a suitable threshold value of acceptance ME^{TH} for the estimate $\langle \beta^{\text{ROI}} \rangle$:

$$\text{ROI}_{\text{rel}} = \{ \text{ROI} \mid \text{ME}_\alpha^{\text{ROI}} \leq \text{ME}^{\text{TH}} \}. \quad (4)$$

TABLE 1: Comparison results between Eta model and LG-Mod directions for different thresholding selection ($\alpha = 0.05$ and $\text{ME}^{\text{TH}} = 15^\circ, 10^\circ, \text{ and } 5^\circ$) and for the case of no thresholding.

	RMSE [°]	MBE [°]	Number of wind vectors
No thresholding	26.3	8.2	1616
Thresholding ($\alpha = 0.05; \text{ME}^{\text{TH}} = 15^\circ$)	21.1	6.4	1412
Thresholding ($\alpha = 0.05; \text{ME}^{\text{TH}} = 10^\circ$)	16.5	3.8	1238
Thresholding ($\alpha = 0.05; \text{ME}^{\text{TH}} = 5^\circ$)	7.7	-0.4	578

As an example, the wind field obtained from the X-band TerraSAR-X ScanSAR Multi look Ground range Detected (MGD) image is reported. The SAR image was acquired on February 28, 2010, at 05:44 UTC, with a pixel size equal to 8.5 m, subsequently resampled at $68 \text{ m} \times 68 \text{ m}$. The retrieved wind directions were compared with the ones provided by the Eta numerical weather model [37], which was also used to remove the 180° ambiguity on the wind direction. Eta outputs were provided within a grid of $4 \text{ km} \times 4 \text{ km}$ at 06:00 UTC, that is, with a temporal shift of 15 min with respect to the satellite acquisition time.

In Figure 1(a) the LG-Mod estimates of wind directions (red arrows) are shown over the Eta grids; the Eta model predictions are superimposed (yellow arrows). From a visual inspection, it can be clearly seen that both wind direction fields are in good agreement with each other, with the exception of the areas where (1) wind rows are not visible (e.g., the left and the bottom part of the image; the wind shadowed zones near the coastline) and (2) in the middle upper part of the image which is featured by the propagation of an atmospheric gravity wave. After thresholding selection ($\alpha = 0.05; \text{ME}^{\text{TH}} = 5^\circ$), the wind field shown in Figure 1(b) was obtained.

The SAR retrieved wind directions were assessed by evaluating their root mean square error (RMSE) and mean bias error (MBE), using Eta model as truth reference. Results of this comparison are reported in Table 1 for different threshold values ME^{TH} with confidence level of 95% assigned to the confidence interval of each estimate. The case of no thresholding is also shown in the Table 1 for comparison.

As expected, the tighter the requirements on the assumed accuracy of directional estimates, the lower the estimation error. Accordingly, the number of valid wind estimates progressively reduces. It is worth noting that the accuracy performance of the LG-Mod not only is related to the actual wind conditions but also could depend on SAR system factors, such as the radiometric resolution, which may affect the overall visibility of wind features on the image. This means that a maximum attainable accuracy level has to be expected for a selected SAR sensor. This is the case for ENVISAT SAR imagery for which the highest attainable accuracy was about 15° , as described in the next section.

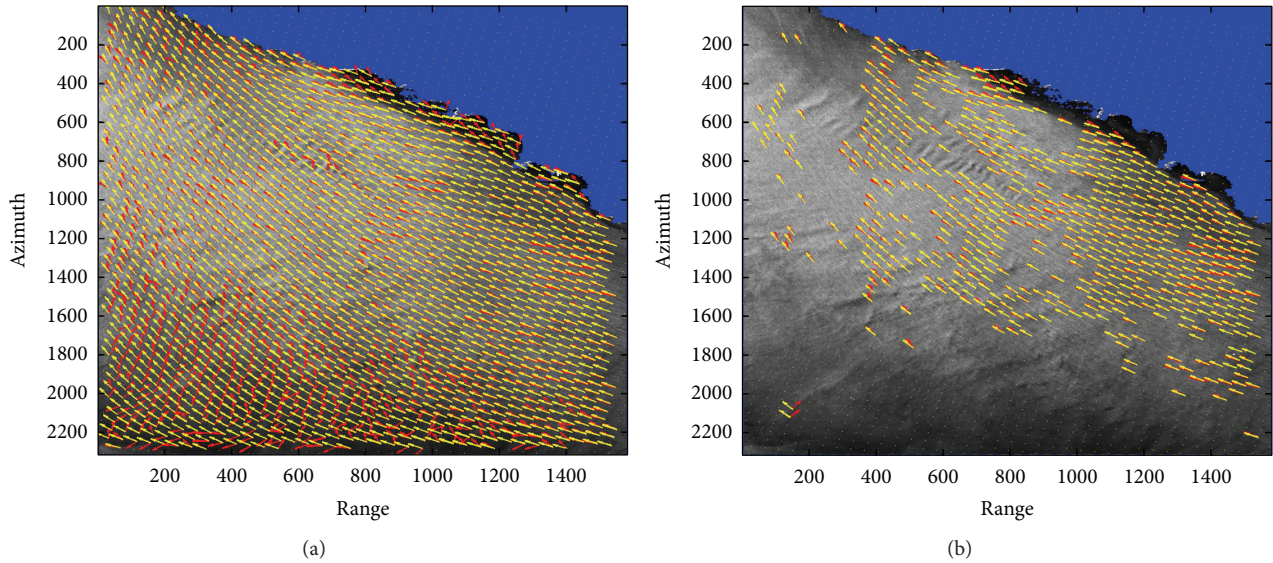


FIGURE 1: Wind directions estimated over a grid of about $4 \text{ km} \times 4 \text{ km}$ by the LG-Mod algorithm (red arrows) and the Eta model (yellow arrows). LG-Mod outcomes are shown before (a) and after (b) discharging unreliable estimations by thresholding selection ($\alpha = 0.05$; $ME^{\text{TH}} = 5^\circ$). The processed full-frame TerraSAR-X ScanSAR MDG image was acquired on February 28, 2010, 05:44:48.110, with VV polarization, descending pass, and off-shore Nice (France), and resized to a pixel size of $68 \text{ m} \times 68 \text{ m}$ (background).

TABLE 2: Information about the buoys deployment and anemometers positioning.

Buoy ID	Geographic coordinates (Lat/Lon) [deg]	Distance from coastline [m]	Sea floor depth [m]	Height of anemometer (above sea level) [m]
62301	52.22 N/4.42 W	≈ 2600	≈ 13	3.0
62303	51.60 N/5.10 W	≈ 3400	≈ 24	3.0

3. Results

In order to evaluate how the LG-Mod performances in coastal regions, a validation analysis was carried out on a dataset of ENVISAT ASAR images acquired at C-band during the period from 2009 to 2012 in correspondence of two marine coastal areas off-shore Wales (UK). The data have been downloaded from the European Space Agency rolling archives. The two stations were instrumented with buoys belonging to the National Data Buoy Center (NDBC) to hourly collect physical parameters of the marine and atmospheric environment (i.e., wind speed and direction, water and air temperature, air pressure, etc.). In Table 2 relevant information about the buoys deployment and anemometers positioning is reported.

The LG-Mod estimation of the wind directions was carried out on a dataset composed of 63 descending and ascending pass ENVISAT ASAR images, 23 and 40 images in correspondence of 62301 and 62303 buoys, respectively. SAR images were Wide Swath Mode products, with pixel size of $75 \text{ m} \times 75 \text{ m}$. All the SAR products were in the Precision Image (PRI) format and VV polarization. All the available images were radiometrically calibrated with NEST (Next ESA SAR Toolbox) package provided by the ESA (European Space Agency) and preprocessed to get a pixel size of about $150 \text{ m} \times 150 \text{ m}$.

The SAR wind was estimated over squared patch of the SAR image with sizes of 3.6 km , centered on the pixel corresponding to buoy location.

Wind speeds measured by anemometers were collected every hour at the height of 3 m above the sea level (a.s.l.) for both sites. Thus, in order to compare these measurements with the corresponding SAR wind vectors, the instrumental wind speeds were referred to at the height of 10 m a.s.l. [38].

In order to correctly compare each anemometer measurement with the corresponding SAR-based estimation, buoy wind data were linearly interpolated to the SAR acquisition times.

After applying the procedure described in the previous sections, 180° ambiguous wind directions are retrieved for each patch. To resolve the ambiguity in the wind direction, the buoy wind data, interpolated to the time of SAR, were used. For each patch, the retrieved ambiguous direction is compared against the buoys direction, and the one with smaller angular difference is selected. After 180° ambiguity removal, the retrieved wind directions, along with the average SAR Normalized Radar Cross Section (NRCS) value and the mean incidence angle, were computed to estimate the corresponding wind speed using the Geophysical Model Function (GMF) CMOD5.N [39].

TABLE 3: Statistical results for different subsets.

Dataset	Wind direction RMSE [°]	Wind direction MBE [°]	Wind speed RMSE [m/s]	Wind speed MBE [m/s]	Number of images
A	44.11	-10.32	2.99	-0.77	63
B	19.40	-11.05	2.78	-2.17	6
C ($\alpha = 0.05$; $ME^{TH} = 15^\circ$)	26.08	-10.45	2.81	-1.89	10

TABLE 4: The buoy mean wind speed and air/sea difference temperature.

Dataset	Buoy mean wind speed [m/s]	Buoy mean $(T_{air} - T_{sea})$ [°]
A	10.6 ± 3.5	-1.1 ± 2.1
B	15.5 ± 2.2	-0.7 ± 0.9
C ($\alpha = 0.05$; $ME^{TH} = 15^\circ$)	11.4 ± 4.3	-0.9 ± 0.9

The analysis has been conducted considering the whole dataset (A) of the available SAR images, a first subset (B) composed by those images selected after a visual inspection and detection of wind rows around the buoys location and a second subset (C) collecting those “reliable” images automatically selected by the application of the final thresholding step (according to (4), with $\alpha = 0.05$; $ME^{TH} = 15^\circ$). In Table 3, statistical results, that is, root mean square error (RMSE) and mean bias error (MBE), derived from the cross-comparison between LG-Mod outcomes and in situ data, are reported, for each defined set of images. Obviously, RMSE and MBE definitions with reference to wind directions take into account that directions must be considered as axial data. From Table 3 it results in high wind direction RMSE if the whole data set is considered. Wind direction RMSE reduces to about 20° when considering SAR images with distinct linear signatures (subset B). These SAR images are characterized by high speed wind regime (>10 m/s, see Table 4) which causes strong local gradients. In the case of automatic selection (described in Section 2), the value of RMSE of about 26° is consistent with the previous selection (subset C). Finally, the good performance of LG-Mod in recognizing wind features when compared to the human expert capability should be pointed out. Indeed, the number of SAR images composing subset C is consistent with relaxing on the user accuracy requirement (i.e., $ME^{TH} = 15^\circ$).

4. Conclusions

A novel SAR wind direction retrieval scheme, called LG-Mod, is described. It is based on the directional information carried by the local gradients (LGs) directly computed on quasi-linear, quasi-periodic wind induced structures detected on SAR images. These structures can be related either to atmospheric boundary layer phenomena or streaks generated by the action of the wind on the sea surface. The performance of the method was evaluated using 63 SAR images of coastal sites. The detected linear features

were compared against in situ measurements of the wind direction provided by instrumented buoys. Considering the limited number of SAR images used in this study, the results presented should be considered as preliminary. Bearing the latter in mind, the following conclusions can be drawn:

- (1) The RMSE value of wind direction estimated on SAR images selected after visual detection of wind rows was comparable with literature reports on off-shore case studies. This result is much better than the best performances obtained using inversion scheme based on wind direction provided by NWM [7].
- (2) Adoption of a threshold value on ME^{TH} led to selection of SAR images with meaningful wind induced features (subset C). This result is encouraging as a criterion for automated SAR image selection can be envisaged. It is worth to analyze the composition of SAR images belonging to subset C: 50% of them include wind rows which escaped from visual inspection; 10% are in common with subset B; and the remaining 40% of SAR images include strong linear features not related to the wind field. The latter result is not unexpected as a consequence of the complex phenomena occurring in coastal areas.
- (3) It should be expected that a significant number of SAR images belonging to subset B were in common with subset C. Instead, only one SAR image belonging to subset B entered in subset C. It frequently happened that the alignment of detected streaks on SAR images showed an angular dispersion much more prominent than that observed in open sea. This could be explained as the effect of small scale coastal circulation. Although most wind cells were dominated by high directional noise, it was still possible to recognize a dominant direction characterized by strong gradient.

Conflict of Interests

The authors declare that there is no conflict of interests regarding the publication of this paper.

Acknowledgment

The activities described in this paper have been funded by the Italian Flagship Project RITMARE.

References

- [1] K. S. Friedman, T. D. Sikora, W. G. Pichel, P. Clemente-Colón, and G. Hufford, "Using spaceborne synthetic aperture radar to improve marine surface analyses," *Weather and Forecasting*, vol. 16, no. 2, pp. 270–276, 2001.
- [2] D. B. Chelton, M. H. Freilich, J. M. Sienkiewicz, and J. M. Von Ahn, "On the use of QuikSCAT scatterometer measurements of surface winds for marine weather prediction," *Monthly Weather Review*, vol. 134, no. 8, pp. 2055–2071, 2006.
- [3] H. A. Espedal and T. Wahl, "Satellite SAR oil spill detection using wind history information," *International Journal of Remote Sensing*, vol. 20, no. 1, pp. 49–65, 1999.
- [4] G. De Carolis, M. Adamo, G. Pasquariello, D. De Padova, and M. Mossa, "Quantitative characterization of marine oil slick by satellite near-infrared imagery and oil drift modelling: the Fun Shai Hai case study," *International Journal of Remote Sensing*, vol. 34, no. 5, pp. 1838–1854, 2013.
- [5] C. B. Hasager, M. Badger, A. Peña, X. G. Larsén, and F. Bingöl, "SAR-based wind resource statistics in the Baltic Sea," *Remote Sensing*, vol. 3, no. 1, pp. 117–144, 2011.
- [6] M. B. Christiansen, W. Koch, J. Horstmann, C. B. Hasager, and M. Nielsen, "Wind resource assessment from C-band SAR," *Remote Sensing of Environment*, vol. 105, no. 1, pp. 68–81, 2006.
- [7] M. Adamo, F. M. Rana, G. De Carolis, and G. Pasquariello, "Assessing the Bayesian inversion technique of C-band synthetic aperture radar data for the retrieval of wind fields in marine coastal areas," *Journal of Applied Remote Sensing*, vol. 8, no. 1, Article ID 083531, 2014.
- [8] M. Portabella, A. Stoffelen, and J. A. Johannessen, "Toward an optimal inversion method for synthetic aperture radar wind retrieval," *Journal of Geophysical Research C: Oceans*, vol. 107, no. 8, pp. 1–13, 2002.
- [9] T. M. Weckwerth, J. W. Wilson, R. M. Wakimoto, and N. A. Crook, "Horizontal convective rolls: determining the environmental conditions supporting their existence and characteristics," *Monthly Weather Review*, vol. 125, no. 4, pp. 505–526, 1997.
- [10] S. Khanna and J. G. Brasseur, "Three-dimensional buoyancy-and shear-induced local structure of the atmospheric boundary layer," *Journal of the Atmospheric Sciences*, vol. 55, no. 5, pp. 710–743, 1998.
- [11] T. M. Weckwerth, T. W. Horst, and J. W. Wilson, "An observational study of the evolution of horizontal convective rolls," *Monthly Weather Review*, vol. 127, no. 9, pp. 2160–2179, 1999.
- [12] P. Drobinski and R. C. Foster, "On the origin of near-surface streaks in the neutrally-stratified planetary boundary layer," *Boundary-Layer Meteorology*, vol. 108, no. 2, pp. 247–256, 2003.
- [13] D. Etling and R. A. Brown, "Roll vortices in the planetary boundary layer: a review," *Boundary-Layer Meteorology*, vol. 65, no. 3, pp. 215–248, 1993.
- [14] W. Alpers and B. Brummer, "Atmospheric boundary layer rolls observed by the synthetic aperture radar aboard the ERS-1 satellite," *Journal of Geophysical Research*, vol. 99, no. 6, pp. 12613–12621, 1994.
- [15] T. W. Gerling, "Structure of the surface wind field from the Seasat SAR," *Journal of Geophysical Research*, vol. 91, no. 2, pp. 2308–2320, 1986.
- [16] H. Dankert, J. Horstmann, and W. Rosenthal, "Ocean wind fields retrieved from radar-image sequences," *Journal of Geophysical Research C: Oceans*, vol. 108, no. 11, pp. 3352–3364, 2003.
- [17] W. Koch, "Directional analysis of SAR images aiming at wind direction," *IEEE Transactions on Geoscience and Remote Sensing*, vol. 42, no. 4, pp. 702–710, 2004.
- [18] W. Koch and F. Feser, "Relationship between SAR-derived wind vectors and wind at 10-m height represented by a mesoscale model," *Monthly Weather Review*, vol. 134, no. 5, pp. 1505–1517, 2006.
- [19] G. Levy, "Boundary layer roll statistics from SAR," *Geophysical Research Letters*, vol. 28, no. 10, pp. 1993–1995, 2001.
- [20] F. Fetterer, D. Gineris, and C. C. Wackerman, "Validating a scatterometer wind algorithm for ERS-1 SAR," *IEEE Transactions on Geoscience and Remote Sensing*, vol. 36, no. 2, pp. 479–492, 1998.
- [21] S. Lehner, J. Horstmann, W. Koch, and W. Rosenthal, "Mesoscale wind measurements using recalibrated ERS SAR images," *Journal of Geophysical Research C: Oceans*, vol. 103, no. 4, pp. 7847–7856, 1998.
- [22] C. C. Wackerman, C. L. Rufenach, R. A. Shuchman, J. A. Johannessen, and K. L. Davidson, "Wind vector retrieval using ERS-1 synthetic aperture radar imagery," *IEEE Transactions on Geoscience and Remote Sensing*, vol. 34, no. 6, pp. 1343–1352, 1996.
- [23] C. C. Wackerman, W. G. Pichel, and P. Clemente-Colon, "Automated estimation of wind vectors from SAR," in *Proceedings of the 12th Conference on Interactions of the Sea and Atmosphere*, Long Beach, Calif, USA, February 2003.
- [24] H. Lin, Q. Xu, and Q. Zheng, "An overview on SAR measurements of sea surface wind," *Progress in Natural Science*, vol. 18, no. 8, pp. 913–919, 2008.
- [25] Y. Du, P. W. Vachon, and J. Wolfe, "Wind direction estimation from SAR images of the ocean using wavelet analysis," *Canadian Journal of Remote Sensing*, vol. 28, no. 3, pp. 498–509, 2002.
- [26] N. Fichaux and T. Ranchin, "Combined extraction of high spatial resolution wind speed and wind direction from SAR images: a new approach using wavelet transform," *Canadian Journal of Remote Sensing*, vol. 28, no. 3, pp. 510–516, 2002.
- [27] G. C. Leite, D. M. Ushizima, F. N. S. Medeiros, and G. G. de Lima, "Wavelet analysis for wind fields estimation," *Sensors*, vol. 10, no. 6, pp. 5994–6016, 2010.
- [28] S. Zecchetto and F. De Biasio, "A wavelet-based technique for sea wind extraction from SAR images," *IEEE Transactions on Geoscience and Remote Sensing*, vol. 46, no. 10, pp. 2983–2989, 2008.
- [29] J. Horstmann and W. Koch, "Evaluation of an operational SAR wind field retrieval algorithm for ENVISAT ASAR," in *Proceedings of the IEEE International Geoscience and Remote Sensing Symposium*, pp. 44–47, ACM, Anchorage, Alaska, USA, September 2004.
- [30] E. V. Stanev, J. Schulz-Stellenfleth, J. Staneva, S. Grayek, J. Seemann, and W. Petersen, "Coastal observing and forecasting system for the German bight—estimates of hydrophysical states," *Ocean Science*, vol. 7, no. 5, pp. 569–583, 2011.
- [31] R. P. Signell, J. Chiggiato, J. Horstmann, J. D. Doyle, J. Pullen, and F. Askari, "High-resolution mapping of Bora winds in the northern Adriatic Sea using synthetic aperture radar," *Journal of Geophysical Research: Oceans*, vol. 115, no. 4, 2010.
- [32] J. Horstmann, W. Koch, D. R. Thompson, and H. Graber, "Observation of hurricane winds using synthetic aperture radar," in *Proceedings of the Advances in SAR Oceanography from ENVISAT and ERS Missions (SeaSAR '06)*, ESA SP-613, Frascati, Italy, January 2006.

- [33] F. M. Rana, M. Adamo, G. Pasquariello, G. De Carolis, S. Morelli, and F. Bovenga, "A simplified local gradient method for the retrieval of SARderived sea surface wind directions," in *Proceedings of the 10th European Conference on Synthetic Aperture Radar (EUSAR '14)*, Berlin, Germany, June 2014.
- [34] K. V. Mardia and P. E. Jupp, *Directional Statistics*, vol. 494, John Wiley & Sons, New York, NY, USA, 1999.
- [35] N. I. Fisher, *Statistical Analysis of Circular Data*, Cambridge University Press, Cambridge, UK, 1995.
- [36] N. I. Fisher and T. Lewis, "Estimating the common mean direction of several circular or spherical distributions with differing dispersions," *Biometrika*, vol. 70, no. 2, pp. 333–341, 1983.
- [37] F. Mesinger, S. C. Chou, J. L. Gomes et al., "An upgraded version of the Eta model," *Meteorology and Atmospheric Physics*, vol. 116, no. 3-4, pp. 63–79, 2012.
- [38] H. K. Johnson, "Simple expressions for correcting wind speed data for elevation," *Coastal Engineering*, vol. 36, no. 3, pp. 263–269, 1999.
- [39] H. Hersbach, *CMOD5. N: A C-Band Geophysical Model Function for Equivalent Neutral Wind*, European Centre for Medium-Range Weather Forecasts, 2008.

Research Article

Visibility of River Plume Fronts with an X-Band Radar

Satoshi Takewaka

Division of Engineering Mechanics and Energy, University of Tsukuba, Tsukuba 305-8573, Japan

Correspondence should be addressed to Satoshi Takewaka; takewaka@kz.tsukuba.ac.jp

Received 27 July 2015; Accepted 6 September 2015

Academic Editor: Francesco Serafino

Copyright © 2016 Satoshi Takewaka. This is an open access article distributed under the Creative Commons Attribution License, which permits unrestricted use, distribution, and reproduction in any medium, provided the original work is properly cited.

A land-based X-band radar was employed to observe river plume fronts at the mouth of the Tenryu River, Japan. Time-averaged radar images captured fronts extending offshore from the river's mouth as bright streaks. Comparisons between satellite optical images and radar images confirm that streaky features in the radar image represent color river plume fronts. Further corroboration comes from field observations of water temperature, salinity, and turbidity conducted simultaneously with the radar measurements. When a survey ship crossed the front, the measured properties varied discontinuously, suggesting that water from the river and sea converged there and also that a downwards current was present. Variation of visibility of the fronts was assessed and compared with the rate of variation of water level and the wind speed and direction. The radar is able to image fronts when the water level is decreasing during ebb tide and the wind speed is over 3 m/s along shore. Surface ripple waves are generated by the local wind, and if they propagate across the front, wave heights increase, causing higher backscatter of the emitted radar beam. This observation gives further evidence on the imaging mechanism of river plume fronts with X-band radars in relation to wind direction.

1. Introduction

River and sea water meet at a river's mouth when the tide is ebbing and form a river plume front observable as discontinuities in surface color, surface roughness of the sea, water temperature, salinity, turbidity, and other physical properties. Observations of river plume fronts have been conducted to characterize the fluid-dynamical aspects and the biological and chemical processes involved in the interaction between land water and oceanic water. Mixing processes of fresh and salt water at the river mouth affect the sedimentation, mixing of suspended solids, and so forth, and those consequences are important from engineering aspects.

Kilcher and Nash [1] gave a comprehensive review on "tidal plume fronts" (in their terminology) which are formed by ebb discharge from a river's mouth. Visual observations [2], instrumental observations [1, 3, 4], marine radar observations at grazing angle (e.g., [1, 5, 6]), and radar observations from space (e.g., [7, 8]) are the major means of detecting and following river plume fronts with the main purposes of elucidating the spatial and temporal behavior of the fronts, mixing processes, flow structures of river and sea water, and propagation dynamics.

Garvine and Monk [2] made field observations of vertical distributions of current velocity, water temperature, and salinity at the mouth of the Connecticut River, USA. They identified vigorous flow convergence with a sinking motion and change in water surface color at the front. Luketina and Imberger [3] made field observations with multiple instruments at the face of a channel connecting an estuary and Koombana Bay in Australia and described strong convergence and concentrated circulation at the front. In their field measurements, the locations of the fronts were determined by tracing foam lines on the water surface. Marmorino and Trump [4] report results of measurements of the outflow of the Chesapeake Bay in the US into the Atlantic Ocean. Frontal structures on a larger scale compared to the studies noted above were observed, and the existence of similar flow patterns at the front was confirmed. It is widely accepted that there is a flow convergence and vertical circulation at the front, where river and sea water meet, and this will be corroborated by this study also.

Wolff et al. [6] used an X-band imaging radar mounted on the island of Sylt in Germany to observe coastal waves, morphological changes, tide stream patterns, and other features. They averaged the radar images in time to extract

static signatures and to discuss the flow patterns of tidal cycles. In their work, the time-averaged radar images have caught frontal structures, which is not pointed out explicitly. Pritchard and Huntley [5] analyzed the formation and evolution of a tidally modulated river plume based on X-band radar observations at the mouth of a small river in the English Channel. An outflow of a semicircular river plume was captured in the radar images, and the rate of radial spreading was estimated from the sequence of images. Kilcher and Nash [1] performed “front-tracking” experiments of currents offshore of the Columbia River, which flows into the Pacific Ocean in the US using acoustic Doppler profiler. Surface backscatter from an X-band radar mounted on a survey ship was used to trace the position, shape, and orientation of the front during the measurements. The authors regarded the bands of higher radar backscatter as regions where surface flow converged.

Satellite radar observations are also capable of detecting river front plumes. Images of synthetic aperture radar (SAR) have been analyzed to understand the behavior of outflows of large rivers. Hessner et al. [7] analyzed the behavior of river plume fronts observed along the Rhine River outflow into the North Sea by European radar satellites ERS-1 and ERS-2. They assert that the formation and the locations of the frontal features are mainly linked to the semidiurnal tidal phase in the outflow region. Jay et al. [8] studied the interaction of Columbia River plumes with the California Current and used radar images captured by RADARSAT-1 to understand their synoptic behavior.

Most of these studies using radar images are predicated on temporal field observations being meaningfully correlated to the behavior of river plume fronts; however, they are snapshots of tidal cycles, and so, for example, the variation in the visibility, or definition, of the fronts in the radar images and its dependence on environmental conditions are not well understood. Alpers [9] discusses the imaging of oceanic internal waves and ocean bathymetry with satellite radars. If an internal wave exists, horizontal flows are induced along the sea surface, resulting in local amplification of surface waves and higher backscatter due to enhanced Bragg scattering of radar beams. Alpers et al. [10] further describe the imaging of underwater topographies from space when surface waves are locally amplified by accelerated or decelerated tidal flows above uneven bottoms. They give optimal wind conditions for observing these features in radar images: (1) wind-generated small-scale surface roughness with a wavelength of a few centimeters for the backscatter of microwaves and (2) optimum wind speeds for detecting these features that are from 3 to 6 m/s. Dependence of backscatter on the wind, surface current, and surface waves is discussed for a theoretical model of a vertical cross section of the ocean by Romeiser and Alpers [11]. The amount of backscatter is estimated for surface waves propagating upwind and downwind.

The author has employed a land-based X-band radar to observe the behavior of river plume fronts continuously during tidal cycles over many years. The radar is installed on the roof of a building close to the mouth of the Tenryu River, in Japan. The hourly processed radar images show streaky features extending offshore from the river’s mouth,

similar to river plume fronts. The origin of this feature is examined in the light of satellite images, simultaneous field observations, and radar measurements. The definition of the river plume fronts captured in the radar images was assessed by visual inspection, and its dependence on the variation of the water level and local wind is discussed. Higher definition is frequently observed when the water level is falling and the alongshore component of the local wind speed exceeds 3 m/s. This observation leads to a discussion of the imaging mechanism of river plume fronts with the radar, especially the dependence on the local wind direction and the extent of the river plume front.

2. Study Site and the Radar Observations

The Tenryu River flows to the Enshu Coast (lat/long: N-34.6472/E-137.7933), Japan, as shown in Figure 1(a). The coast, facing the Pacific Ocean, suffers from severe erosion, and, consequently, enhancement of sediment supply from the catchment is being planned to mitigate the erosion. The river basin area is 5,090 km², and the length of the river is 213 km. Observation by a land-based X-band imaging radar, in this context, helps us understand the morphology and hydrodynamics by capturing spatial distributions and temporal variation of water lines of the river channel and coastlines and wave propagation in the shallow area [12].

The radar employed in this study is a conventional commercial marine X-band radar (JMA-3925-9 Japan Radio Co. Ltd., incoherent radar, 3 cm wavelength, 25 kw transmitting power, HH-polarization, and 0.08 μ s radar pulse length), which is usually installed on fishery or commercial boats. The 2.8 m antenna rotates with a period of approximately 2.6 s and transmits with a beam width of 0.8° in the horizontal plane and 25° in the vertical plane, respectively. The radar is installed on the roof of a sewage plant located near the mouth of the river, as depicted in the satellite image in Figure 1(b). The measurements started in June of 2007 and are still ongoing as of 2013. All the dates and times are displayed in Japanese Standard Time (JST) in the following.

Backscatter, or echo signals, from the sea surface, so-called sea clutter, are sampled at 20 MHz with a specially designed A/D-board installed on a Windows PC. The signals are then converted to a rectangular image of 1024 pixels in both the Cartesian coordinates. Each pixel corresponds to a square of 5.43 m, which is smaller than the theoretical spatial resolution 7.5 m of the radar system as determined from the pulse length of the emitted beam [13]. There are two main scattering mechanisms for backscatter from the sea surface [14]. The first is Bragg scattering from gravity-capillary waves when the length of the roughness is half the wavelength of the radar beam, which is 1.5 cm in this study. The second is backscatter that comes from steep and breaking waves, especially in shallow waters. For a horizontally polarized radar beam, that is, for HH-polarization, the latter is stronger than the Bragg scattering.

Time-averaged radar images over 17 min. are processed hourly, as shown in Figure 1(c), which enables identification of water lines of the river channel, dune locations, shore

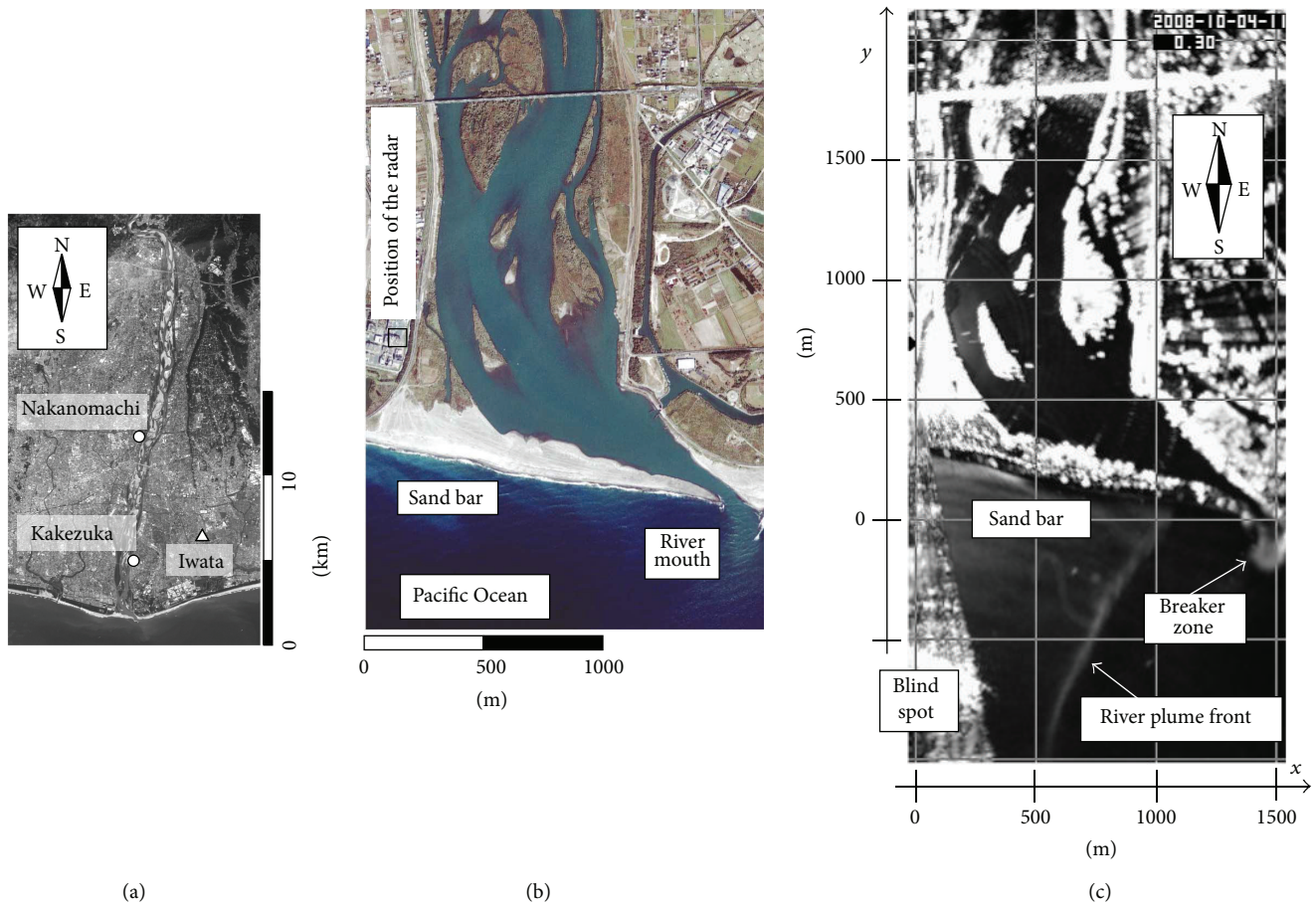


FIGURE 1: Location of the site: (a) River Tenryu and its fluvial plain, ○: gauging station (Nakanomachi, Kakezuka). △: weather station (Iwata). (b) Satellite optical image of the study area, the river's mouth, (Ikonos-2 satellite, acquisition time: 4 October, 2008, 10:54). (c) Time-averaged radar image (average of instantaneous images collected during 11:00 to 11:17 of 4 October, 2008). A river plume front is extending from the sand bar. Breaker zone is formed at the shoal of the river mouth.

positions, breaker zones, and other features. The gray images have pixel intensities between 0 and 255, with brighter pixels corresponding to points with higher signal returns. Comparison with optical satellite data indicates the highest echo signals, depicted with a bright intensity, come from solid surfaces, such as dunes and floodplains, and shallow waters with rough surface due to wave breaking. Smooth sea surfaces return only a small amount of the emitted beam, so they are dark in the time-averaged radar images. A fan-like spot lies on the left side of the averaged radar image, where the radar beam is interfered with by a tower on the sewage plant. The figure also shows the coordinate system used in the study—the x -coordinate for east-west extent and the y -coordinate for north-south.

In Figure 1(c), a streak denoted as “River front plume” extending offshore from the designated sand bar may represent a front where fresh and salt water encounter. This feature is not always detectable, and the origin of the pattern in the radar image will be discussed in this report. Figure 2 contains an example of a sequence of radar images time-averaged over 8 hours with and without a streaky pattern. The streaky pattern extends offshore from the vicinity of the river's mouth

with different inclinations depending on the tidal phase. The bracketed digits encode the definition, or the intensity of the front, as assessed by inspection. Details of these features and the assessment are discussed later on.

3. Color Fronts Captured in Satellite Images and Streaky Patterns Captured in the Radar Images

River plume fronts are observed in the field as sharp changes in the sea surface color, or as a color front [2]. The water from the river contains a higher concentration of suspended solids than the sea water. The sea surface also frequently shows an abrupt change from a smooth one to a rough one across the front: vertical circulation is formed at the front and resultant velocity gradient at the surface alters the amplitudes of surface ripples [3, 4]. Here, satellite images and time-averaged radar images are compared to understand the origin of the streaky pattern.

Figure 3(a) shows a comparison between an optical image acquired by ALOS satellite on July 24, 2008, and

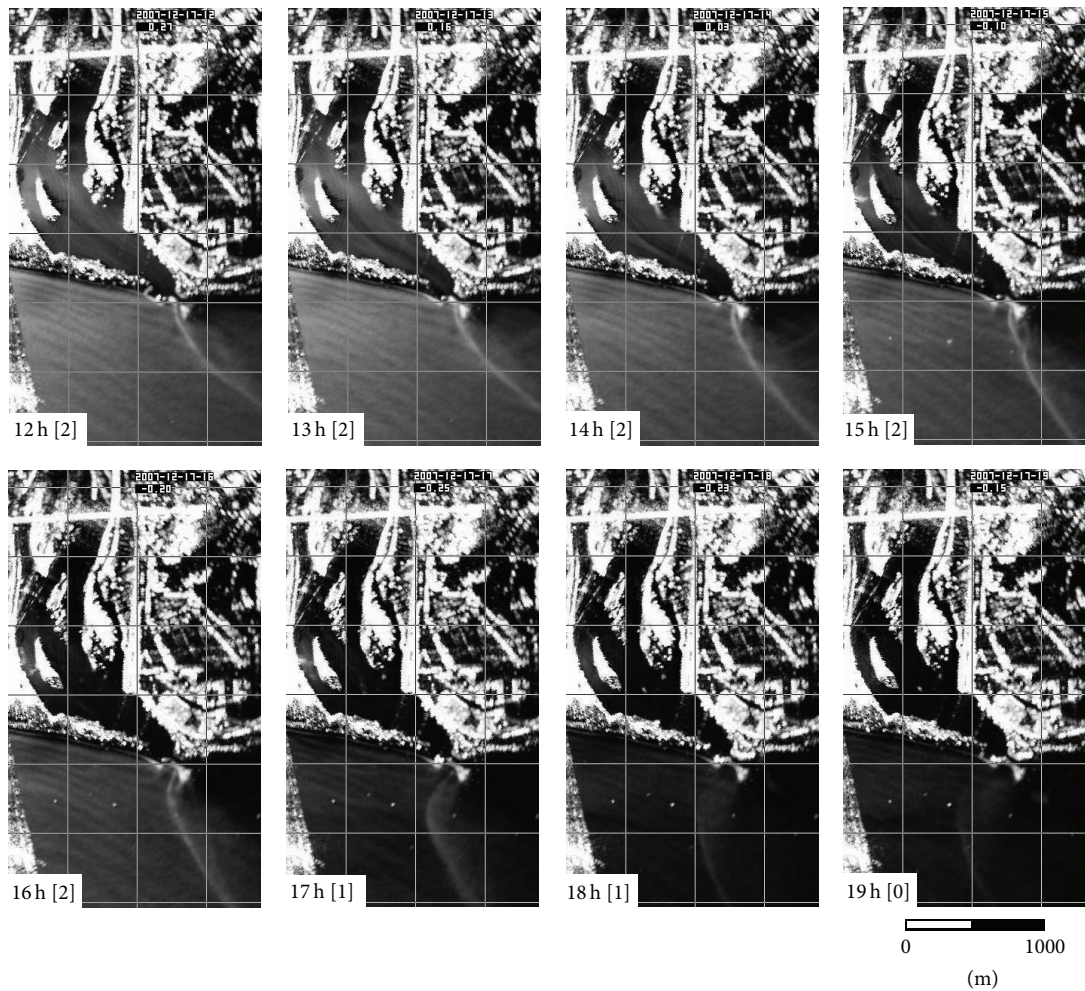


FIGURE 2: Sequence of time-averaged radar images during ebbing period of 17 December, 2007, 12:00–19:00. Each square of the grid corresponds to a square of 500 m. The number in bracket is the definition of the river plume front, or the front intensity, assessed by inspection.

time-averaged radar image. The sea surface close to the river's mouth captured in the satellite image has a complex texture; the color of the sea surface changes abruptly along the streaks, which extend broadly in a net-like manner. Waves approaching the shore during the period of observation had modest heights and are captured as parallel patterns with short wave lengths. A streak in the time-averaged radar image extends offshore from the river's mouth along a path similar to that of one of the streaks observed in the satellite image. Figure 3(b) shows another comparison between an optical image and time-averaged radar images. An outflow of turbid water from the river to the sea is clearly captured in the satellite image, forming a sharp color front extending offshore from the river's mouth. In the time-averaged radar images, a vertical streak extends from the mouth in a manner similar to that in the satellite image. The streak migrates slightly to the west in one hour.

The two comparisons shown here suggest that streaky patterns in the time-averaged radar images correspond to changes of sea surface texture or so-called color fronts formed on the sea in front of the river's mouth.

4. Field Observations

In the preceding section, satellite images were used to confirm the origin of the streaky patterns captured in the time-averaged images. Field observation data will be displayed here for further corroboration.

An in situ towing measurement of water temperature, salinity, and turbidity was conducted across the river plume front on 24 July, 2008, just after a satellite observation was done, simultaneously with the radar observation as summarized in Figure 4. The ship's path is juxtaposed in Figure 4(a) with the streaky feature, or the river plume front, captured in the time-averaged radar image. The ship crossed the front two times, approximately at 12 h 12 m and 12 h 24 m. Figure 4(b) is a photo taken from the ship looking towards the river's mouth at the moment when the ship crossed the front approximately at 12 h 12 m. A westerly wind with a speed of 1.4 m/s for this period was measured at the Iwata weather station, Japan Meteorological Agency, shown in Figure 1(a). The color and roughness of the sea surface suddenly change along a strip extending from the river's mouth. Since the wind field may

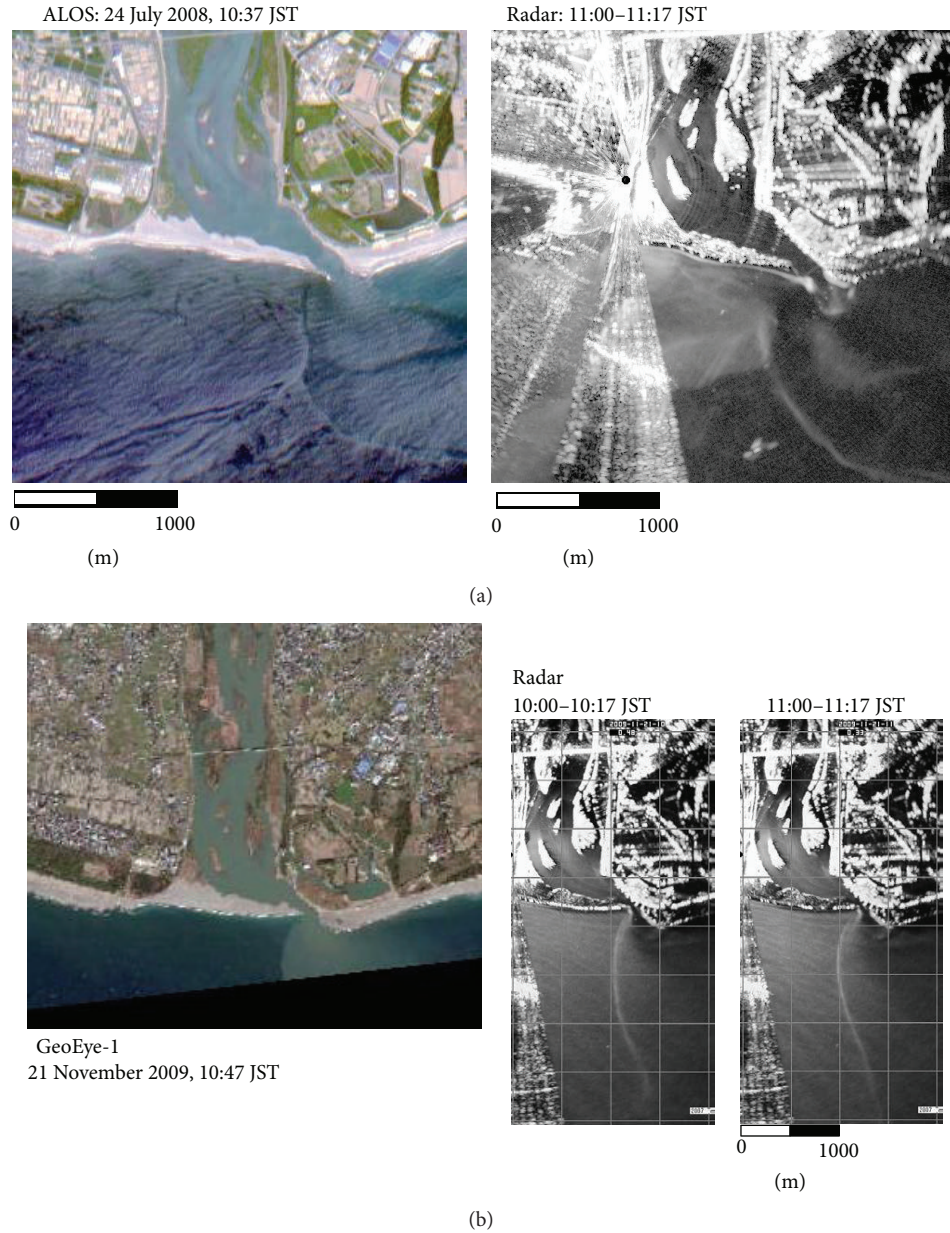


FIGURE 3: Comparisons between satellite images and time-averaged radar images. (a) Satellite image: ALOS (24 July, 2008, 10:37) and time-averaged radar image (24 July, 2008, 11:00–11:17), (b) satellite image: GeoEye (21 November, 2009, 10:47) and time-averaged radar images (21 November, 2009). The ring-shaped features which appear in the time-averaged images of the lower panels are due to some interference in the radar observation; however, its cause is not known.

be regarded as locally uniform in the vicinity of the mouth, the gap in roughness must be due to the internal structure of the flow field beneath the water's surface, which affects the propagation and deformation of the locally generated surface ripple waves.

Figure 4(c) presents the time histories of the mean turbidity and salinity records measured with a data logger CTD manufactured by Alec Electronic Instruments. Turbidity is measured from the amount of infrared backscatter and salinity, from conductivity. Data were sampled at a rate of 2 Hz, and the instrument was kept at a depth of 1 to 2 m

from the water's surface. The eastern area of the river plume front, denoted as "plume," is the area that should be under the influence of the river water; the salinity is relatively low and the turbidity is high compared to those measured in the western area of the river plume front, denoted as "ocean." This suggests that the change in water surface color observed from the ship is due to the difference in concentration of suspended solids between the river and the sea water.

Figure 4(d) shows the vertical water temperature distribution measured with a thermistor chain of length approximately 7 m. A thermal stratification was formed by solar

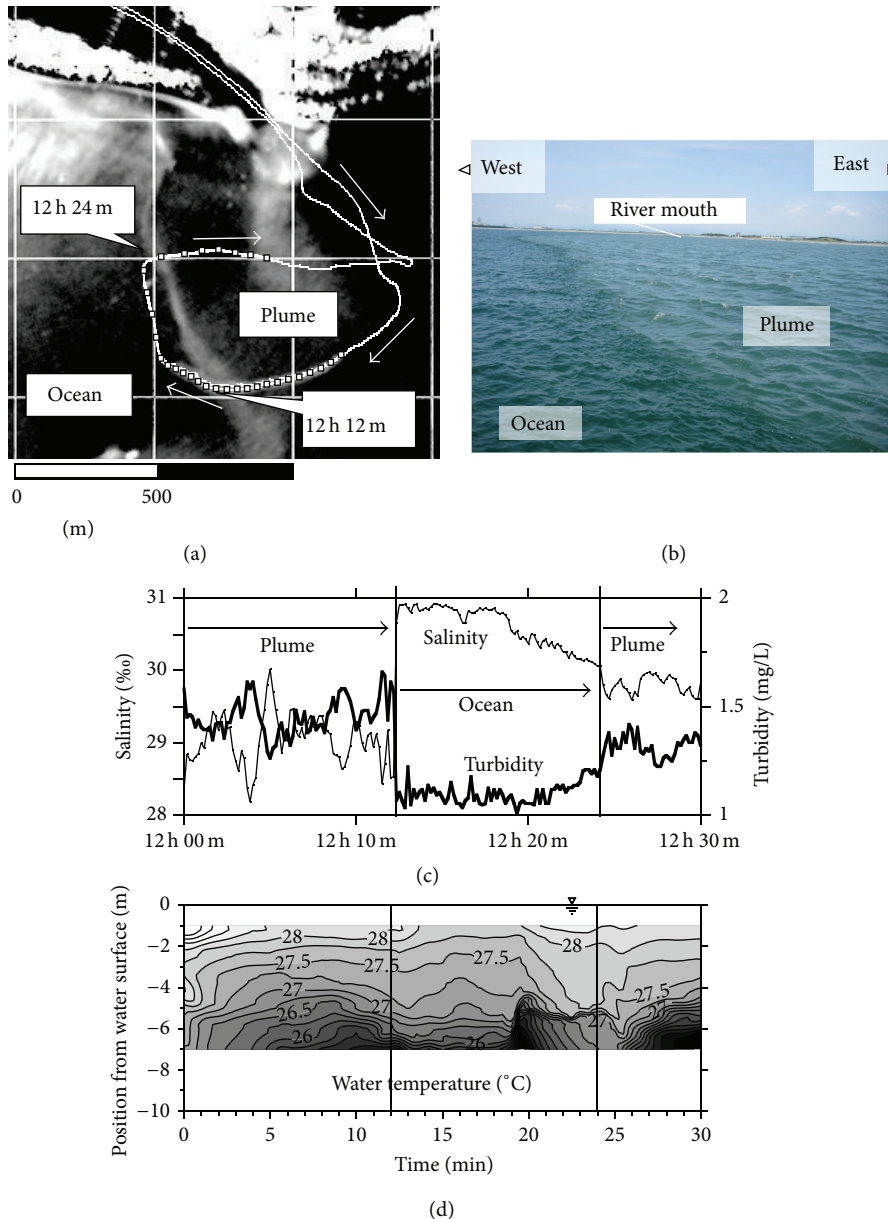


FIGURE 4: Result of in situ measurements across the river plume front. (a) Path of the survey ship through the river mouth and the river plume front 24 July, 2008, 12:00–12:30. Times in the panel denote moments of the crossings of the front. “Plume” is the area under the influence of the river water, where the salinity is relatively low and the turbidity is high compared to those of “ocean.” (b) Picture photographed from offshore of the river mouth looking towards the north-northeast. The left side of the front is ocean and the right side is plume. Time histories of (c) salinity, turbidity, and (d) vertical water temperature distribution observed in the vicinity of the river plume front.

radiation, and water was mixed weakly under calm sea conditions. When the ship was crossing the front from ocean to plume between 12 h 20 m and 12 h 25 m, stratification close to the water surface vanished, and warm water was found at a depth of 5 m below the surface where the water was well mixed in the vertical. Luketina and Imberger [3] and Marmorino and Trump [4] discuss mixing processes along a river plume front and claim that flow convergence at the front accompanied with a strong downwards flow mixes the water vertically and weakens the stratification. The local

uniform temperature distribution observed in this measurement might be formed from the same flow mechanism.

The observational results described here support the assertion that the streaky pattern captured in the time-averaged radar images corresponds to a river plume front formed by the discharge of fresh water from the river. There must be a convergence zone along the front that increases the steepness of surface ripple waves resulting in higher radar backscatter and concomitant bright strips in the radar image.

5. Capability of the X-Band Radar to Observe River Plume Fronts

In the previous sections, we confirmed that the streaky patterns captured in the time-averaged radar images correspond to the river plume fronts. We will discuss here the detection capability of river plume fronts with the X-band radar.

As shown in Figure 2, the definition of the streaky pattern, or the river plume front, varies in the time-averaged radar images. To explore the dependence of visibility on various environmental conditions, a collaborator assessed the definition of the river plume fronts, or the front intensity, into three levels by visual inspection: 0 for absent, 2 for well defined, and 1 for intermediate definition (see the bracketed digits in the captions of Figure 2). The relationship between this subjective assessment and environmental conditions is discussed first from the comparison of the hourly variation of the front intensity and river water level and wind speed and direction and then from a statistical viewpoint in the following.

Figure 5 displays some environmental conditions for one week in December of 2007: the variations of hourly water level record in the river channel and of the river plume front definition with the rate of change of the hourly water level of the river channel, the hourly wind speed and direction displayed as vectors, and a projection of the square of the wind speed along the east-west direction. Some examples of time-averaged radar images captured during this period are already shown in Figure 2. The water surface levels were measured at the Nakanomachi gauging station, 9 km from the river's mouth, and the Kakezuka gauging station, 4 km from the mouth in the tidal range (both stations operated by the Ministry of Land, Infrastructure, Transport, and Tourism). Wind speed and direction were measured at the Iwata weather station, 9 km northeast of the mouth (operated by the Japan Meteorological Agency). See Figure 1(a) for their locations. The area is a fluvial plain, and the ground level of the weather station is 1 m above the mean sea level. The anemometer is mounted at a height of 10 m from the ground. The 10-minute means of wind speed and direction are released by the agency every hour with a resolution of one meter per second and in sixteen azimuth directions.

The water level measured at Nakanomachi is constant, showing that there was no fluctuation in the river flow during the period. Since the Kakezuka gauging station is in the tidal range, the drift in the daily mean of the water level might be affected by factors such as the phase of the tidal cycle, wave breaking, and the corresponding wave setup at the river's mouth (Figure 5(a)). Nevertheless, the rate of water level change scatters around zero and is being used as an approximate indicator for the tidal flow rate at the river mouth (Figure 5(b)). The square of the easterly projection of the wind speed is displayed as an indicator of the wind stress component along the coast, which should promote the growth of ripple waves propagating alongshore (Figure 5(d)).

The diagrams indicate that the definition becomes larger mostly when the water level is falling, or the tide is ebbing, and the river water merges with the sea. There is, however, a period with no river plume front apparent in the images

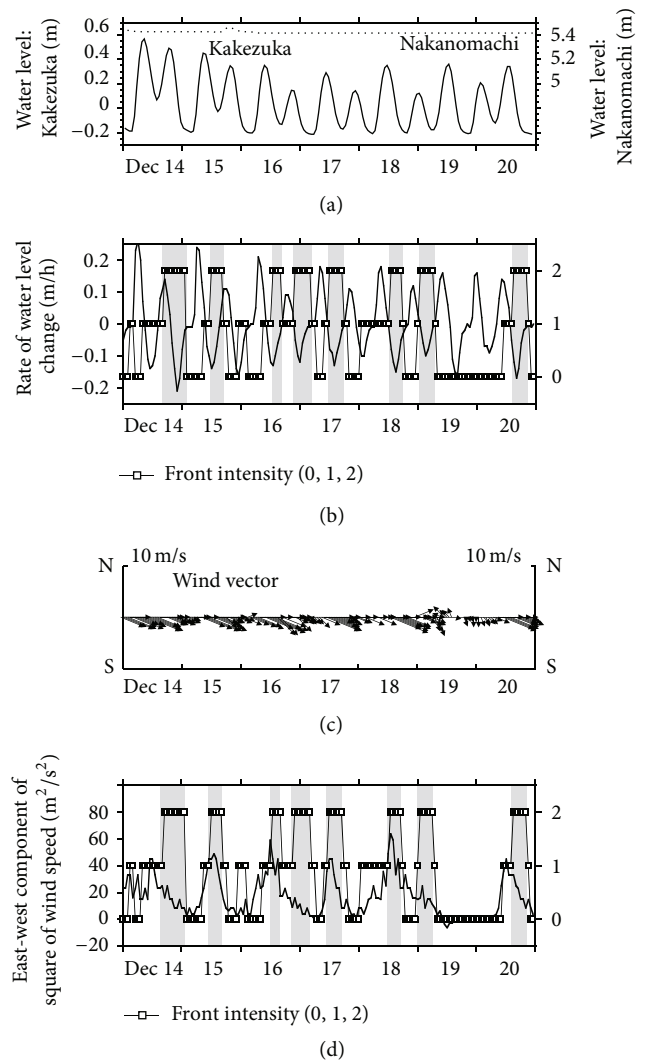


FIGURE 5: Variations of (a) water levels measured at gauging stations in the river channel: Nakanomachi, 9 km, from the river mouth, and Kakezuka, 4 km, from the river mouth, (b) definition of the river plume front (thin solid line with open square) captured in the time-averaged radar image (right axis) and rate of water level change at Kakezuka (solid line, left axis), (c) wind vector measured at Iwata weather station, and (d) square of east-west projection of wind speed (solid line, left axis), for the period of 14 to 20 December, 2007. Refer to Figure 1 for the locations of the gauging and weather stations.

even though the water level was decreasing. During these periods, from 8 h of 19th December, 2007, to the 10 h of 20th, the wind speed as well as the easterly projection of the square of the wind speed was small compared to other periods, suggesting that wind speed and direction play an important role in detecting the river plume front with the radar.

Macroscopic dependence of the river plume front definitions on the water level variation and wind speed and direction has been assessed with the time-averaged radar images collected for a year, from June, 2007, to May, 2008. Of 7302 images, 880 images were classified into definition level 2, 1810 into level 1, and 4612 into level 0. Figure 6

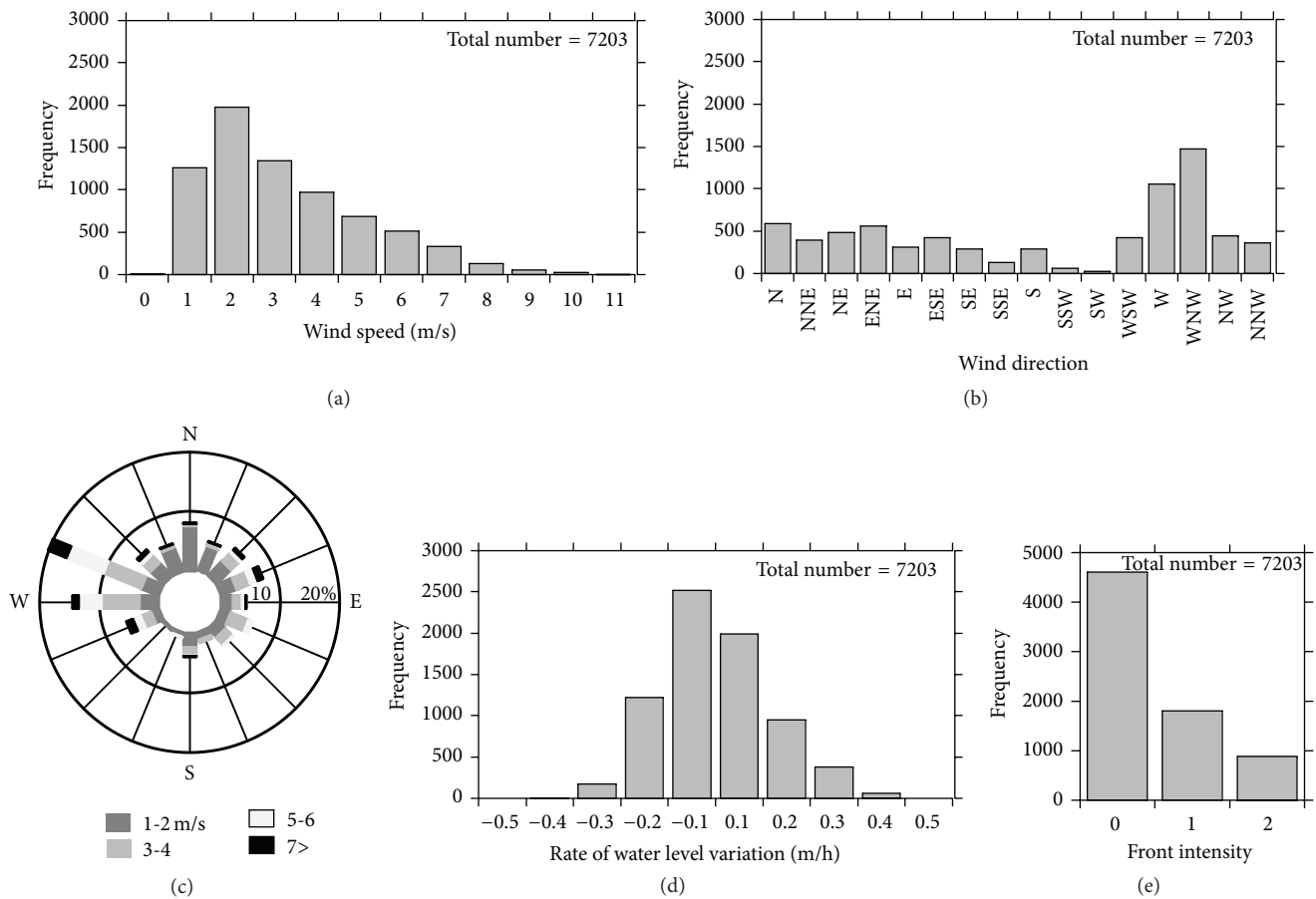


FIGURE 6: Histograms of (a) wind speed, (b) wind direction, and (c) wind rose measured at the Iwata weather station, histograms of (d) rate of water level variation measured at the Kakezuka gauging station, and (e) front intensity for the period of June, 2007, to May, 2008. Number of analyzed events is 7302.

contains histograms of wind speed and direction, wind rose measured at the Iwata weather station, and histograms of the rate of water level variation measured at the Kakezuka gauging station and the front intensity for the period of June, 2007, to May, 2008. The prevailing winds from WNW and W are observed mostly in the winter. The histogram for the rate of water level variation suggests that sea water intrusion into the river channel during tidal flooding periods is larger than the outflow during ebbing periods.

Figure 7 has distributions of the mean front intensity and wind speeds with respect to the rate of water level variation and wind direction. The mean of the front intensity (top row) is estimated from a simple arithmetic average, and its breakdown is given in the bottom row. The middle row displays the wind speed components in the north-south and east-west directions estimated from the average of the absolute value of the projections of the wind velocity vector. All the panels in the middle row indicate that the strength of the wind remained relatively constant during tidal cycles.

Figure 7(a) shows the results for all wind conditions (number of events $n = 7302$), whereas Figures 7(b) and 7(c) show the results for east/west winds ($n = 4245$) and

north/south winds ($n = 1819$). These results suggest higher definition is frequently observed when the water level is falling and the wind is blowing along the coast. In contrast, the definition decreases when the wind blows perpendicular to the coast, that is, for southerly and northerly winds. Since the number of samples for north/south winds is small compared to those for east/west winds, another result for east/west wind speeds below 2 m/s is given in Figure 7(d) ($n = 1061$). This result assures that the smaller definitions for north/south winds are not due to the fewer occurrences and low wind speeds; mean front intensities for east/west winds are higher even for lower wind speeds compared to those for north/south winds, implying the radar can better detect the occurrence of river plume fronts when an east or west wind is prevailing.

Table 1 shows the joint distribution of mean front intensity of the river plume front for different wind directions and wind speeds. Higher definition is frequently observed when the wind is blowing along the coast and the wind speed exceeds 3 m/s. The definition becomes relatively smaller when the wind blows perpendicular to the coast, that is, for south and north winds. This result again suggests the radar is not capable of detecting the occurrence of river plume fronts

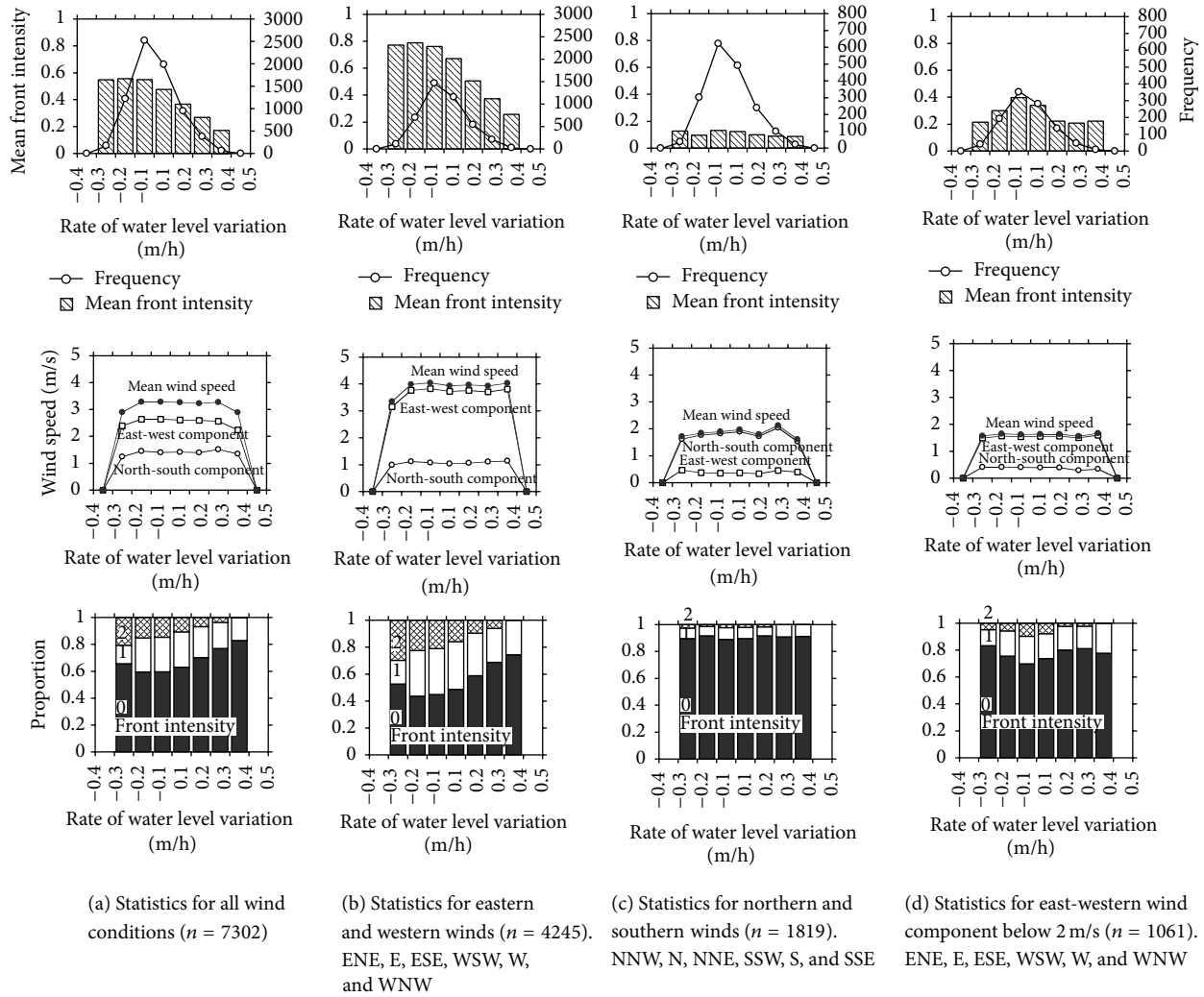


FIGURE 7: Mean front intensity and wind speed with respect to the rate of water level variation. Top row: mean front intensity and frequency of events. Middle row: mean wind speed and means of absolute value of east-west and north-south wind components. Bottom row: proportions of front intensities identified (a) for all wind conditions, (b) for east and west winds, (c) for north and south winds, and (d) for east and west winds below 2 m/s. Class “0.1 m/hour” is for the range of 0.0 m/hour to 0.1 m/hour and “-0.1 m/hour” for -0.1 m/hour to 0.0 m/hour.

in weak wind conditions or when a north or south wind prevails.

6. Discussion and Concluding Remarks

The radar detects reflection from the ripple waves by Bragg scattering [14], which becomes stronger when the directions of the radar beam emission and surface water wave propagation match. It is confirmed that the streaky features captured in the time-averaged radar images represent the river plume fronts, the boundary lines between the river and sea water. The imaging by the radar is schematically shown in Figure 8. If river and sea water meet, a strip extending offshore from the vicinity of the river’s mouth is formed, along which current convergence and a resulting downwards flow occur. This is confirmed from the results of field measurements of temperature distribution. Previous reports also depict similar flow structures along the front [3, 4]. Local winds cause

growth of ripple waves along the wind direction. As these waves travel across the river plume front, they are amplified and steepened by the convergence flow and cause a higher return signal of the emitted radar beam along the river plume front. This conclusion is supported by the fact that the definition of the river plume front is lesser when the alongshore wind speed is small or when north or south winds prevail. Since the river plume fronts extend mostly in the north-south direction due to the orientation of the river’s mouth, any ripple waves generated by north/south winds travel along the front and are consequently amplified at the front only slightly.

Alpers [9] discusses the imaging mechanism of oceanic internal waves with satellite radars, which is similar to the present discussion. If an internal wave exists, horizontal flows are induced along the sea surface, resulting in local amplification of surface waves and higher backscatter of radar beams emitted from space by enhanced Bragg scattering.

TABLE 1: Mean front intensity of the river plume front with respect to the wind speed and direction. The frequency is the number of images in the category. The three numbers shown in the breakdown denote the percentage of images assessed with front intensities of 0, 1, and 2, respectively.

Wind speed [m/s]	Wind direction		
	NWN, N, NNE SSW, S, and SSE	NW, NE SW, and SE	ENE, E, ESE WSW, W, and WNW
>6			
Mean front intensity	0.29	0.79	0.96
Frequency	35	199	1497
Breakdown [%]	(77, 17, and 6)	(38, 45, and 17)	(31, 42, and 27)
3, 4, and 5			
Mean front intensity	0.24	0.36	0.60
Frequency	463	611	2284
Breakdown [%]	(80, 16, and 4)	(72, 21, and 7)	(54, 31, and 15)
1 and 2			
Mean front intensity	0.07	0.16	0.24
Frequency	1321	427	465
Breakdown [%]	(94, 5, and 1)	(88, 8, and 4)	(81, 14, and 5)

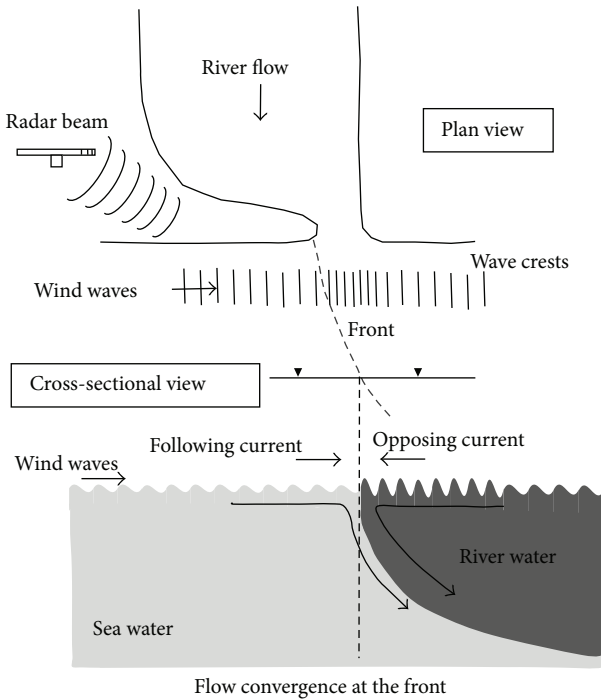


FIGURE 8: Schematic of imaging mechanism of the river plume front by the X-band radar. Flow convergence at the front amplifies local wind waves that propagate across the plume and on the opposing current, yielding higher backscatter of the emitted radar beam.

In addition, the present study demonstrates that the amplification mechanism is dependent on the wind direction and confirms the visibility of the features in the radar images, which has not been discussed before.

Marmorino et al. [15] report observations of oceanic fronts approaching the shore with land-based X-band radar at Duck, North Carolina, USA. The observational setup is similar to the present; a horizontally polarized radar is employed at a grazing angle. They do not explain the details of the imaging mechanism; however, convergence flow at the surface should have amplified the surface waves yielding higher backscatter.

In summary, we have the following:

- (1) Time-averaged X-band radar images of the mouth of the Tenryu River capture river plume fronts extending offshore from the river's mouth as bright streaks.
- (2) Comparisons between satellite optical images and time-averaged radar images confirm that streaky features in the time-averaged radar images represent color fronts, or river plume fronts. Further corroboration comes from field observations of water temperature, salinity, and turbidity conducted simultaneously with the radar measurement across the river plume front. When the survey ship crossed the river plume front (confirmed by visual inspection from the ship), the measured properties varied discontinuously, suggesting that water from the river and sea met there and also that a downwards current was present.
- (3) The definition of the river plume front varies in the time-averaged radar images. The definition was visually assessed and compared with the rate of water level variation and with the wind speed and direction. The radar captures well river plume fronts when the river water level is decreasing and the wind speed exceeds 3 m/s alongshore. The wind generates ripple waves, causing higher backscatter of the emitted radar beam

when they travel across the plume. The observations are expanded upon to illustrate a detailed imaging mechanism of the river plume front with X-band radars.

Highlights

- (i) A land-based X-band radar was employed to observe river plume fronts.
- (ii) Features captured in the radar images were checked against satellite and field data.
- (iii) The fidelity of radar observation of fronts was assessed and found to be correlated to wind direction.

Conflict of Interests

The author declares that there is no conflict of interests regarding the publication of this paper.

Acknowledgments

The author is grateful for the support by Mr. Takahashi Yu and Takahashi Ryo, former graduate students, and Professors Sato Shinji and Tajima Yoshimitsu of the University of Tokyo in the field observations. Mr. Takahashi Yu's laborious assistance in the determination of the front intensity is especially highly appreciated. This research is supported by the Special Coordination Funds for Promoting Science and Technology of the Ministry of Education, Culture, Sports, Science, and Technology, and the River Fund, The Foundation of River & Watershed Environment Management. Finally, the author is thankful to the anonymous reviewers who carefully checked the initial draft and gave informative suggestions to improve the work.

References

- [1] L. F. Kilcher and J. D. Nash, "Structure and dynamics of the Columbia River tidal plume front," *Journal of Geophysical Research: Oceans*, vol. 115, no. 5, Article ID C05S90, 2010.
- [2] R. W. Garvine and J. D. Monk, "Frontal structure of a river plume," *Journal of Geophysical Research*, vol. 79, pp. 2251–2259, 1974.
- [3] D. A. Luketina and J. Imberger, "Characteristics of a surface buoyant jet," *Journal of Geophysical Research*, vol. 92, pp. 5435–5447, 1987.
- [4] G. O. Marmorino and C. L. Trump, "Gravity current structure of the Chesapeake Bay outflow plume," *Journal of Geophysical Research: Oceans*, vol. 105, no. 12, pp. 28847–28861, 2000.
- [5] M. Pritchard and D. A. Huntley, "A simplified energy and mixing budget for a small river plume discharge," *Journal of Geophysical Research: Oceans*, vol. 111, no. 3, Article ID C03019, 2006.
- [6] U. Wolff, J. Seemann, C. M. Senet, and F. Ziemer, "Analysis of morphodynamical processes with a nautical X-band radar," in *Mustererkennung 1999—21. DAGM-Symposium Bonn, 15–17 September 1999*, Informatik aktuell, pp. 372–380, Springer, Berlin, Germany, 1999.
- [7] K. Hessner, A. Rubino, P. Brandt, and W. Alpers, "The Rhine outflow plume studied by the analysis of synthetic aperture radar data and numerical simulations," *Journal of Physical Oceanography*, vol. 31, no. 10, pp. 3030–3044, 2001.
- [8] D. A. Jay, J. Pan, P. M. Orton, and A. R. Horner-Devine, "Asymmetry of Columbia River tidal plume fronts," *Journal of Marine Systems*, vol. 78, no. 3, pp. 442–459, 2009.
- [9] W. Alpers, "Theory of radar imaging of internal waves," *Nature*, vol. 314, no. 6008, pp. 245–247, 1985.
- [10] W. Alpers, G. Campbell, H. Wensink, and Q. Zheng, "Underwater topography," in *Synthetic Aperture Radar Marine User's Manual*, chapter 10, US Department of Commerce, National Oceanic and Atmospheric Administration, 2004.
- [11] R. Romeiser and W. Alpers, "An improved composite surface model for the radar backscattering cross section of the ocean surface. 2. Model response to surface roughness variations and the radar imaging of underwater bottom topography," *Journal of Geophysical Research*, vol. 102, no. 11, pp. 25251–25267, 1997.
- [12] S. Takewaka, Y. Takahashi, Y. Tajima, and S. Sato, "Observation of morphology and flow motion at the river mouth of Tenryu with X-band radar," in *Proceedings of the Coastal Dynamics, Impacts of Human Activities on Dynamic Coastal Processes*, Tokyo, Japan, September 2009.
- [13] S. Takewaka, "Measurements of shoreline positions and intertidal foreshore slopes with X-band marine radar system," *Coastal Engineering Journal*, vol. 47, no. 2-3, pp. 91–107, 2005.
- [14] M. I. Skolnik, *Radar Handbook*, McGraw-Hill, 2nd edition, 1990.
- [15] G. O. Marmorino, A. L. Cooper, R. P. Mied, G. J. Lindemann, D. B. Trizna, and D. L. Porter, "Onshore propagation of a buoyant ocean front observed using a shore-based marine radar," *Continental Shelf Research*, vol. 24, no. 9, pp. 951–964, 2004.

Research Article

Monitoring Individual Wave Characteristics in the Inner Surf with a 2-Dimensional Laser Scanner (LiDAR)

Kévin Martins, Chris E. Blenkinsopp, and Jun Zang

Research Unit for Water, Environment and Infrastructure Resilience (WEIR), Department of Architecture and Civil Engineering, University of Bath, Claverton Down Road, Bath BA2 7AY, UK

Correspondence should be addressed to Chris E. Blenkinsopp; c.blenkinsopp@bath.ac.uk

Received 28 March 2015; Accepted 29 June 2015

Academic Editor: Jochen Horstmann

Copyright © 2016 Kévin Martins et al. This is an open access article distributed under the Creative Commons Attribution License, which permits unrestricted use, distribution, and reproduction in any medium, provided the original work is properly cited.

This paper presents an investigation into the use of a 2-dimensional laser scanner (LiDAR) to obtain measurements of wave processes in the inner surf and swash zones of a microtidal beach (Rousty, Camargue, France). The bed is extracted at the wave-by-wave timescale using a variance threshold method on the time series. Individual wave properties were then retrieved from a local extrema analysis. Finally, individual and averaged wave celerities are obtained using a crest-tracking method and cross-correlation technique, respectively, and compared with common wave celerity predictors. Very good agreement was found between the individual wave properties and the wave spectrum analysis, showing the great potential of the scanner to be used in the surf and swash zone for studies of nearshore waves at the wave-by-wave timescale.

1. Introduction

LiDAR in Coastal Engineering. The use of remote sensing techniques in coastal engineering has become increasingly popular during the past 3 decades. These instruments can provide measurements at temporal and spatial scales that are not reached by common *in situ* instruments. As an example, video imagery has been used for a wide range of applications: from bathymetric inversion [1] to alongshore swash motion variability [2].

Since remote sensors are nonintrusive instruments, they have the advantage of being easily and safely deployed on existing beachfront structures or specifically installed towers. Furthermore, instruments like the terrestrial LiDAR scanner (TLS) directly measure the wave profile and the wave properties (e.g., wave height and period) can subsequently be extracted. This represents an important advantage over other remote sensing techniques (e.g., video or radar) which are able to cover large domains but cannot directly obtain wave properties. Additionally, the ability of a single TLS to obtain data at multiple locations provides significant advantages over *in situ* sensors like pressure transducers, which are commonly used in surf zone studies but provide only point measurements.

The first reported experiment using a TLS to study wave processes is that of Irish et al. [3], who mounted a 4-rangefinder laser on a pier. A directional wave spectrum obtained with the scanner was compared to that from a submerged wave gauge, showing good agreement.

Recently, a few attempts were made to study the wave propagation or measure wave breaker heights. Harry et al. [4] investigated the potential of a 3D TLS to capture the water surface of a surf zone. Despite capturing the wave profile successfully, the time spent by the scanner to scan on the three dimensions was a major drawback since it introduced an alongshore time shift on the wave crest propagation. Their conclusion was that a 2D TLS might be a better alternative. Park et al. [5] also used a 3D TLS to measure breaker heights. They compared the scanner data with visual measurements against a vertical staff and obtained a relatively good agreement over the 26 measured waves, with a Root Mean Square Error (RMSE) of 5 cm. Individual wave height and celerity measurement was also made possible by combining the use of video camera and a 3D TLS, fixed on an automated robot, in Wübbold et al. [6]. Interestingly, this technique enabled the measurement of several alongshore points of the wave crest, allowing a 2-dimensional description of the wave propagation.

Swash zone data have been obtained using fixed 2D TLS instruments by Blenkinsopp et al. [10], Brodie et al. [11], and Almeida et al. [12], who demonstrated the ability of the instrument to measure swash hydro- and morphodynamics with high accuracy. The approach of Wübbold et al. [6] was also used by Vousdoukas et al. [13] in laboratory conditions to measure wave-by-wave events in the swash zone. Overall, it was found that the precision of such instruments was lower than that of ultrasonic altimeters which had previously been used to make such swash measurements; however the ability to capture small scale features due to the high spatial resolution and small measurement footprint compared to other remote sensors makes this instrument a powerful tool for coastal studies.

Known Drawbacks of the 2D-LiDAR for Wave Processes Studies. Previous studies [10, 14] have shown that an aerated and turbulent water surface is required for the laser to be sufficiently scattered to enable detection by the instrument. While, in the laboratory, this can be achieved by adding particulates to increase the water turbidity [15], this is not feasible in the field.

Fortunately, when the wave conditions are sufficiently energetic (wave breaking occurring), the surf and swash zones are very dynamic and are characterised by high levels of turbulence and aeration, which cause sufficient scattering for the consistent detection of the free surface elevation.

Environmental conditions (luminosity, air humidity, and wind) also have an impact on the scanner measurements. While the influence of humidity or water drops characterized by noise or spikes in data can be corrected, under high wind conditions the TLS can become too unstable for the data to be used. Indeed, while instrument accuracies are typically of the order of millimetres, the error induced by small oscillations of the instrument increases with distance from the instrument and can lead to measurement errors of the order of centimetres.

2. Experimental Setup

2.1. Site Location: Rousty. The experiment described in this paper was completed at Rousty beach, Camargue, which is located in the South of France on the Mediterranean Sea, from November 2014 until February 2015. The overall aim of the experiment was to study the coupling between the wave field, groundwater table dynamics, and the beach morphodynamics. It was organised in two different phases: a 10-day short-term and high-frequency phase within a 3-month long period of low-frequency measurements.

The site presents morphodynamic characteristics typical of the beaches in the National park of Camargue [16, 17]. Despite the microtidal environment (tidal range ~ 0.4 m), this part of the coastline presents very dynamic beach/dune morphologies. This region is subject to seasonal storms accompanied by storm surges that flood the low-lying area of the Camargue beaches [16]. This region is also exposed to very strong onshore wind episodes (mistral), which cause huge losses of sand due to aeolian transport [18].



FIGURE 1: Photograph showing the experimental setup and its location on the upper part of Rousty beach. The TLS was fixed on the 4.8-meter high tower standing on the left part of the picture while the scaffold is on the right. The buried sensors can be observed in between.

The high-frequency part of the experiments took place from the 8th to the 18th of December 2014 (10 days). During this period, 15 buried pressure sensors were deployed on the berm located at approximately 60 m from the dune system in addition to a laser scanner fixed on top of a 4.8 m high tower erected at the shoreline; see Figure 1. Both sets of instruments were logged by a computer placed on a scaffold structure, 16 m landward of the scanner.

2.2. Instrumentation. In this section, only the scanner instrumentation will be described since this paper focusses on the capacity of a commercial 2D scanner for inner surf and swash zones studies. During the Rousty experiments, the TLS used was a commercial LMS511 Laser Measurement System manufactured by SICK. This ranging device uses the time of flight method: the distance between two objects is calculated using the time required for an eye-safe pulsed beam ($\lambda = 905$ nm) to be detected after reflection from the target. This instrument is similar to that used by Blenkinsopp et al. [10] in terms of its function and specification.

The TLS has a range of 65 m and a 190° field-of-view with an angular resolution of 0.1667° and can be sampled at the sample rate of 25 Hz [19]. With this sampling rate, each spatial measurement location is measured 25 times per second, the instrument thus providing a total of 28500 measured points per second. During the experiment, a 4.8 m high tower was erected around the shoreline position for mounting the scanner and from this position it was possible to obtain measurements across the whole beach profile and into the inner surf zone (approximately 30% of the surf zone was covered in the present dataset). A schematic of the high-frequency experimental setup can be observed in Figure 2.

For the experimental setup at Rousty and using an angular resolution of 0.1667° , the distance between measurement points varied from 0.014 m at the Nadir point (zero grazing angle) to 0.25 m at the most seaward valid measurement location (Figure 3). This spatial resolution allows the detection of the instantaneous shape of small wave features, something that most conventional, point-measurement instruments such as pressure transducers or wave gauges are unable to do. The systematic error and spot

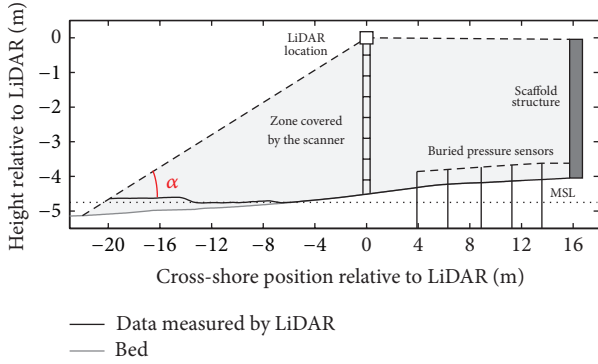


FIGURE 2: Schematic of the experimental setup at the Rousty experiments, for the 18 December 2014. The TLS, erected on top of a tower, covered a 35 m long zone from the scaffold structure where it was logged, to the point where the incident angle with the water surface (α) becomes too small for a sufficiently strong return signal. The cross-shore locations of the 15 buried pressure sensors are also shown (3 sensors were fixed to each buried pole, at different depths).

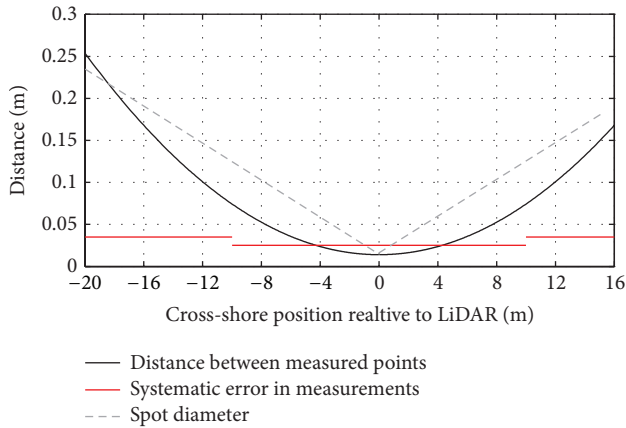


FIGURE 3: Distance between the points measured by the TLS (black line), for this experimental setup described in this paper. This value evolves from 0.014 m at the Nadir to 0.25 m at the most seaward captured location. The systematic error and the spot diameter provided by the manufacturer are also plotted (red continuous and grey dashed lines resp.).

diameter provided by the manufacturer [19] are also shown in the same figure. The systematic error naturally increases with increasing spot diameter and evolves from ± 0.025 m from 1 to 10 m from the scanner to ± 0.035 m between 10 and 20 m.

As the grazing angle between the laser beam and the target decreases (α , Figure 2), the signal reflected by the water surface and returning to the scanner gets weaker. While bore fronts can still be captured due to a more normal-oriented surface relative to the instrument, a signal is not always returned from a more horizontal surface (e.g., wave troughs), resulting in increasing gaps in the dataset as we move offshore. As a result, a cross-shore position of -20 m relative to the TLS was set as the seaward extent of the dataset for the extraction of wave properties. If we consider a plane surface, the minimum incident angle allowing good quality data with this specific scanner model was found to be around

13.5° . It is noted however that, since wave crests could still be followed from further offshore, the bore celerities were calculated from -22 m relative to the TLS, as discussed in Section 4.

3. Methodology

3.1. Preprocessing. Before analysing the dataset to study wave characteristics in the inner surf and swash zones, preprocessing is required. As in Almeida et al. [12], a beach survey carried out the same day as the dataset presented in this study (18 December 2014) was used to find the instrument orientation relative to the cross-shore profile. Data transformation from the scanner-centroid coordinate system to the cross-shore coordinate system is then possible from this analysis. This results in two arrays X and Z containing the cross-shore position and height relative to the scanner.

The dataset was despiked to reduce noise in the measurements and environmental effects such as splashes or people passing within the TLS field-of-view. Despiking the time series was achieved using gradient thresholds between two consecutive points. Then to reduce random noise, the dataset was time-averaged using a moving-window method (0.2 s) and spatially interpolated onto a regular cross-shore grid ($\delta x = 0.1$ m).

3.2. Bed Extraction. Since the instrument simply measures the distance to the closest target, no distinction on the medium is made, for example, water or sand. Due to the scanner's location in the swash zone which is alternatively dry and submerged, an important step in the data processing is to separate the water signal from the bed. The methodology used in this study to extract the bed follows the work of Almeida et al. [12].

Almeida et al. [12] calculated the time series variance over 4-second windows at every point on the regular grid. This methodology relies on the fact that the time series variance when the target is the exposed bed is much smaller than that from a moving water surface. Therefore, by defining empirical thresholds at every cross-shore location, one can extract data corresponding to stationary, dry bed. By defining a water depth criterion (0.015 m in this study) one can separate the original time series into separate "bed" and "wet" time series. This water depth criterion ensures that the noise in the measurements (of the order $O(\text{mm})$) is not interpreted as "wet" data.

By interpolating in time the extracted bed points, a beach profile can be obtained at each time step. This enables the monitoring of bed morphology at several hundred points and at the time scale of individual waves. An example of the result from this extraction is shown in Figure 4, where both accretionary and erosive swash events can be observed at $x = -10$ m.

3.3. Wave Properties Extraction. In order to obtain the individual wave characteristics at each point on the grid, a local maxima analysis was carried out on the surface elevation time series to detect the wave crests. This technique has been used in previous surf zone studies by Power et al. [20]

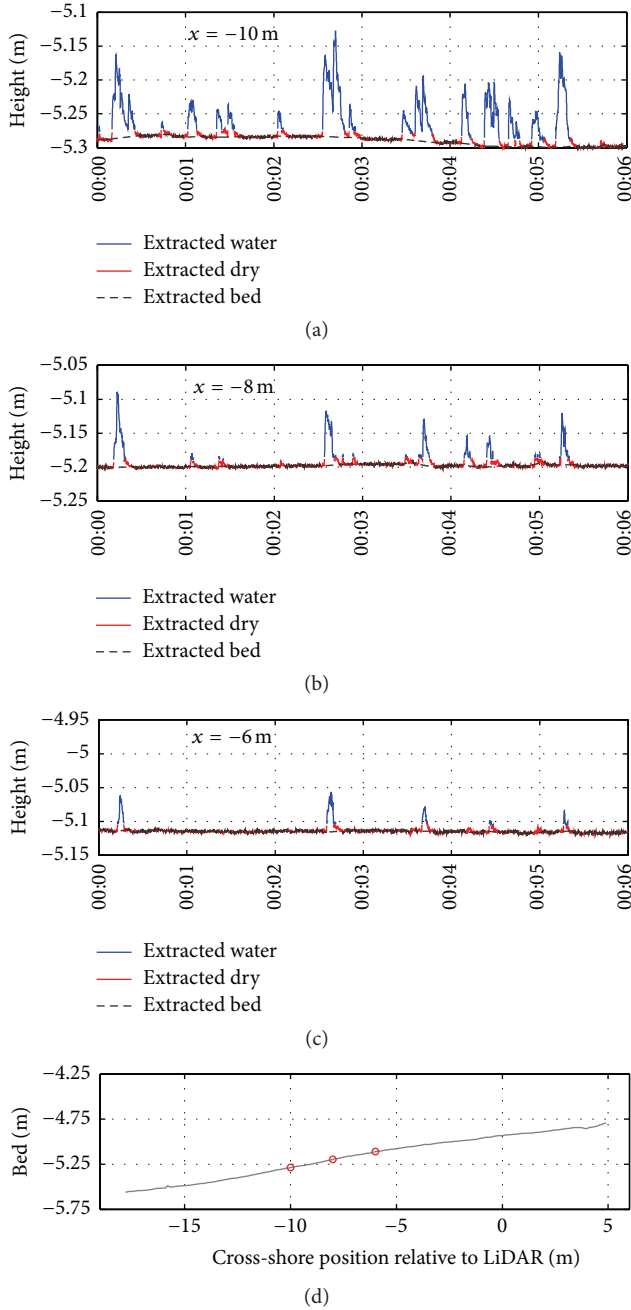


FIGURE 4: Example of bed extraction for the 14th of December. Three cross-shore positions are shown in panels (a), (b), and (c) and are represented by a red circle on the bed profile, in panel (d). The “wet” time series is represented in blue, the “bed” one in red, and the time-interpolated bed in grey. Interestingly, we can observe accretive and erosional patterns at the event time scale at the cross-shore position $x = -10$ m.

or Postacchini and Brocchini [21] because it is insensitive to low-frequency motions, unlike most common methods such as zero-down crossing which define waves relative to intersection between the instantaneous free surface elevation and mean sea level. When studying the surf zone and especially the inner surf where low-frequency motions can

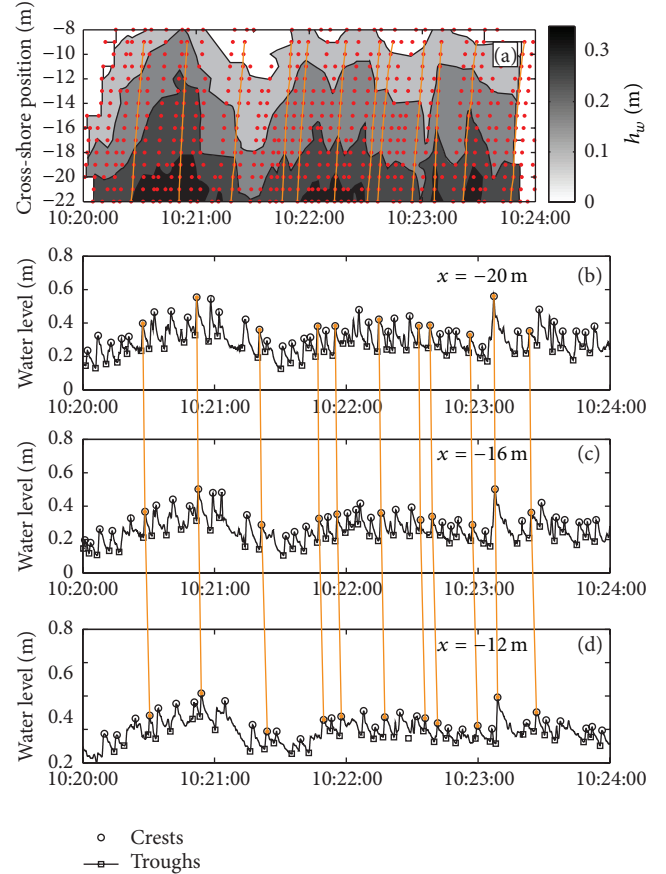


FIGURE 5: Example showing the wave extraction method in the inner surf zone. The wave-period-averaged water depth h_w contours are shown in (a), where red dots represent the detected wave crests. The orange lines are the waves selected in this time window for the celerity calculations. Panels (b), (c), and (d) represent the water surface elevations at three cross-shore locations, with the chosen waves tracked across them. Extracted wave crests and troughs are represented by black circles and squares, respectively.

be predominant, this aspect becomes critical since both the wave crest and trough can be under/above the defined mean water level. This is illustrated in Figure 5.

The wave troughs were defined as the minima reached between two crests and the wave period as the time elapsed between the passage of the troughs preceding and following a wave crest at the same location. A filter was applied to delete incorrect detections by limiting the time between 2 crests (2 s for this study). The wave height was defined as the elevation difference between the wave crest and trough elevations. Two other parameters were extracted, following the notation of Power et al. [20]: h_w is the wave-period-averaged mean water depth (mean surface elevation between the two troughs immediately before and after a crest), and h_{tr} is the trough depth. These are used for the analysis of individual wave celerities and the wave height to water depth ratio, γ .

3.4. Wave Celerities. To calculate the wave celerities, two different approaches have been used. The first one was

developed in the scope of this study and is based on a simple crest-tracking technique, allowing the estimation of individual wave celerities. The second uses a cross-correlation between two time series to calculate the averaged wave celerities over the time series length, following Tissier et al. [24].

Individual wave celerities were calculated every 1 m between the cross-shore locations $x = -21$ and -10 m using a tracking algorithm. This algorithm is initiated by manually choosing waves at the cross-shore position $x = -22$ m and storing the corresponding time index. At the next position ($x = -21$ m), the first detected crest after this time index is assumed to be the same wave. The same methodology is used to track the wave until $x = -9$ m and every time index is stored. The wave celerity at a cross-shore position x_i is then defined as the ratio of the distance between the two adjacent measurement points x_{i-1} and x_{i+1} (2 m) and the time elapsed between the passage of the wave crest at these two positions.

Due to the simplicity of the tracking algorithm and the difficulties caused by superposition of multiple waves within the inner surf, a careful visual inspection was carried out on all of the detected crests. Only waves not presenting obvious visual wave-wave interactions with other crests were selected. For the current study, this still enabled the detection of 275 waves and thus more than 3000 individual wave celerities. The process described above is illustrated for a 4-minute-period in Figure 5(a), where the selected waves for this time window are shown in orange.

Averaged wave celerities were calculated following the method of Tissier et al. [24]. The cross-correlation was calculated between two 10-minute time series from two cross-shore locations (separated by 2 m). The maximum correlation found between the two time series is the averaged time delay between the surface elevation features. Physically, it represents an estimation of the averaged wave celerity over the time series.

Using these two different methods to estimate the wave celerity is interesting in several aspects. The TLS data opens up the possibility to detect wave celerity and geometry in shallow water right up to the shoreline without any mathematical transformation on the measurements (e.g., Radon transform in Almar et al. [25]). The present dataset corresponds to shallower water than investigated by Tissier et al. [24]; thus the relationship between wave properties and celerity can be studied closer to the shoreline. Furthermore, the estimation of individual celerities will provide more insight into the dispersion of these values.

4. Results

4.1. Bed Monitoring. Following the methodology presented in Section 3.1, the bed morphology has been monitored using the bed time series. By subtracting the initial beach face profile from the measured profile at each time step, erosion/accretion patterns over the measurement period can be observed. An example is presented in Figure 6 where the erosion/accretion patterns are shown every minute, after window-averaging the extracted bed (15-second window), for

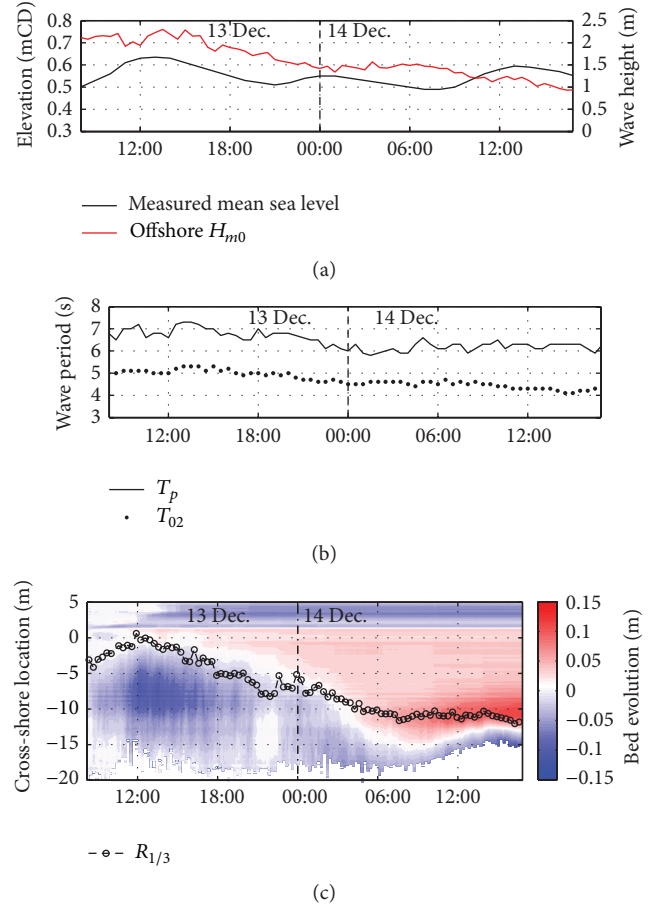


FIGURE 6: Bed extraction results: (a) measured mean water levels above Chart Datum at Fos-sur-Mer port and offshore significant wave height measured by a buoy close to Sete; (b) measured wave periods (T_p and T_{02}) by the same buoy; (c) beach morphological evolution for the 13th and 14th of December (30 continuous hours of measurement). Erosion and accretion patterns were calculated by subtracting the initial beach profile to that of the actual moment. Red color corresponds to accretion while blue corresponds to erosion. The significant run-up limit $R_{1/3}$ is shown as a circled black line.

the period of the 13th to the 14th of December (30 continuous hours). This corresponded to the most energetic period of the 10-day experiments (energy peak around 13 pm on the 13th of December).

Offshore wave conditions were measured by a buoy (data provided by CEREMA/DREAL Languedoc Roussillon) located 40 km west of Rousty beach, moored in a water depth of 30 m. Measured significant wave height and peak and mean spectral periods are shown in Figures 6(a) and 6(b), respectively. Mean water levels were obtained by a tidal gauge located at Fos-sur-Mer port (data provided by REFMAR/SHOM) (20 km east of Rousty). Interestingly, we can observe the influence of the tide even in this microtidal environment (high tides at 12:55 pm on the 13th, 1:25 am and 1:35 pm on the 14th). In addition to the direct influence on the mean sea level, a significant reason for these oscillations is thought to be the weaker energy dissipation during high

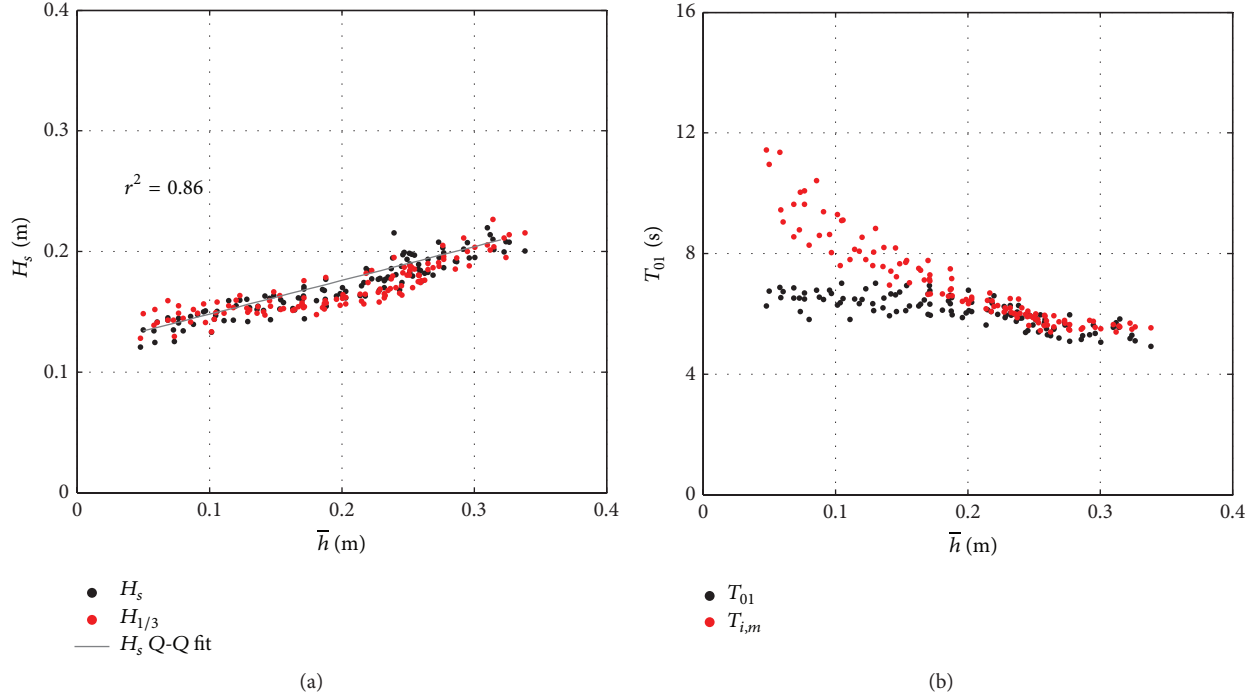


FIGURE 7: Comparison of (a) significant wave heights and (b) mean wave period calculated with two different methods: using the centroidal frequency inverse from spectral analysis (black dots) and averaged values over the same period of time, from an extrema analysis (red dots).

tides on this low-sloping barred beach [26]. During the first part of this storm event (9 am to 6 pm on the 13th of December), the swash zone profile flattened and experienced the strongest erosion (~ 0.15 m) between $x = -10$ and -5 m. When the conditions became milder, there is evidence of berm building centred around $x = -10$ m at a rate of approximately 10 mm/hr. This berm remained present until the end of the experiment, with evolving steepness depending on the offshore conditions.

4.2. Validation of the Extracted Wave-by-Wave Properties.

The methodology to extract wave properties based on the extrema analysis was compared to a classic spectral analysis (Figure 7). Significant wave height H_s was calculated by means of a Fast-Fourier transform on a 15-minute time series, between cutoff frequencies of 0.05 Hz and 0.5 Hz. H_s was compared to the averaged extracted wave height of the 1/3 highest waves $H_{1/3}$ from the wave-by-wave analysis described in Section 3.3, over the same period. The mean extracted individual wave period $T_{i,m}$ was compared to the mean wave period $T_{01} = m_0/m_1$, which is the inverse of the centroidal frequency, where m_n is the n th spectral moment that is defined as

$$m_n = \int_0^{\infty} f^n E(f) df \quad (1)$$

with $E(f)$ being the power density spectrum.

Plotted against the mean water depth over the same time period \bar{h} , H_s and $H_{1/3}$ show very good agreement at all water depths (Figure 7(a)), validating the extraction method

based on the local extrema analysis. Both statistical ($H_{1/3}$) and spectral (H_s) significant wave height were found to show little scatter and to linearly decrease with averaged water depth ($r^2 = 0.86$). Though such depth-dependence is generally observed when saturated conditions are found in the inner surf [27], the relatively short dataset (2h30) and the consistent offshore conditions do not allow for such statement. Furthermore, waves were found to stop breaking and reform between the two beach bars, consistent with unsaturated conditions [28].

In contrast to averaged values, measured individual wave heights showed considerably more scatter; see Figure 8(a). This scatter is explained by two main factors: the influence of infragravity motions and the presence of high-frequency waves increasing or lowering the wave trough height. Naturally, it is also visible in the individual wave height to water depth ratio $\gamma_w = H/h_w$ (Figure 8(b)), which shows increasing values as waves approach the shoreline, something previously observed by Sénéchal et al. [29] and Power et al. [20]. In particular, the wide range of observed individual γ_w values show the inappropriateness of choosing constant values for this parameter in numerical models. Finally, the individual γ_w values, obtained closer to the shoreline than these two previous studies, seem to be in agreement with the line fit obtained with averaged γ_w values by Power et al. [20].

The comparison between $T_{i,m}$ and T_{01} (Figure 7(b)) also shows interesting results. While, for the deepest waters considered ($h \geq 0.2$ m), the mean extracted individual wave periods are consistent with T_{01} , as we get closer to the shoreline, the difference between the two values increases with decreasing water depth. This analysis gives some support

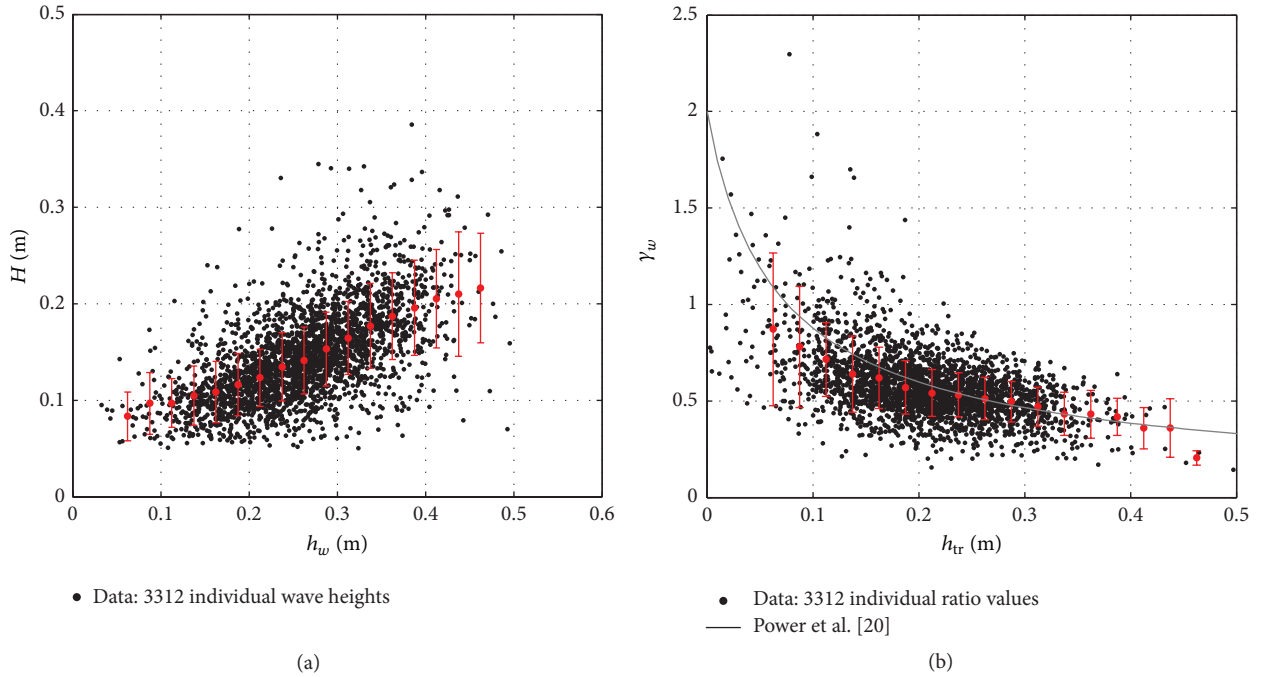


FIGURE 8: Individual wave properties: (a) wave height as a function of the wave-period-averaged water depth and (b) wave height to water depth ratio as a function of the depth under the trough. Standard deviations are shown by the red bars and are calculated for 0.025 m wide bins. In (b), the empirical fit equation obtained by Power et al. [20] using averaged γ_w values is shown as the gray line.

to the idea of using the centroidal frequency to define a characteristic period in the inner surf, as suggested by Raubenheimer et al. [23] and Sénéchal et al. [29].

4.3. Influence of the Characteristic Period on the γ Parametrization. To further compare the characteristic wave periods, the ratio between averaged significant wave height and water depths noted $\bar{\gamma}_s$ has been plotted against $\beta/\bar{k}\bar{h}$, which represents the fractional change in water depth over a wavelength. In this expression, β represents the bed slope, \bar{k} the wave number calculated from the averaged estimated celerities and a characteristic period, and \bar{h} the averaged water depth over the same period.

Two different comparisons were made (using the same typology as in Section 4.2):

- (1) Comparison shown in Figure 9(a) using $H_{1/3}$ for $\bar{\gamma}_s$ and $T_{i,m}$ to derive \bar{k} .
- (2) Comparison shown in Figure 9(b) using H_s for $\bar{\gamma}_s$ and T_{01} to derive \bar{k} .

For both comparisons, a strong linear dependence was found between $\bar{\gamma}_s$ and $\beta/\bar{k}\bar{h}$. For deeper water and using two different frequency cutoffs, Raubenheimer et al. [23] and Sénéchal et al. [22] found a similar linear relationship, but with different coefficients. For the present dataset and for both derived $\bar{\gamma}_s$, a good match is found with the linear fit obtained by Sénéchal et al. [22] when $0 \geq \beta/\bar{k}\bar{h} \geq 0.5$. For greater values of $\beta/\bar{k}\bar{h}$, lower values compared to Sénéchal et al. [22] are obtained when using the mean extracted wave

period T_m , while that using T_{01} still matches the linear fit. This limit value of $\beta/\bar{k}\bar{h}$ corresponds to the critical depth where T_{01} does not match $T_{i,m}$ any more (Figure 7(b)).

It is noted that the three compared datasets use different frequency cutoffs ($0.05 \text{ Hz} \leq f \leq 0.18 \text{ Hz}$ for Raubenheimer et al. [23], $0.09 \text{ Hz} \leq f \leq 0.3 \text{ Hz}$ for Sénéchal et al. [22], and $0.05 \text{ Hz} \leq f \leq 0.18 \text{ Hz}$ for the present study). Except for the influence of the much lower high-frequency cutoff used by Raubenheimer et al. [23], it is unclear why the present dataset shows higher values than in Raubenheimer et al. [23] but matches that of Sénéchal et al. [22]. Finally, it has to be noted that the dataset presented in this study contains much shallower depths than that considered in the two previous studies. For instance, the highest value of $\beta/\bar{k}\bar{h}$ considered by the previous studies was 0.25 while it is approximately 1.75 in the current work.

4.4. Wave Celerities. Individual wave celerities were compared to a range of previously developed predictors summarized in Table 1. In the different formulations, h , h_c , and h_t are, respectively, the mean water depths, the crest height, and the trough height. A more complete introduction to these predictors is given by Catalán and Haller [30] who compared a wider range of celerity predictors against measurements obtained using video imagery from laboratory experiments.

Prior to this work, only a few studies have been published on the measurement of individual broken-wave celerities in the surf zone. Radon transform on video camera data has been used by Yoo et al. [31] and Almar et al. [32] to track wave crests, while Tissier et al. [33] used a large array of

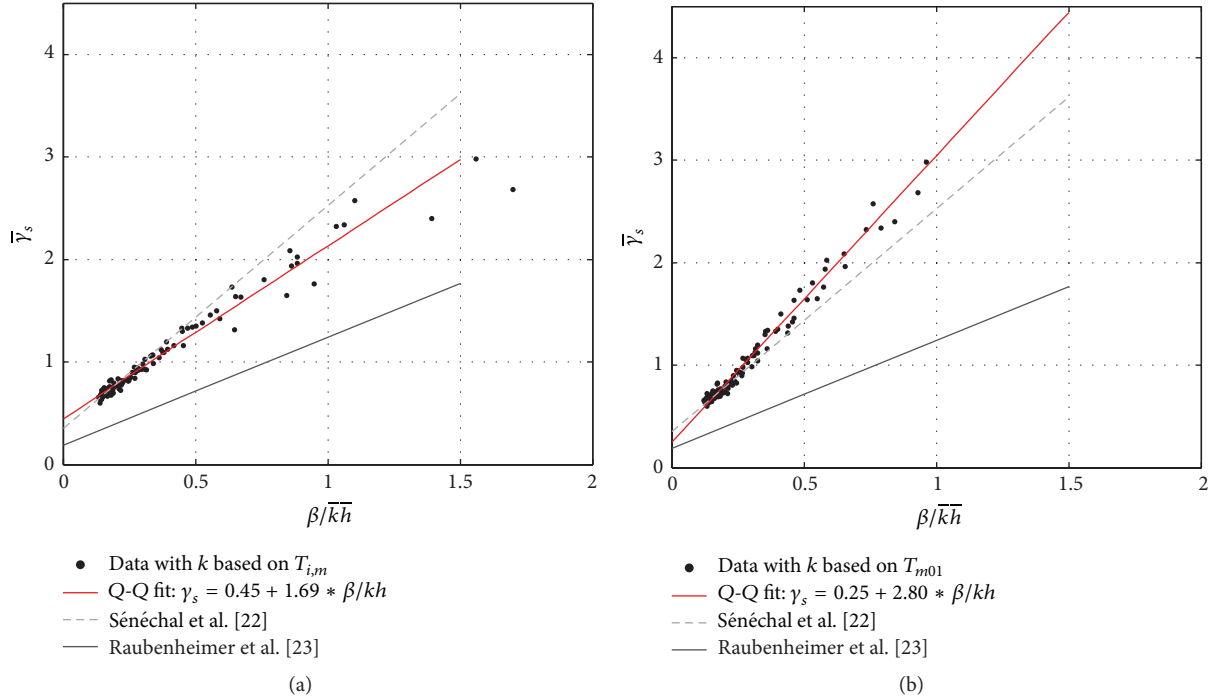


FIGURE 9: Averaged significant wave height to averaged water depth ratio plotted against $\beta/\bar{k}h$: (a) ratio calculated with \bar{k} based on the mean extracted individual wave period $T_{i,m}$; (b) ratio calculated with \bar{k} based on the mean spectral wave period $T_{m01} = m_0/m_1$, inverse of the centroidal frequency. The present dataset (black dots, and its Q-Q fit shown as red line) is compared to the fit obtained in two previous studies: dashed gray lines for Sénéchal et al. [22] and gray continuous line for Raubenheimer et al. [23].

TABLE 1: List of the different tested wave celerity predictors. For individual wave celerities, the mean water depth h becomes the wave-period-averaged mean water depth h_w .

Predictor	Formulation of c
Linear theory (shallow water assumption)	$c = \sqrt{gh}$
Modified shallow water formulation [7]	$c = 1.3\sqrt{gh}$
Solitary wave theory	$c = \sqrt{gh \left(1 + \frac{H}{h}\right)}$
Bore model [8]	$c = \sqrt{gh_c h_t \frac{(h_t + h_c)}{2h^2}}$
Shock model [9]	$c = -2\sqrt{gh} + 2\sqrt{gh_t} + \sqrt{gh_c \frac{(h_t + h_c)}{2h_t}}$

wave gauges for this purpose. Additionally, Postacchini and Brocchini [21] calculated individual broken-wave celerities by correcting the averaged celerities obtained by a cross-correlation method [24] for each detected wave. While Tissier et al. [24] found better agreement with Bonneton [9] predictor using averaged celerities, individual celerities from Postacchini and Brocchini [21] and this study were found to better match the solitary wave theory celerity; see Figure 10(a).

In contrast to the study of Tissier et al. [24] whose data was concentrated in the outer and midsurf zone, the present study uses data from the inner surf to the swash zone. In particular, this enables one to look more closely at the boundary between the two zones in terms of wave celerities using the cross-correlation method. This is illustrated in Figure 10(b), where the 10-minute averaged celerities are plotted against the corresponding averaged water-depth.

Between water depth of 0.2 and 0.4 m, the averaged celerities show good agreement with the modified shallow water wave predictor, though they are slightly underestimated. This is in agreement with the results found in Figure 10(a). Indeed, the modified shallow water wave predictor corresponds to the solitary wave predictor with a constant wave height to water depth ratio of 0.78. Hence, despite a not insignificant scatter when using the individual celerities (shown by Postacchini and Brocchini [21], not shown in this study), the modified shallow water predictor provides good estimates of the averaged wave celerities seaward of $h \geq 0.2$ m, corresponding to $\gamma = 0.5$ in this study; see Figure 8(b). Interestingly, for shallower depths, the averaged celerities remain quite constant slightly decreasing, to finally present a much broader value range at the shoreline position ($1.3 \text{ m}\cdot\text{s}^{-1} < c_b < 2.2 \text{ m}\cdot\text{s}^{-1}$). This scatter of averaged values implies a wider range of individual celerities at the surf-swash boundary, which could be explained by the interaction between surf and swash processes.

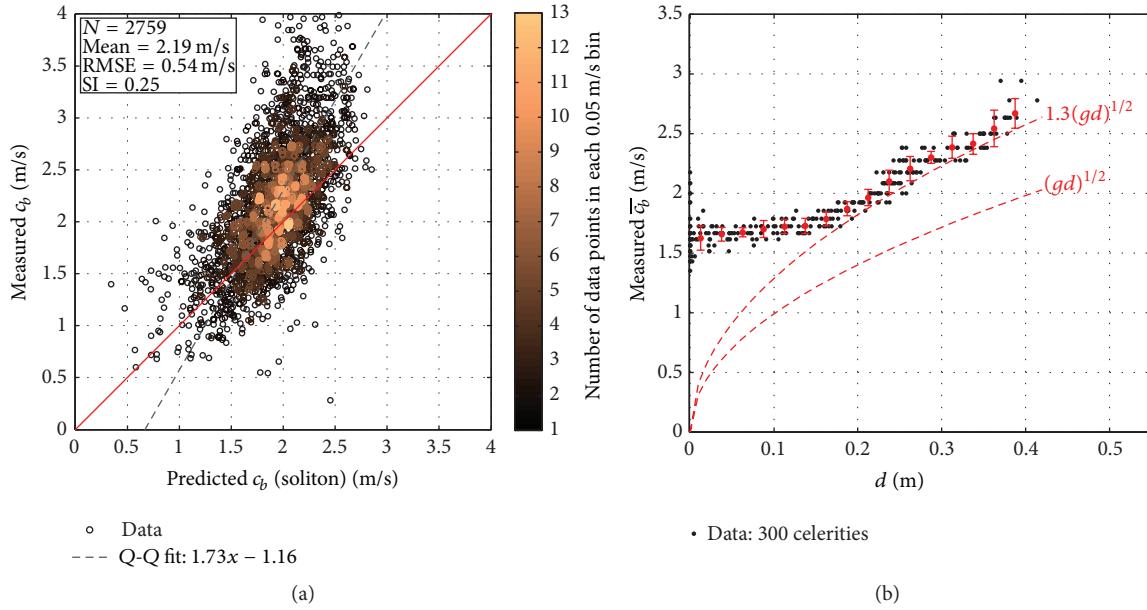


FIGURE 10: Scatter plot of measured wave celerities: (a) individual wave celerities against the predictor from the solitary wave theory. Data circles are coloured by their concentration in every 0.05 m/s bins. The wave-period-averaged depth is used for the soliton celerity formulation, following Postacchini and Brocchini [21]. Correlation coefficient $r = 0.65$; (b) averaged wave celerities obtained from the cross-correlation of two 10-minute time series, plotted against water depth. Their standard deviation is plotted as red bars, using 0.025 m wide bins. The modified and original linear wave theories in shallow water are represented in red dashed lines.

5. Conclusion

In this study, a methodology for monitoring the beach morphology and individual wave characteristics using a shore-mounted 2-dimensional commercial laser scanner has been presented. The conclusions of this investigation can be summarized with the following points:

- (i) The laser scanner can be used to measure time-varying water surface profiles in the inner surf and swash zones, enabling the study of wave propagation on a wave-by-wave as well as time-averaged basis.
- (ii) Individual wave properties (H , T) can be extracted using an extrema analysis on the measured time series. The extracted wave height was found to compare well with that from spectral analysis. It was also shown that for these conditions, the wave period derived from the centroidal frequency could be chosen as a characteristic wave period for water depths down to 0.2 m. Further investigation is needed on the reason why this changes at the swash/inner surf boundary.
- (iii) $\bar{\gamma}_s$ was found to be linearly dependent on $\beta/\bar{k}\bar{h}$. Furthermore, the present dataset seems to match well that of Sénéchal et al. [22], for values of $\beta/\bar{k}\bar{h}$ lower than 0.5. For higher values, discrepancies are observed and are due to the differences observed between T_m and T_{01} .

- (iv) Individual wave celerities were estimated using a simple crest-tracking method. Comparisons with various predictors showed that the solitary wave theory gave the best agreement with the present dataset. However, in the shallow water depths investigated here, these values exhibit considerable variability.
- (v) 10-minute averaged wave celerities were also calculated using a cross-correlation technique. These values agree well with the modified shallow-water predictor in depths greater than 0.2 m, becoming almost constant as the water depths decrease landwards. This critical depth also corresponds to that when T_m and T_{01} start to show discrepancies. Since the celerity is a function of the wave period, the two facts could be physically linked. This will be the subject of further investigation, since it could bring new insight into the conditions at the surf-swash boundary.

Appendix

Statistical Parameters

The different statistical parameters (Root-Mean Square Error, Scatter Index, and a correlation coefficient noted r) used in this study are defined in this section. If we denote the two

compared series as $X = \{x_1, \dots, x_n\}$ and $Y = \{y_1, \dots, y_n\}$, they are defined as follows:

$$\begin{aligned} \text{RMSE} &= \sqrt{\frac{1}{n} \sum_{i=1}^n (x_i - y_i)^2}, \\ \text{SI} &= \frac{\sqrt{(1/n) \sum_{i=1}^n (x_i - y_i - (\bar{X} - \bar{Y}))^2}}{\bar{X}}, \\ r &= \frac{\sum_{i=1}^n (x_i - \bar{X})(y_i - \bar{Y})}{\sqrt{(\sum_{i=1}^n (x_i - \bar{X}))^2 (\sum_{i=1}^n (y_i - \bar{Y}))^2}}. \end{aligned} \quad (\text{A.1})$$

Conflict of Interests

The authors declare that there is no conflict of interests regarding the publication of this paper.

Acknowledgments

This work was supported by EPSRC. The three anonymous reviewers are greatly acknowledged for their constructive comments on the paper. CEREMA/DREAL Languedoc Roussillon and REFMAR/SHOM are thanked for providing the offshore wave buoy and tide gauge data, respectively. Researchers from the institutions involved in this project, Damien Sous (MIO), Frédéric Bouchette (Géosciences Montpellier), François Sabatier, Samuel Meulé (CEREGE), Lise Petitjean (Ph.D. student, MIO and Géosciences Montpellier), and all the other Ph.D. students, are greatly acknowledged for the invitation to participate at this large scale experiment. The survey data used for calibrating the LiDAR was also much appreciated.

References

- [1] H. F. Stockdon and R. A. Holman, "Estimation of wave phase speed and nearshore bathymetry from video imagery," *Journal of Geophysical Research: Oceans*, vol. 105, no. 9, Article ID 1999JC000124, pp. 22015–22033, 2000.
- [2] R. M. C. Guedes, K. R. Bryan, and G. Coco, "Observations of alongshore variability of swash motions on an intermediate beach," *Continental Shelf Research*, vol. 48, pp. 61–74, 2012.
- [3] J. L. Irish, J. M. Wozencraft, A. G. Cunningham, and C. Giroud, "Nonintrusive measurement of ocean waves: lidar wave gauge," *Journal of Atmospheric and Oceanic Technology*, vol. 23, no. 11, pp. 1559–1572, 2006.
- [4] M. Harry, H. Zhang, C. Lemckert, and G. Colleter, "3D spatial definition of a water surface," in *Proceedings of the 9th ISOPE Pacific/Asia Offshore Mechanics Symposium*, Busan, Republic of Korea, November 2010.
- [5] H. S. Park, J. S. Sim, J. Yoo, and D. Y. Lee, "Breaking wave measurement using terrestrial lidar: validation with field experiment on the mallipo beach," in *Proceedings of the 11th International Coastal Symposium*, pp. 1718–1721, Szczecin, Poland, May 2011, (Journal of Coastal Research, Special Issue, No. 64).
- [6] F. Wübbold, M. Voudoukas, M. Hentschel, and B. Wagner, "Towards autonomous coastal monitoring using 3d laser range scanners and camera vision," in *Proceedings of the 33rd International Conference on Coastal Engineering*, Santander, Spain, 2012.
- [7] H. A. Schäffer, P. A. Madsen, and R. Deigaard, "A Boussinesq model for waves breaking in shallow water," *Coastal Engineering*, vol. 20, no. 3–4, pp. 185–202, 1993.
- [8] I. A. Svendsen, P. A. Madsen, and J. B. Hansen, "Wave characteristics in the surf zone," in *Proceedings of the 16th Conference on Coastal Engineering*, vol. 1, pp. 765–780, Hamburg, Germany, September 1978.
- [9] P. Bonneton, "Wave celerity in the inner surf zone," in *Proceedings of 29th International Conference on Coastal Engineering*, vol. 29, pp. 392–401, National Civil Engineering Laboratory, Lisbon, Portugal, September 2004.
- [10] C. E. Blenkinsopp, M. A. Mole, I. L. Turner, and W. L. Peirson, "Measurements of the time-varying free-surface profile across the swash zone obtained using an industrial LIDAR," *Coastal Engineering*, vol. 57, no. 11–12, pp. 1059–1065, 2010.
- [11] K. L. Brodie, R. K. Slocum, and J. E. McNinch, "New insights into the physical drivers of wave runup from a continuously operating terrestrial laser scanner," in *Proceedings of the Oceans*, pp. 1–8, Hampton Roads, Va, USA, October 2012.
- [12] L. P. Almeida, G. Masselink, P. E. Russell, and M. A. Davidson, "Observations of gravel beach dynamics during high energy wave conditions using a laser scanner," *Geomorphology*, vol. 228, pp. 15–27, 2015.
- [13] M. I. Voudoukas, T. Kirupakaramoorthy, H. Oumeraci et al., "The role of combined laser scanning and video techniques in monitoring wave-by-wave swash zone processes," *Coastal Engineering*, vol. 83, pp. 150–165, 2014.
- [14] A. J. Evans, "Laser scanning applied to hydraulic modeling," in *Proceedings of the International Archives of Photogrammetry, Remote Sensing and Spatial Information Sciences, Commission V Symposium*, Newcastle upon Tyne, UK, 2010.
- [15] M. J. Allis, W. L. Peirson, and M. L. Banner, "Application of lidar as a measurement tool for waves," in *Proceedings of the 21st International Offshore and Polar Engineering Conference (ISOPE '11)*, pp. 373–379, Maui, Hawaii, USA, June 2011.
- [16] F. Sabatier, "Modélisation de l'impact du changement climatique sur l'érosion des dunes. Application à la camargue," *La Houille Blanche*, no. 1, pp. 40–49, 2008.
- [17] F. Sabatier, O. Samat, A. Ullmann, and S. Suanez, "Connecting large-scale coastal behaviour with coastal management of the Rhône delta," *Geomorphology*, vol. 107, no. 1–2, pp. 79–89, 2009.
- [18] F. Sabatier, E. J. Anthony, A. Héquette et al., "Morphodynamics of beach/dune systems: examples from the coast of France," *Géomorphologie: Relief, Processus, Environnement*, pp. 3–22, 2009.
- [19] SICK, "Laser measurement sensors of the lms5xx product family—operating instructions," 2015, <https://www.sick.com/media/pdf/4/14/514/IM0037514.PDF>.
- [20] H. E. Power, M. G. Hughes, T. Aagaard, and T. E. Baldock, "Nearshore wave height variation in unsaturated surf," *Journal of Geophysical Research: Oceans*, vol. 115, no. 8, Article ID C08030, 2010.
- [21] M. Postacchini and M. Brocchini, "A wave-by-wave analysis for the evaluation of the breaking-wave celerity," *Applied Ocean Research*, vol. 46, pp. 15–27, 2014.
- [22] N. Sénéchal, H. Dupuis, P. Bonneton, H. Hova, and R. Pedreros, "Observation of irregular wave transformation in the surf zone over a gently sloping sandy beach on the French Atlantic coastline," *Oceanologica Acta*, vol. 24, no. 6, pp. 545–556, 2001.

- [23] B. Raubenheimer, R. T. Guza, and S. Elgar, "Wave transformation across the inner surf zone," *Journal of Geophysical Research C: Oceans*, vol. 101, no. 11, pp. 25589–25597, 1996.
- [24] M. Tissier, P. Bonneton, R. Almar, B. Castelle, N. Bonneton, and A. Nahon, "Field measurements and non-linear prediction of wave celerity in the surf zone," *European Journal of Mechanics B/Fluids*, vol. 30, no. 6, pp. 635–641, 2011.
- [25] R. Almar, P. Bonneton, H. Michallet, R. Cienfuegos, B. G. Ruessink, and M. Tissier, "On the use of the radon transform in studying wave dynamics," in *Proceedings of the 7th International Conference on Coastal Dynamics*, pp. 73–82, Arcachon, France, June 2013, <https://hal.archives-ouvertes.fr/hal-00909132>.
- [26] R. M. C. Guedes, K. R. Bryan, G. Coco, and R. A. Holman, "The effects of tides on swash statistics on an intermediate beach," *Journal of Geophysical Research: Oceans*, vol. 116, no. 4, Article ID C04008, 2011.
- [27] A. H. Sallenger and R. A. Holman, "Wave energy saturation on a natural beach of variable slope," *Journal of Geophysical Research: Oceans*, vol. 90, pp. 11939–11944, 1985.
- [28] E. B. Thornton and R. T. Guza, "Energy saturation and phase speeds measured on the natural beach," *Journal of Geophysical Research*, vol. 87, no. 12, pp. 9499–9508, 1982.
- [29] N. Sénéchal, H. Dupuis, and P. Bonneton, "Preliminary hydrodynamic results of a field experiment on a barred beach, truc vert beach on october 2001," *Ocean Dynamics*, vol. 54, no. 3-4, pp. 408–414, 2004.
- [30] P. A. Catalán and M. C. Haller, "Remote sensing of breaking wave phase speeds with application to non-linear depth inversions," *Coastal Engineering*, vol. 55, no. 1, pp. 93–111, 2008.
- [31] J. Yoo, H. M. Fritz, K. A. Haas, P. A. Work, and C. F. Barnes, "Depth inversion in the surf zone with inclusion of wave nonlinearity using video-derived celerity," *Journal of Waterway, Port, Coastal and Ocean Engineering*, vol. 137, no. 2, pp. 95–106, 2011.
- [32] R. Almar, H. Michallet, R. Cienfuegos, P. Bonneton, M. Tissier, and G. Ruessink, "On the use of the radon transform in studying nearshore wave dynamics," *Coastal Engineering*, vol. 92, pp. 24–30, 2014.
- [33] M. Tissier, R. Almar, P. Bonneton et al., "Individual wave celerity in the surf zone of a low-sloping laboratory beach," in *Proceeding of the 7th International Conference on Coastal Dynamics*, June 2013.

Research Article

GNSS-R Delay-Doppler Map Simulation Based on the 2004 Sumatra-Andaman Tsunami Event

Qingyun Yan and Weimin Huang

Faculty of Engineering and Applied Science, Memorial University, St. John's, NL, Canada A1B 3X5

Correspondence should be addressed to Weimin Huang; weimin@mun.ca

Received 20 March 2015; Revised 19 June 2015; Accepted 29 June 2015

Academic Editor: Jose C. Nieto-Borge

Copyright © 2016 Q. Yan and W. Huang. This is an open access article distributed under the Creative Commons Attribution License, which permits unrestricted use, distribution, and reproduction in any medium, provided the original work is properly cited.

A new method for simulating Global Navigation Satellite System-Reflectometry (GNSS-R) delay-Doppler maps (DDMs) of a tsunami-dominant sea surface is presented. In this method, the bistatic scattering Z-V model, the sea surface mean square slope model of Cox and Munk, and the tsunami-induced wind perturbation model are employed. The feasibility of the Cox and Munk model under a tsunami scenario is examined by comparing the Cox and Munk model based scattering coefficient with the Jason-1 measurement. A good consistency between these two results is obtained with a correlation coefficient of 0.93. After confirming the applicability of the Cox and Munk model for a tsunami-dominated sea, this study provides the simulations of the scattering coefficient distribution and the corresponding DDMs of a fixed region of interest before and during the tsunami. In the final analysis, by subtracting the simulation results that are free of tsunami from those with presence of tsunami, the tsunami-induced variations in scattering coefficients and DDMs can be clearly observed. As a result, the tsunami passage can be readily interpreted.

1. Introduction

A tsunami is a special ocean event that manifests its characteristics in terms of high propagation speed in the deep sea and extremely high wave height nearshore. It has been widely recognized that tsunamis are one of the worst natural hazards. For example, the Sumatra-Andaman tsunami that occurred in 2004 claimed many lives and caused tremendous damage to several countries [1]. Therefore, tsunami detection is especially important.

The conventional buoy measurement is a costly and inefficient method to detect tsunamis due to its high expense and low coverage [1]. The satellite altimeter may provide some direct information about the tsunami such as sea surface height (SSH) and the radar backscattering coefficient. For example, Jason-1 satellite altimeter encountered the 2004 Sumatra-Andaman tsunami on its path 109 for cycle 129, thereby offering valuable data on tsunami measurement [2]. However, only a handful of definitive SSH changes due to a tsunami event have been measured out of more than 150 documented tsunami events since the launch of the TOPEX/Poseidon satellite altimeter in 1992 [3]. This is mainly

because of the limited coverage of the satellite altimeter [2]. Recently, GNSS-R emerged as an efficient and accurate technique for ocean remote sensing due to its advantages in temporal and spatial coverage and immunity to weather effects [4]. Those benefits of the application of GNSS-R may provide a promising solution to tsunami remote sensing. Moreover, manifestations of a tsunami in the deep ocean have been investigated by a large amount of researchers, thereby laying a theoretical foundation for the GNSS-R-based deep sea tsunami detection. In 1996, tsunami-induced variations in sea surface roughness were first reported by Walker [5] and were given the name “tsunami shadow” based on observations of the darkened stripes along the tsunami front. Later, Godin [6] explained that the tsunami-induced changes in sea surface roughness are due to the tsunami-induced perturbations in sea surface wind speed. Based on these results, a theoretical model for the calculation of tsunami-induced sea surface wind velocity has been developed in [2].

In addition, recent research has made significant development on GNSS-R DDM-based sea surface wind remote sensing (e.g., [7–9]). These works have also contributed to the DDM simulation in this paper for a tsunami-dominated

sea surface, which is based upon the tsunami-perturbed sea surface wind speed. There are a few reports (e.g., [1, 10, 11]) in the literature about the GNSS-R altimetry-based tsunami detection. However, there is no publication on tsunami detection from GNSS-R DDM, to the authors' knowledge. In this paper, a process for simulating tsunami-dominant sea surface DDM is proposed. This method is based on the Zavorotny and Voronovich (Z-V) bistatic scattering model [12], the Cox and Munk sea surface mean square slope model [13], and the tsunami-induced wind speed perturbation model [2]. Followed by the introduction to this method, the feasibility of the Cox and Munk model [13] under a tsunami scenario is examined by comparing the simulated scattering coefficient with the Jason-1 measurement. After verifying its applicability, the tsunami DDM simulation can be achieved through inputting the background wind speed over the sea surface and the tsunami-induced sea surface change. In this work, the simulation results before and during a tsunami over a region of interest are presented. Through analysis, the passage of the tsunami over this region can be interpreted based on the observation of tsunami-induced variations in scattering coefficient and DDMs. This work may provide some new support for the GNSS-R DDM-based tsunami detection in the future.

The remainder of this paper is organized as follows. The procedures of tsunami-dominant sea surface DDM simulation are described in Section 2. The verification of the Cox and Munk model under a tsunami scenario followed by the simulation results is presented in Section 3. Conclusions are presented in Section 4.

2. Model Implementation and Simulation Process

The Cox and Munk model [13] and the Z-V model [12] have already been successfully applied to the GNSS-R DDM-based sea surface wind sensing (e.g., [7, 14]). The Z-V model depicts the scattered GPS signal power as a function of time delay and Doppler frequency shift, the transmitter elevation angle, and the receiver height as well as the surface scattering coefficient (σ^0). The Cox and Munk model substantiates an empirical relationship between the wind speed at the height of 10 m above the sea surface (U_{10}) and the sea surface mean square slope (MSS). Consequently, the sea surface scattering coefficient is determined by MSS [7]. In summary, with knowledge of U_{10} the corresponding DDM can be simulated by combining the Cox and Munk model and the Z-V model. With this in mind, the associated DDM simulation can be completed if the distribution of U_{10} over a tsunami-dominant sea surface is available.

The Z-V model [12] can be described as follows:

$$\begin{aligned} & \langle |Y(\tau, f_D)|^2 \rangle \\ &= T_i^2 \iint_A \frac{D^2(\vec{\rho}) \sigma^0(\vec{\rho}) \Lambda^2(\tau) |S(f_D)|^2}{4\pi R_R^2(\vec{\rho}) R_T^2(\vec{\rho})} d^2\rho, \end{aligned} \quad (1)$$

where τ is the time delay between the received signal and the local code replica, $\Lambda(\tau) = 1 - |\tau/\tau_c|$, when $-\tau_c \leq \tau \leq \tau_c$;

$\Lambda = 0$; otherwise τ_c is the length of one code chip. Consider $S(f_D) = \sin(\pi T_i f_D)/(\pi T_i f_D)$, T_i is the coherent integration time, $\vec{\rho}$ is the displacement vector of a surface point from the specular point (SP), D is the antenna radiation pattern, R_T and R_R are the distances from a point on the ocean surface to the GNSS-R transmitter and receiver, A represents the effective scattering surface area (glistening zone), and σ^0 is the surface scattering coefficient.

With the exception of σ^0 , the rest of the terms in (1) are usually known for a specific GNSS system and its geometry. Therefore, we mainly consider the scattering coefficient σ^0 , which may be written as [7]

$$\sigma^0(\vec{\rho}) = \pi |\mathfrak{R}|^2 P\left(-\frac{q_\perp}{q_z}\right) \left(\frac{q}{q_z}\right)^4, \quad (2)$$

where $|\mathfrak{R}|^2$ is the Fresnel reflection coefficient that depends on the local elevation angle, polarization, and the complex dielectric constant of sea water [7]; the scattering vector \vec{q} can be obtained with the locations of the transmitter, receiver, and corresponding surface point; $-q_\perp/q_z$ is the ocean surface slope, denoted hereafter as s . $P(s)$ is the slope Probability Density Function (PDF) of the ocean surface gravity wave which is believed to be subject to Gaussian distribution with wind-dependent upwind variance σ_u^2 and crosswind variance σ_c^2 [15]. It is worth mentioning that tsunami waves are gravity waves. $P(s)$ is expressed as [7]

$$\begin{aligned} P(s) &= \frac{1}{2\pi \sqrt{\det(W)}} \exp\left[-\frac{1}{2} \begin{pmatrix} s_x \\ s_y \end{pmatrix}^T W^{-1} \begin{pmatrix} s_x \\ s_y \end{pmatrix}\right], \\ W &= \begin{bmatrix} \cos \phi_0 & -\sin \phi_0 \\ \sin \phi_0 & \cos \phi_0 \end{bmatrix} \times \begin{bmatrix} \sigma_u^2 & 0 \\ 0 & \sigma_c^2 \end{bmatrix} \\ &\times \begin{bmatrix} \cos \phi_0 & \sin \phi_0 \\ -\sin \phi_0 & \cos \phi_0 \end{bmatrix}, \end{aligned} \quad (3)$$

where ϕ_0 is the angle between the up-down wind direction and the x -axis. Subsequently, the clean sea surface mean square slope model of Cox and Munk [13] is introduced to link the wind speed and wind direction to the upwind and crosswind variances, as

$$\begin{aligned} \sigma_u^2 &= 0.45 \times (3.16 \times 10^{-3} f(U_{10})), \\ \sigma_c^2 &= 0.45 \times (0.003 + 1.92 \times 10^{-3} U_{10}), \end{aligned} \quad (4)$$

where

$$f(U_{10}) = \begin{cases} U_{10} & U_{10} \leq 3.49 \\ 6 \cdot \ln(U_{10}) - 4 & 3.49 < U_{10} \leq 46 \\ 0.411 \cdot U_{10} & U_{10} > 46. \end{cases} \quad (5)$$

Following similar steps as presented in [7, 14], the DDMs can be readily simulated with the knowledge of U_{10} , based on the Cox and Munk model [13] and the Z-V model [12] for a tsunami-free sea surface.

For a tsunami-dominant sea surface, the effective wind speed can be derived from the tsunami-induced wind speed perturbation model [2], that is, the so-called Godin model. This model was proposed based on the observation data of “tsunami shadow” from the October 4, 1994, Hokkaido tsunami [5]. The theoretical derivation of this model and its validation based on simulation were presented in [2]. Moreover, this model has been successfully applied in the simulation of radar backscattering strength over a tsunami region (e.g., [2, 3]). The tsunami-induced variations in radar backscattering strength estimated based on the Godin model were consistent with the Jason-1 measurement [2]. Thus, the Godin model is employed here to determine the effective wind speed during a tsunami period. This model shows that the effective wind speed during a tsunami event depends on tsunami parameters and differs from the background wind speed by a factor of M [2], and

$$M = 1 - \frac{\kappa a c}{H u_* \ln \beta}, \quad (6)$$

where $\kappa = 0.4$, $u_* = 0.04U_{10}$, H is the height of the background logarithmic boundary layer, a is the sea surface height change due to tsunami, $c = \sqrt{gD}$ is the tsunami phase speed, where g is the acceleration due to gravity, D is the depth of sea, and

$$\beta = \frac{\kappa u_* T_0}{2\pi z_0}, \quad (7)$$

where $z_0 = 0.01u_*^2/g$ represents the roughness length and T_0 is tsunami period.

By employing these models, the tsunami DDMs can be simulated with different tsunami parameters and background wind speed.

3. Simulation Results

In this section, feasibility of the Cox and Munk model under a tsunami scenario is tested first. Then, the parameters associated with tsunami DDM simulation are set. After that, the tsunami DDM simulation results are presented.

3.1. Feasibility of the Cox and Munk Model under a Tsunami Scenario. The Jason-1 satellite altimeter encountered the tsunami on the morning of December 26, 2004 [2] (shown in Figure 1). It recorded radar backscattering coefficient and sea surface wind speed, thereby offering an opportunity to study the wind speed and σ^0 during the tsunami event. Before exerting the tsunami DDM simulation, the feasibility of the Cox and Munk model under a tsunami event should be examined. By employing the Cox and Munk model, the σ^0 of a tsunami-dominant sea surface can be simulated with the knowledge of U_{10} over the corresponding region. Based on this, a comparison between the Jason-1 measured σ^0 and the simulated σ^0 can be made.

Figure 2(a) illustrates the Jason-1 measured sea surface wind speeds (solid line) over the range of (6.00°S, 83.60°E) to (4.99°N, 87.54°E) with the presence of the tsunami leading

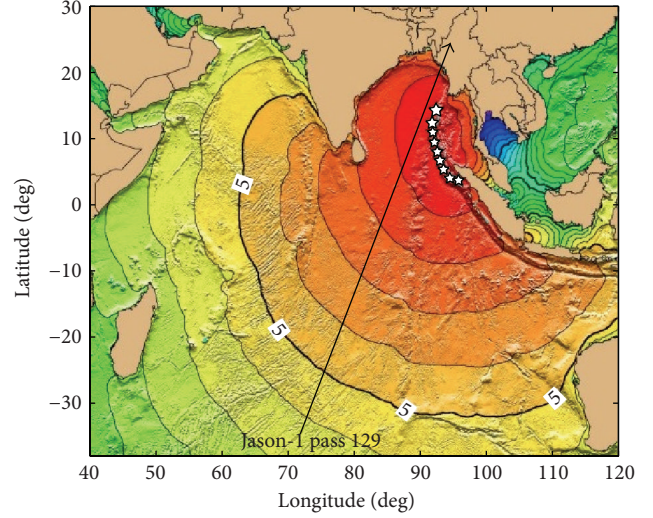


FIGURE 1: Jason-1 satellite altimeter ground track during the 2004 Sumatra-Andaman tsunami. Black line indicates the Jason-1 ground track with a direction in accordance with the arrow. White stars represent the epicentre. Contours of the tsunami leading front are also shown with hourly intervals. This graphic is modified from the work of the National Geophysical Data Center/NOAA, at http://www.ngdc.noaa.gov/hazard/img/2004_1226.jpg.

wave front. For the simulation, some assumptions are made below:

- (1) The GNSS-R transmitter, receiver, and the SP are set on the same line that is also perpendicular to the sea surface.
- (2) The SP follows the Jason-1 ground track.
- (3) The Jason-1 measured U_{10} is uniform along tsunami wave front.

The first assumption is required to simulate the Jason-1 backscattering scenario. The second assumes that the GNSS-R system and Jason-1 monitored this region at the same time. The last one aims at forming a two-dimensional wind speed distribution over the glistening zone.

The size of GNSS-R glistening zone is about 200 km by 200 km. Through inputting the wind speeds that are interpolated using the Jason-1 measured U_{10} over sea surface, the scattering coefficient can therefore be simulated. Here, only the σ^0 at SP which follows the Jason-1 ground track is recorded and compared with the Jason-1 measurements. Figure 2(b) shows the σ^0 measured by Jason-1 and the σ^0 simulated by the Cox and Munk model. A good consistency between the measured σ^0 and the simulated σ^0 can be observed with a correlation coefficient of 0.93. In Figure 2(b), the simulated scattering coefficients for GNSS-R seem to be slightly overestimated compared to the measurement by Jason-1. This is mainly due to the difference in the operating frequencies of GNSS-R (1.5 GHz, i.e., L-band) and Jason-1 (5.4 GHz, i.e., C-band). The average difference of the scattering coefficient is about 1.33 dB and this is consistent with the analysis in [16], where the difference of σ^0 between

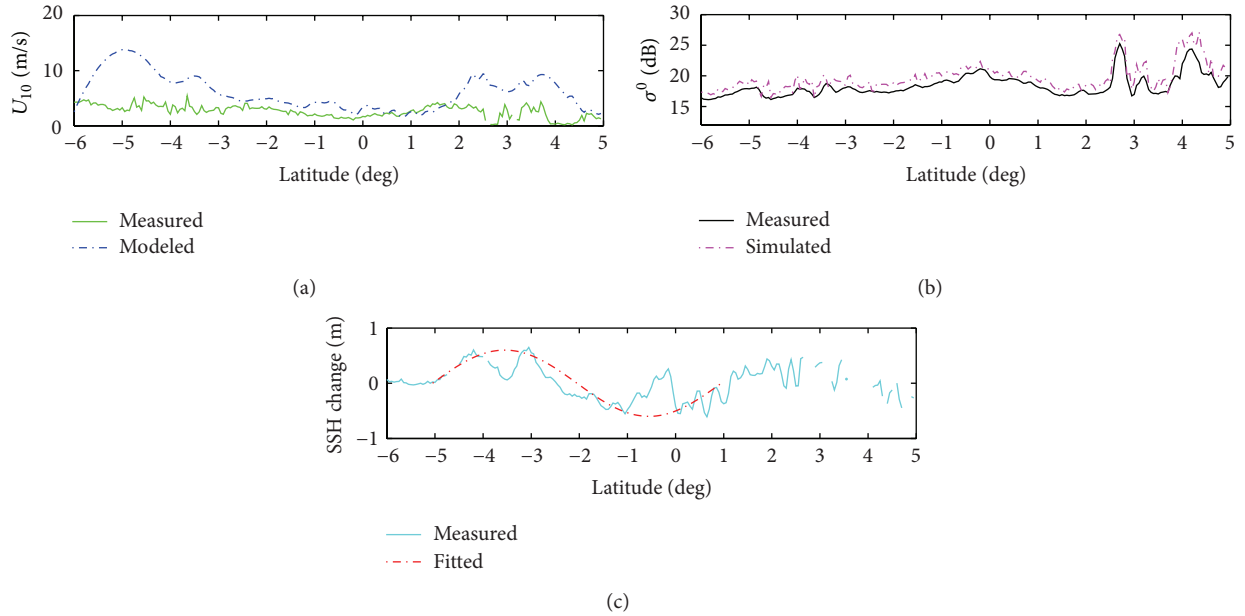


FIGURE 2: Jason-1 measurement for pass 129 from (6.00°S, 83.60°E) to (4.99°N, 87.54°E) obtained during the 2004 tsunami: (a) sea surface U_{10} , (b) backscattering coefficient σ^0 , and (c) SSH change due to a tsunami. Gaps in the curves are caused by deficiency of measured data.

L- and C-band measurements is found to be about 2 dB. Therefore, the feasibility of the Cox and Munk model on the tsunami DDM simulation is confirmed.

3.2. Simulation Scenario Parameters. Based on the analysis above, it can be concluded that the σ^0 of a tsunami-dominant sea surface can be simulated via the Cox and Munk model [13]. Thus, the tsunami DDMs can be simulated through the Z-V model [12], the Cox and Munk model [13], and the tsunami-induced wind speed perturbation model [2] with reliability.

Here, to facilitate the simulation, the typical empirical values are adopted in alignment with those in [2]; that is, $T_0 = 40$ min, $D = 4000$ m, and $H = 60$ m. If the SSH change a due to tsunami and the background wind speed are known, the effective wind speed over a tsunami surface can therefore be determined by implementing the tsunami-induced wind speed perturbation model [2].

The SSH measured by Jason-1 on cycle 109 during the tsunami event is subtracted by the average SSH observed over the exactly same ground track on cycles 108 and 110, and the difference is regarded as tsunami-induced SSH change a (shown in Figure 2(c)). This process is in accord with [17]. Besides, it has been reported in [17] that the tsunami-induced SSH change a over the range from (5.00°S, 83.96°E) to (1.00°N, 86.12°E) can be well fitted by a sine wave with a wavelength of 580 km and an amplitude of 60 cm, as shown by a dash line in Figure 2(c). Alternatively, the sine model is treated as another form of input a for reference. In addition, a is assumed to distribute uniformly along the contours of the tsunami leading wave front, which are concentric circles with a center at the epicenter (3.4°N, 94.2°E).

The U_{10} over the region under investigation measured by QuikSCAT on its orbit 28744 is considered to be the

background wind speed. The data was recorded around 45 min before the earthquake appeared, which means this measurement is totally free of the tsunami influence. Therefore, it is reasonable to use the QuikSCAT measurement as the background U_{10} . The effective U_{10} is calculated using only the QuikSCAT measurement over the Jason-1 ground track and is shown in Figure 2(a). Difference between the modelled and measured wind speeds can be seen in Figure 2(a). This is because the modelled wind speed significantly relies on the background wind speed (i.e., before the appearance of tsunami). The only available background wind speed data of the region under investigation, immediately before the tsunami, was measured by QuikSCAT. However, the data was collected 45 min before the earthquake happened. Moreover, Jason-1 flew over the same region 115 min after the earthquake appeared. Thus, a time gap of 160 min exists between the measured and the modelled wind speeds. As we know, wind speed may change significantly after two hours. This may explain the difference between the modelled and measured wind speeds.

The parameters mentioned above are tabulated in Table 1. In terms of GNSS-R simulation scenario, the parameters are kept the same as those in [18], also shown in Table 1.

In order to manifest a unique influence of the tsunami on GNSS-R sea surface remote sensing in this work, a continuous detection over a fixed region is assumed. To achieve this, both the transmitter and the receiver are set fixed over time. In this fashion, the variations caused by the geometry change of GNSS-R system will be eliminated as well, which allows a more direct observation of tsunami effect. The region of our interest is set around (6.0081°S, 83.6019°E) with a size of 200 km by 200 km. The first simulation result was conducted for 02:55:22 UT. The study region at this time was tsunami-free. Therefore, this first simulation result is considered as

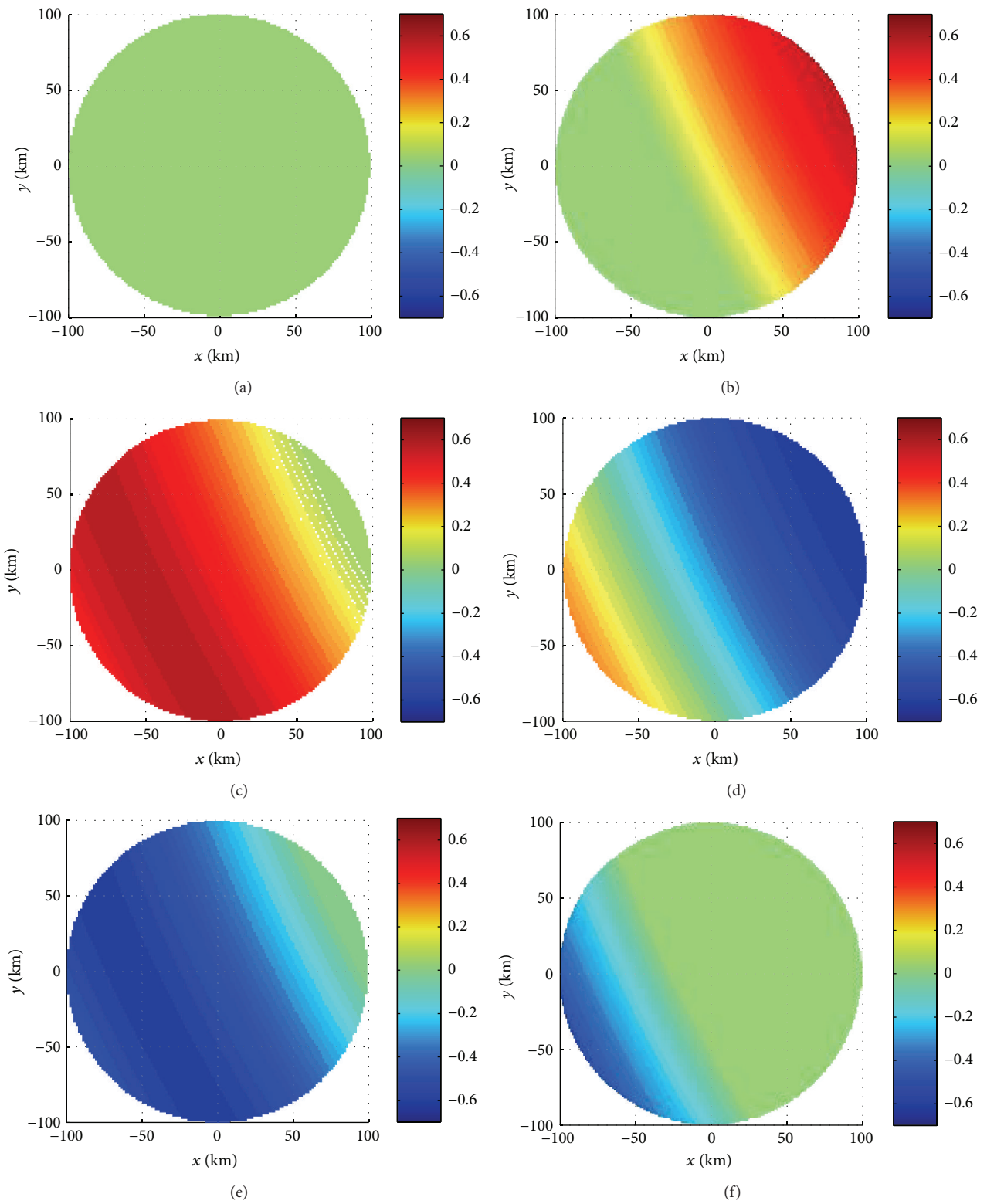


FIGURE 3: Spatial distribution of tsunami-induced SSH change based on a sine wave model: (a) before tsunami and with (b) a part of tsunami leading front, (c) the tsunami crest, (d) a part between the crest and trough, (e) the tsunami trough, and (f) the tail of tsunami leading front.

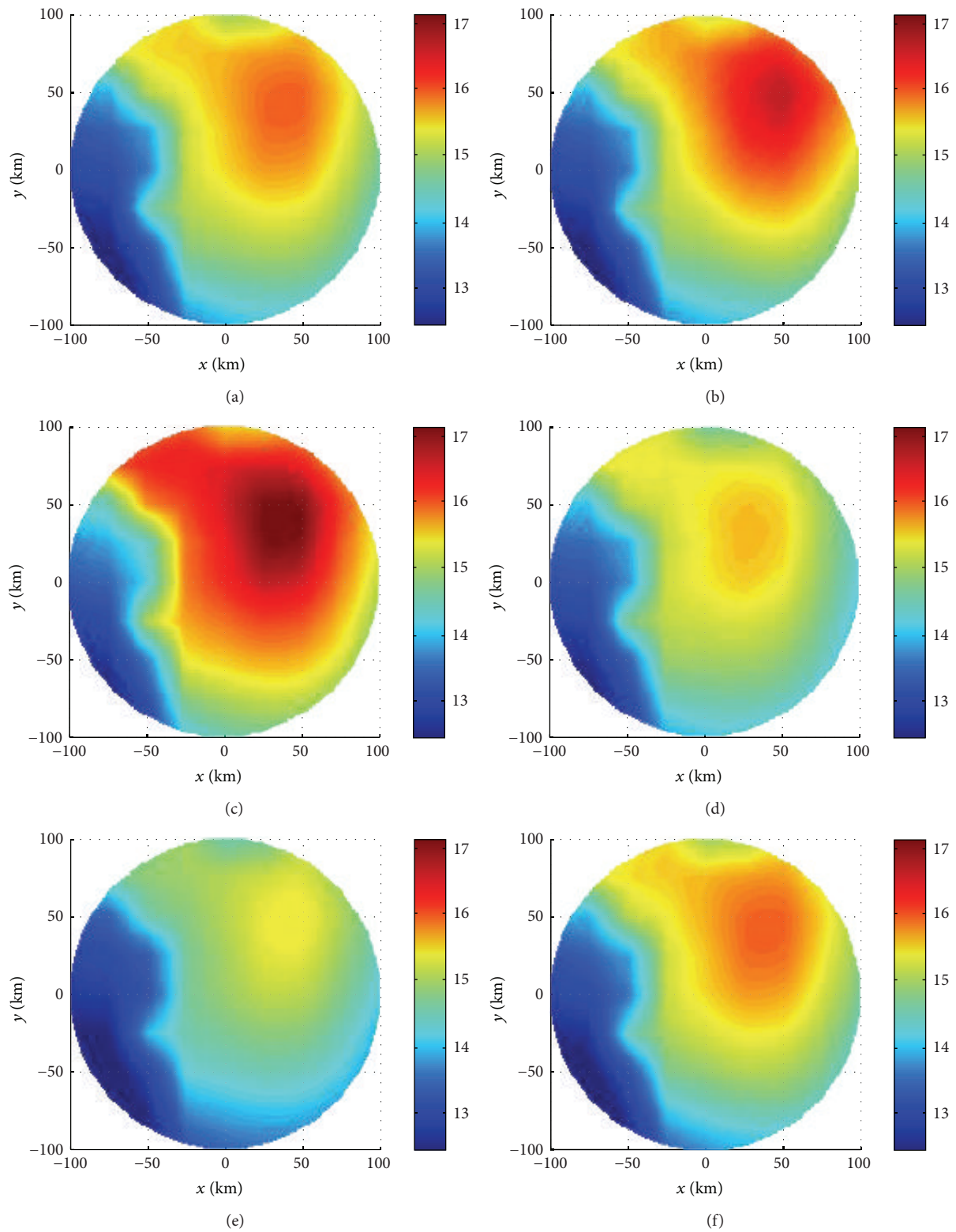


FIGURE 4: Simulated σ^0 using fitted sine wave as input: (a) without tsunami and with (b) a part of tsunami leading front; (c) the tsunami crest; (d) a part between the crest and trough; (e) the tsunami trough; and (f) the tail of tsunami leading front.

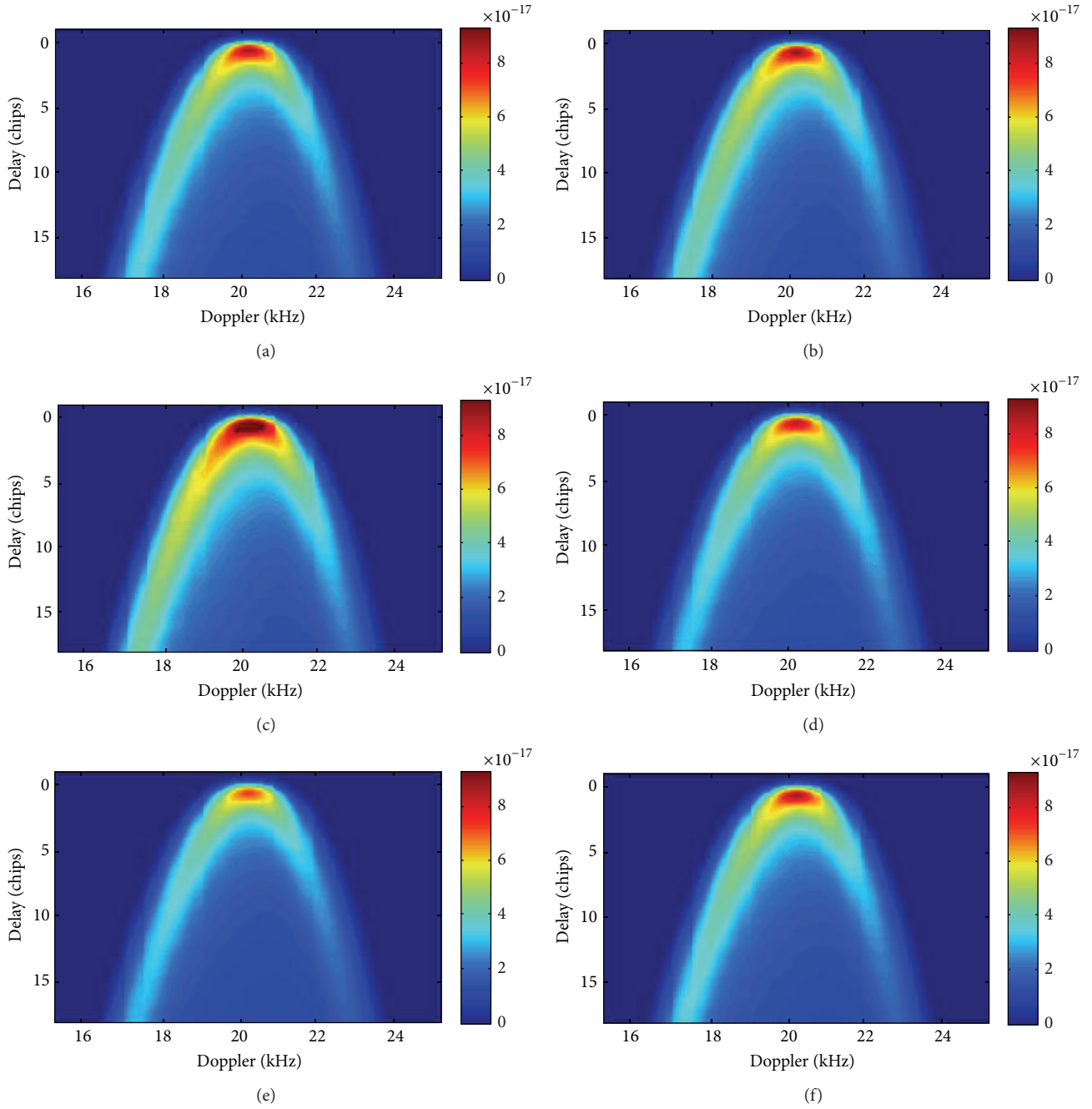


FIGURE 5: Corresponding DDMs resulting from σ^0 in Figure 4.

the initial baseline for the following results. Meanwhile, the SSH change in Figure 2(c) is regarded as initial distribution. The initial simulation only depends on the background U_{10} over this region measured by QuikSCAT. However, within a few minutes, this region experienced a tsunami passage. The tsunami-induced wind speed perturbation model must be employed with the tsunami entering into this region. The effective U_{10} will be calculated based on this model with the knowledge of background U_{10} and a .

As we have assumed $D = 4000$ m, the tsunami propagation speed can thus be approximated by 200 m/s. Meanwhile,

the initial distribution of a over space is known. For this reason, the a over this region at each moment can be easily deduced according to the distance and tsunami propagation speed. Then, the effective U_{10} at different time can also be determined.

3.3. Results. The spatial distribution of tsunami-induced SSH change based on a sine wave model is shown in Figure 3.

Figure 4 displays the simulated σ^0 by adopting the fitted sine wave model as input a . The time gaps between the initial detection in Figure 4(a) and those from Figures

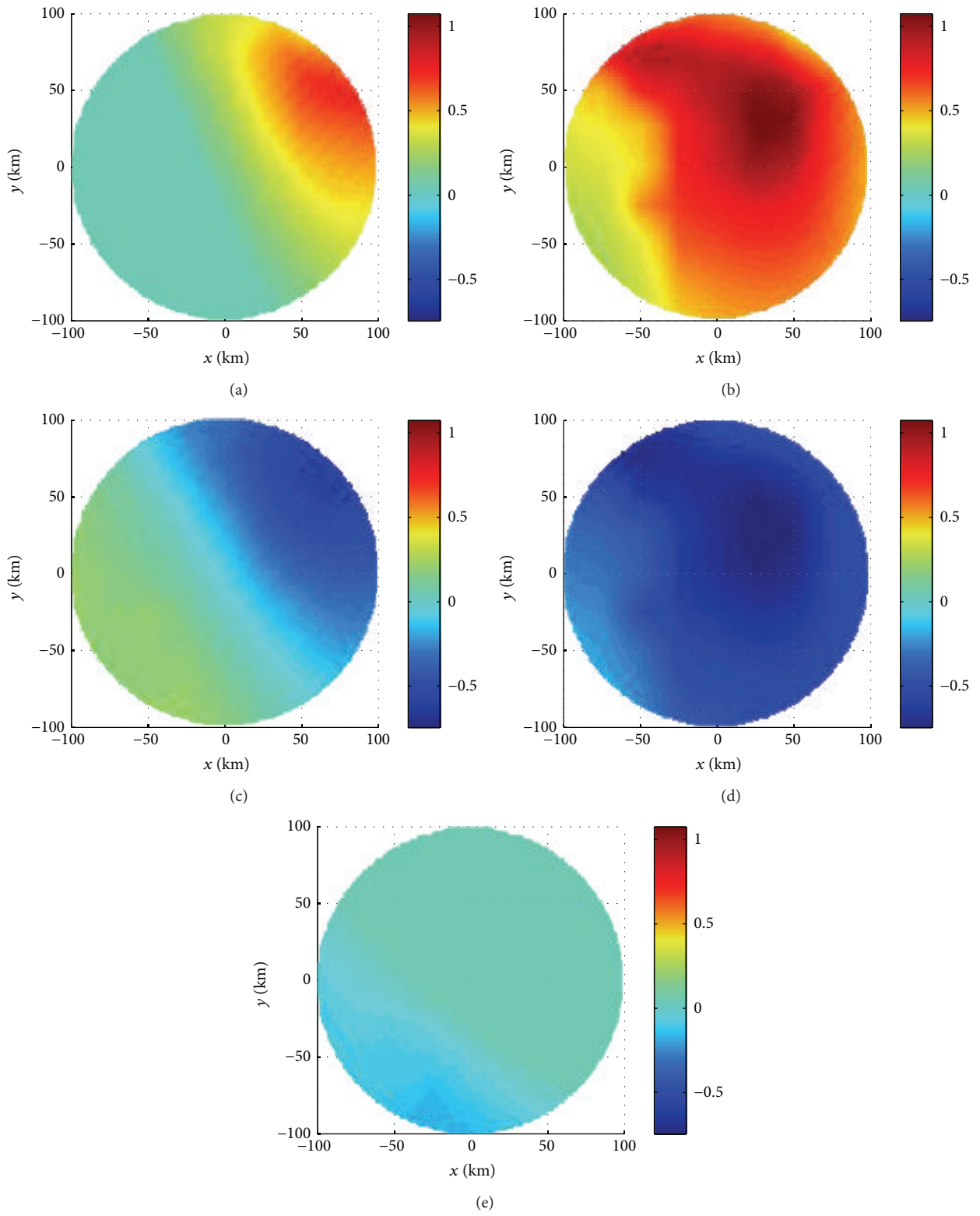


FIGURE 6: Differences of the scattering coefficients of tsunami-dominated and tsunami-free sea surfaces (based on sine wave-modelled SSH changes).

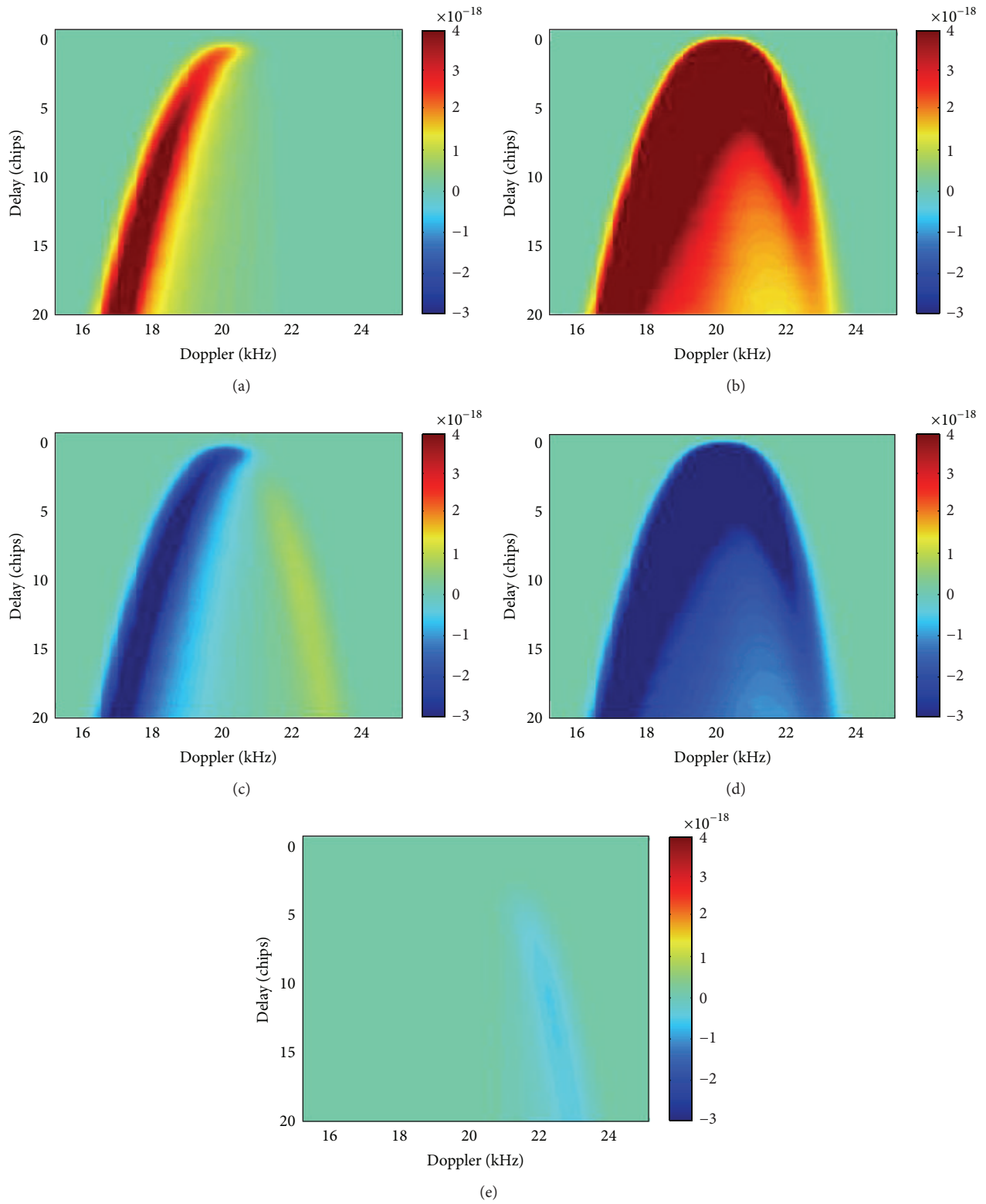


FIGURE 7: Differences of the DDMs of tsunami-dominated and tsunami-free sea surfaces (based on sine wave-modelled SSH changes).

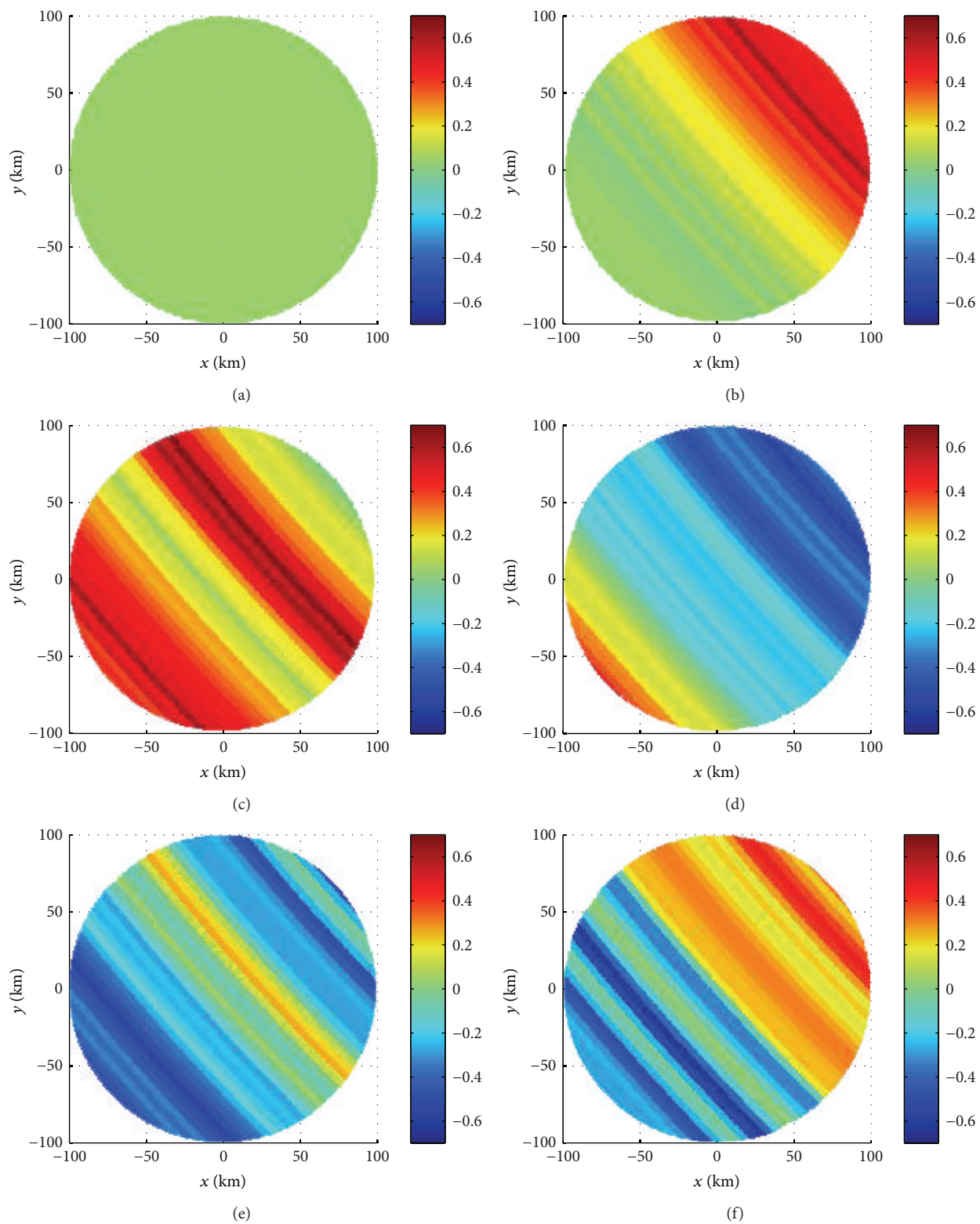


FIGURE 8: Spatial distribution of tsunami-induced SSH change based on Jason-1 measurements.

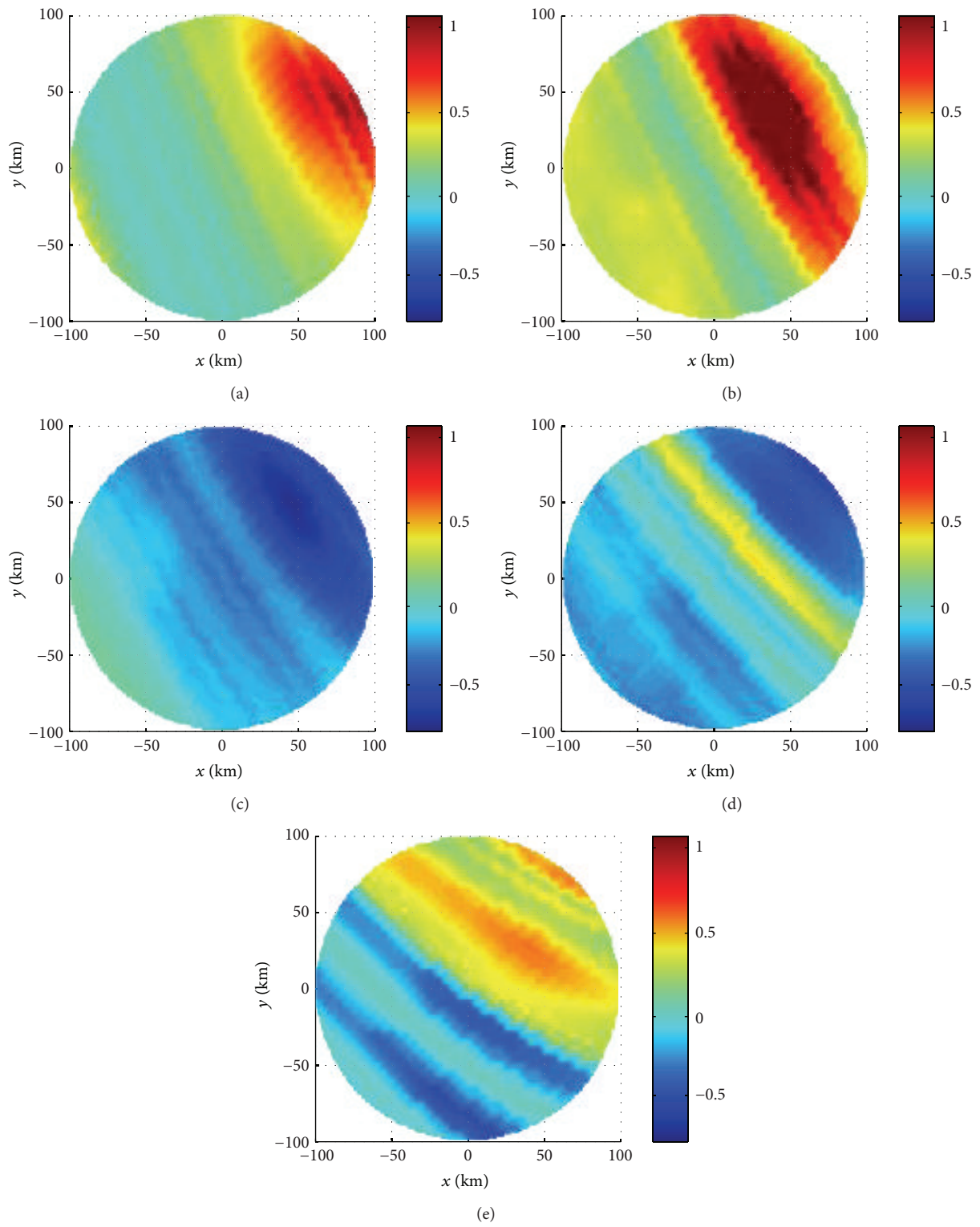


FIGURE 9: Differences of the scattering coefficients of tsunami-dominated and tsunami-free sea surfaces (based on Jason-1 measured SSH changes).

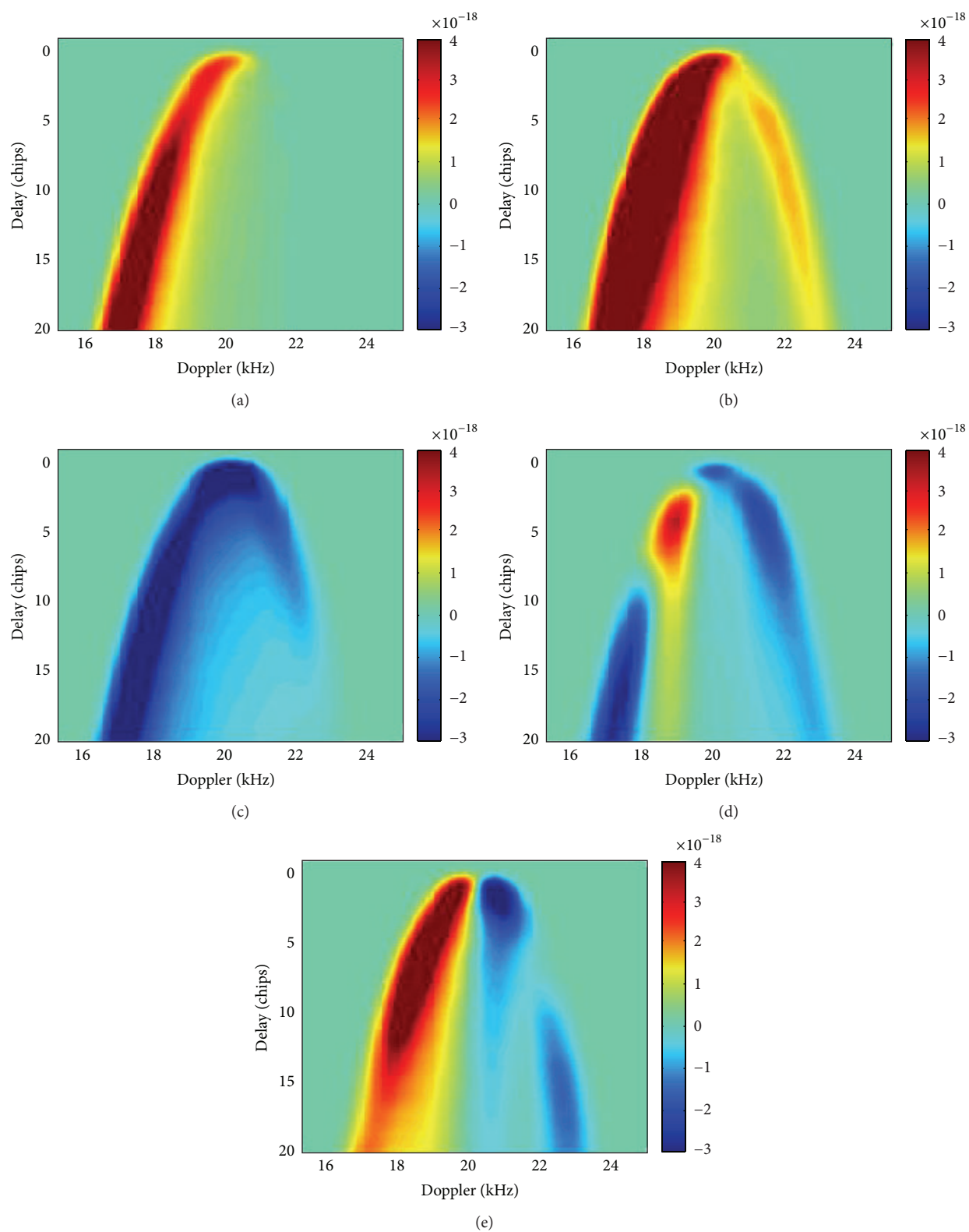


FIGURE 10: Differences of the DDMs of tsunami-dominated and tsunami-free sea surfaces (based on Jason-1 measured SSH changes).

TABLE 1: Tsunami DDM simulation setting up.

Simulation parameters	Value (data source)
Tsunami period (T_0)	40 min
Depth of ocean (D)	4000 m
Height of the background logarithmic boundary layer (H)	60 m
SSH change (a)	Jason-1 measurement/fitted sine wave model
Background wind speed	QuikSCAT measurement on orbit 28744
Receiver height	680 km
Transmitter velocity	(-2.72, 2.68, -.65) km/s
Receiver velocity	(7.21, 1.23, 1.72) km/s
SP position	(6.0081°S, 83.6019°E)

4(b) to 4(f) are 9.17 min, 22.92 min, 36.67 min, 50.42 min, and 64.17 min, respectively. Figure 5 shows the simulated DDMs corresponding to the scattering coefficient maps in Figure 4. In order to manifest the tsunami-induced variations in σ^0 and DDMs, the simulation results with tsunami are subtracted by the initial result that contains no tsunami; that is, subplots (b)–(f) in both Figures 4 and 5 are subtracted by the corresponding subplot (a). The resultant scattering coefficient and DDM differences are displayed in Figures 6 and 7, respectively. Although the overall shapes in each subplot of Figure 4 or Figure 5 are similar, variations still can be observed. From Figure 6, the σ^0 variations caused by the tsunami are found to be about ± 1 dB. This result is consistent with the analysis in [2].

Intuitively, an increase in a will lead to a reduction in M factor according to (6). On the other hand, a decrease in U_{10} will contribute to an increase in σ^0 . On the whole, the variations in σ^0 are coincident with the changes of a . Therefore, the passage of the tsunami can be identified from Figure 6: (a) the leading front appears first; (b) then comes the crest; (c) the transition region between the crest and the trough approaches later; (d) after that, the trough emerges; and (e) finally, the tsunami wave propagates out of this region with only a small portion of the tail remaining. The variations in σ^0 are approximately proportional to the tsunami-induced SSH changes. The tsunami-induced variations in DDMs can be observed in Figure 7.

The spatial distribution of tsunami-induced SSH change based on Jason-1 measurements is shown in Figure 8. Since the variations due to tsunami are not so obvious in simulated scattering coefficient maps and DDMs, only the differences between the results with and without tsunami are displayed in Figures 9–10. Due to the non-ideal-sine distribution of measured a , these simulation results differ slightly from those based on fitted sine wave input a . However, with a close observation of Figure 9, the variations in σ^0 are also consistent with the distribution of measured a .

4. Conclusion

In this work, a process is proposed to simulate the DDM of a tsunami-dominant sea surface. The Z-V model, the

Cox and Munk model, and the tsunami-induced wind speed perturbation model are employed in this method. The feasibility of Cox and Munk model under the tsunami scenario is confirmed (a correlation coefficient of 0.93 between the simulated and measured σ^0 is observed). After verifying the applicability of the Cox and Munk model for a tsunami-dominated sea, σ^0 and DDMs are simulated with two different tsunami-induced SSH change inputs, that is, Jason-1 measurement and fitted sine wave model. The σ^0 variations caused by the tsunami are found to be about ± 1 dB, which is consistent with the result in [2]. Finally, by studying the tsunami-induced variations in σ^0 , the passage of tsunami can be identified. In the future, tsunami parameters may be retrieved from the simulated DDMs of tsunami-dominant sea surface. It is also necessary to further validate the proposed method using collected GNSS-R data and corresponding measured background and effective wind speed dataset during a tsunami event. However, this study is not possible today as the available data for this research is limited. This may become possible with the launch of new spaceborne GNSS-R missions, for example, TechDemoSat-1 and Cyclone GNSS (CYGNSS) [19].

Conflict of Interests

The authors declare that there is no conflict of interests regarding the publication of this paper.

Acknowledgments

This work was supported by the Natural Sciences and Engineering Research Council of Canada Discovery Grant (NSERC 402313-2012) to Dr. Weimin Huang. The authors would like to thank C. Arbour for her editorial help on this paper.

References

- [1] K. Yu, "Tsunami-wave parameter estimation using GNSS-based sea surface height measurement," *IEEE Transactions on Geoscience and Remote Sensing*, vol. 53, no. 5, pp. 2603–2611, 2015.
- [2] O. A. Godin, V. G. Irisov, R. R. Leben, B. D. Hamlington, and G. A. Wick, "Variations in sea surface roughness induced by the 2004 Sumatra-Andaman tsunami," *Natural Hazards and Earth System Science*, vol. 9, no. 4, pp. 1135–1147, 2009.
- [3] B. D. Hamlington, R. R. Leben, O. A. Godin, and V. G. Irisov, "On the feasibility of tsunami detection using satellite-based sea surface roughness measurements," in *Proceedings of the 30th IEEE International Geoscience and Remote Sensing Symposium (IGARSS '10)*, pp. 3035–3038, Honolulu, Hawaii, USA, July 2010.
- [4] S. Jin, G. P. Feng, and S. Gleason, "Remote sensing using GNSS signals: current status and future directions," *Advances in Space Research*, vol. 47, no. 10, pp. 1645–1653, 2011.
- [5] D. A. Walker, "Observations of tsunami 'shadows': a new technique for assessing tsunami wave heights?" *Science of Tsunami Hazards*, no. 14, pp. 3–11, 1996.
- [6] O. A. Godin, "Air-sea interaction and feasibility of tsunami detection in the open ocean," *Journal of Geophysical Research C: Oceans*, vol. 109, no. 5, Article ID C05002, pp. 1–20, 2004.

- [7] C. Li and W. Huang, "An algorithm for sea-surface wind field retrieval from GNSS-R delay-doppler map," *IEEE Geoscience and Remote Sensing Letters*, vol. 11, no. 12, pp. 2110–2114, 2014.
- [8] N. Rodriguez-Alvarez, D. M. Akos, V. U. Zavorotny, J. A. Smith, A. Camps, and C. W. Fairall, "Airborne GNSS-R wind retrievals using delay-doppler maps," *IEEE Transactions on Geoscience and Remote Sensing*, vol. 51, no. 1, pp. 626–641, 2013.
- [9] E. Valencia, V. U. Zavorotny, D. M. Akos, and A. Camps, "Using DDM asymmetry metrics for wind direction retrieval from GPS ocean-scattered signals in airborne experiments," *IEEE Transactions on Geoscience and Remote Sensing*, vol. 52, no. 7, pp. 3924–3936, 2014.
- [10] M. Martin-Neira, C. Buck, S. Gleason et al., "Tsunami detection using the PARIS concept," in *Proceedings of the Progress in Electromagnetics Research Symposium*, Hangzhou, China, August 2005.
- [11] R. Stosius, G. Beyerle, A. Hoehner, J. Wickert, and J. Lauterjung, "The impact on tsunami detection from space using GNSS-reflectometry when combining GPS with GLONASS and Galileo," *Advances in Space Research*, vol. 47, no. 5, pp. 843–853, 2011.
- [12] V. U. Zavorotny and A. G. Voronovich, "Scattering of GPS signals from the ocean with wind remote sensing application," *IEEE Transactions on Geoscience and Remote Sensing*, vol. 38, no. 2, pp. 951–964, 2000.
- [13] C. Cox and W. Munk, "Measurement of the roughness of the sea surface from photographs of the sun's glitter," *Journal of the Optical Society of America*, vol. 44, no. 11, pp. 838–850, 1954.
- [14] M. P. Clarizia, C. P. Gommenginger, S. T. Gleason, M. A. Srokosz, C. Galdi, and M. Di Bisceglie, "Analysis of GNSS-R delay-Doppler maps from the UK-DMC satellite over the ocean," *Geophysical Research Letters*, vol. 36, no. 2, Article ID L02608, 5 pages, 2009.
- [15] S. Gleason and D. Gebre-Egziabher, "Remote sensing using bistatic GNSS reflections," in *GNSS Applications and Methods*, chapter 16, Artech House, 2009.
- [16] A. Awada, A. Khenchaf, and A. Coatanhay, "Frequency impact on the bistatic radar scattering from an ocean surface," in *Proceedings of the IEEE International Geoscience and Remote Sensing Symposium (IGARSS '07)*, pp. 4459–4462, Barcelona, Spain, June 2007.
- [17] J. Gower, "The 26 December 2004 tsunami measured by satellite altimetry," *International Journal of Remote Sensing*, vol. 28, no. 13-14, pp. 2897–2913, 2007.
- [18] C. Li, W. Huang, and S. Gleason, "Dual antenna space-based GNSS-R ocean surface mapping: oil slick and tropical cyclone sensing," *IEEE Journal of Selected Topics in Applied Earth Observations and Remote Sensing*, vol. 8, no. 1, pp. 425–435, 2015.
- [19] C. Ruf, M. Unwin, J. Dickinson et al., "CYGNSS: enabling the future of hurricane prediction [remote sensing satellites]," *IEEE Geoscience and Remote Sensing Magazine*, vol. 1, no. 2, pp. 52–67, 2013.

Research Article

Wave Height Estimation from Shipborne X-Band Nautical Radar Images

Xinlong Liu, Weimin Huang, and Eric W. Gill

Faculty of Engineering and Applied Science, Memorial University of Newfoundland, St. Johns, NL, Canada A1B 3X5

Correspondence should be addressed to Weimin Huang; weimin@mun.ca

Received 30 March 2015; Revised 3 July 2015; Accepted 12 July 2015

Academic Editor: Francesco Serafino

Copyright © 2016 Xinlong Liu et al. This is an open access article distributed under the Creative Commons Attribution License, which permits unrestricted use, distribution, and reproduction in any medium, provided the original work is properly cited.

A shadowing-analysis-based algorithm is modified to estimate significant wave height from shipborne X-band nautical radar images. Shadowed areas are first extracted from the image through edge detection. Smith's function fit is then applied to illumination ratios to derive the root mean square (RMS) surface slope. From the RMS surface slope and the mean wave period, the significant wave height is estimated. A data quality control process is implemented to exclude rain-contaminated and low-backscatter images. A smoothing scheme is applied to the gray scale intensity histogram of edge pixels to improve the accuracy of the shadow threshold determination. Rather than a single full shadow image, a time sequence of shadow image subareas surrounding the upwind direction is used to calculate the average RMS surface slope. It has been found that the wave height retrieved from the modified algorithm is underestimated under rain and storm conditions and overestimated for cases with low wind speed. The modified method produces promising results by comparing radar-derived wave heights with buoy data, and the RMS difference is found to be 0.59 m.

1. Introduction

Marine radars can image both temporal and spatial variations of the sea surface while buoys provide only temporal point measurements. The radar signature of the sea surface, also known as sea clutter, is undesirable and generally suppressed in navigation purposes, but it is useful in monitoring the sea state [1]. The clutter is, in general, generated by the Bragg scattering of the near-grazing incidence radar signal with short wind-induced sea surface ripples. Longer waves become visible in radar images due to their modulations of the short ripples, mainly via hydrodynamic modulation, tilt modulation, and shadowing [2]. Thus, analysis of time series of X-band nautical radar sea surface images allows the estimation of directional wave spectra and integrated sea state parameters [3–5]. Algorithms for such purposes have been largely developed during the last several decades.

A widely accepted method of wave height estimation for X-band radar is based on the signal-to-noise ratio (SNR) derived from the image spectrum [5–7]. Another class of algorithms is based on the statistics of radar sea surface images. Through a constant threshold probability of illumination P_0 based on the theory of geometric optics [8], a

model relating the significant wave height to the island-to-trough ratio extracted from the image was established in [9]. In [10], an algorithm based on [9], but with a varying P_0 , was proposed to enhance the wave height determination. In [11, 12], wave height was derived by analyzing the texture of X-band radar sea surface images. Other techniques, including an iterative least square approach [13] and a wavelet-based algorithm [14], have been similarly developed. In all cases, the algorithmic outputs require calibration by additional reference sensors such as wave buoys.

Recently, a shadowing-analysis-based wave height algorithm has been proposed [15]. Assuming a geometric shadowing condition, shadowed areas are first extracted from the image by edge detection. Then, using the calculated illumination ratios in local areas, the RMS surface slope is derived by curve-fitting Smith's function [16]. Finally, the significant wave height is estimated from the RMS surface slope and the average zero-crossing wave period. Unlike earlier approaches, this algorithm does not require calibrations using additional reference sensors. Therefore, it shows promise for improving the ease of implementation and reducing operational cost. Here, such a method is modified and applied to data acquired from a radar on a moving ship.

This paper proceeds as follows. In Section 2, the shadowing-analysis-based wave height algorithm is briefly reviewed and the proposed modifications are described. Section 3 contains experimental results obtained from shipborne radar data using both the original and modified algorithms, as well as the comparison with buoy data. Finally, a conclusion and future directions for this work appear in Section 4.

2. Method

2.1. The Shadowing-Analysis-Based Wave Algorithm. The algorithm was introduced in detail in [15]. It contains the following major steps.

2.1.1. Estimating Shadow Threshold. The edges in the image that separate shadowed areas from illuminated areas are identified using an edge detection technique. Here, this involves the convolution of a raw radar image $I(r, \theta)$ with a simple pixel difference operator $H_i(r, \theta)$ for each of $i = 1, 2, \dots, 8$ directions, and r and θ are range and azimuth, respectively. In [17], this convolution results in i edge-detected images ($I_{Ei}(r, \theta)$) given by

$$I_{Ei}(r, \theta) = I(r, \theta) \otimes H_i(r, \theta). \quad (1)$$

A thresholding process is then applied to the eight edge images using a threshold value equal to the highest N -percentile of the pixels. Edge image pixels whose intensity levels are higher than the threshold are assigned the value of 1, and the remaining pixels take the value of 0. The process results in eight thresholded edge images $I_{Ti}(r, \theta)$. Subsequently, an overall edge image $I_F(r, \theta)$ is obtained by combining the eight thresholded edge images $I_{Ti}(r, \theta)$ and a filtering process given by [15]

$$I_T(r, \theta) = \sum_{i=1}^8 I_{Ti}(r, \theta), \quad (2)$$

$$I_F(r, \theta) = \begin{cases} 1, & I_T(r, \theta) \in [1, \tau_F] \\ 0, & \text{otherwise.} \end{cases} \quad (3)$$

The filtering is implemented to remove the single pixel noise that has edges in more than τ_F directions.

Using the raw radar image pixels corresponding to the pixels of intensity value of 1 in $I_F(r, \theta)$, a statistical distribution $F_H(\eta)$ of gray level values η is created. From the distribution, the gray level threshold τ_S used to identify shadow can be determined as [15]

$$\tau_S = \text{mode}(F_H(\eta)). \quad (4)$$

2.1.2. Calculating Illumination Ratio. Using the shadow threshold τ_S determined in Section 2.1.1, the shadow image can be derived. Pixels with the values less than τ_S are regarded as shadowed, and the remaining pixels are understood to be illuminated. Next, the shadow image is divided into segments along the range r and the azimuth θ , and the illumination ratio $L(\gamma)$ as a function of grazing angle γ for each segment is calculated [15].

2.1.3. Estimating RMS Surface Slope. Having obtained the illumination ratios for each azimuth direction, the RMS surface slope σ_{RMS} of a random rough surface described by a one-dimensional Gaussian surface height probability density function (PDF) can be derived by curve-fitting Smith's function [16] for that direction. The curve fitting is implemented by the Neidler-Mead simplex method in one dimension [18]. After deriving σ_{RMS} for all azimuth angles, an average RMS surface slope σ_{RMS}^A can be calculated.

2.1.4. Estimating Significant Wave Height. Finally, from the average RMS surface slope σ_{RMS}^A and the average zero-crossing wave period T_{m02} , the significant wave height H_{m0} can be determined as in [15] by

$$H_{m0} = \frac{\sigma_{\text{RMS}}^A g T_{m02}^2}{\sqrt{2\pi}}, \quad (5)$$

where g is the gravitational acceleration. T_{m02} can be derived from the radar images themselves using existing wave algorithms [1–5]. However, the average zero-crossing wave period T_{m02} measured by well-accepted buoy data instead of radar was used here since the radar employed in this study did not produce a good value for T_{m02} .

2.2. Modification

2.2.1. Data Quality Control. Before processing the raw radar data, low quality images, such as rain-contaminated or low-backscatter cases, should be discarded. The data quality control procedure described in [19] is employed here.

Rain leads to the change of the normalized radar cross section (NRCS) and significantly affects wave height retrieval. Due to the strong impact of rain on the number of zero-intensity pixels in X-band nautical radar images, the zero-pixel percentage (ZPP), which is defined as the ratio of the number of zero-intensity pixels to the total number of pixels in an image, is identified as a parameter for rain recognition [20]. For the data used here, pixels with gray scale intensity lower than 5 are regarded as zero-intensity pixels [19]. Images with ZPP less than 10% are considered as rain-contaminated and are not used for wave height retrieval.

Low-backscatter images that appear almost completely black due to low wind speed or unknown system errors contain little or no wave information. A parameter called low-clutter direction percentage (LCDP), which is defined as the ratio of the number of low-clutter directions to total number of directions in an image, is used for identifying low-backscatter images [19]. If the ZPP of a single azimuth direction is higher than 40% (empirical and also varies with systems), the direction is regarded as a low-clutter direction. Then, the images with LCDP higher than 90% are excluded from subsequent processing.

2.2.2. Edge Pixel Intensity Histogram Smoothing. In [15], the shadow threshold is directly determined as the intensity value corresponding to the highest occurrence of the intensity histogram of edge pixels. This is viable if the distribution

is smooth. However, the data used in this work has a small gray scale depth (8-bit, i.e., 0–255) and a relatively small number of pixels. The shadow threshold may not be correctly determined by seeking the highest occurrence of the histogram. In order to improve the accuracy of shadow threshold determination, a smoothing process using a spline function is applied to the edge pixel intensity histogram. The smoothing spline function [21], s , minimizes

$$p \sum_{\eta_i=1}^n \left(F_H(\eta_i) - s\left(\frac{\eta_i}{n}\right) \right)^2 + \int_0^1 \left(\frac{d^2 s(\tau)}{d\tau^2} \right)^2 d\tau, \quad (6)$$

where p is the smoothing parameter determining the tradeoff between fidelity to the data and smoothness of the function. When p approaches 0, the function converges to a simple linear least squares regression. When p approaches infinity, the function converges to the interpolating spline. Here, p is selected as 9 since the tendency can be maintained and the outlier of the distribution can be removed with this choice. This smoothing process is performed using the MATLAB built-in curve-fitting function “fit”. It should be noted that other smoothing methods (e.g., moving average, median filtering) can remove outliers but may change the details of the tendency of a distribution. Thus, an inaccurate mode of the edge pixel intensity histogram may be obtained, leading to an inaccurate shadow threshold. However, the spline function does not cause such a problem. The shadow threshold is estimated from the smoothed intensity histogram.

2.2.3. Subareas Selection. In [15], all the azimuth directions in the shadow image were used for the derivation of the average RMS surface slope. However, the image portion in the azimuths far from the upwind direction usually has low sea clutter intensities and overestimated shadowed areas. Including such a portion may result in wave height overestimation. Here, for each shadow image, only a subarea selected from the portion $\pm 5^\circ$ around the upwind direction is used for RMS surface slope estimations since the clutter signal is stronger in those directions and more robust results may be obtained. The technique for determining the upwind direction is based on a dual-curve-fitting algorithm found in [19]. Then, a RMS surface slope is derived from the subarea for each image. Moreover, an average RMS surface slope is calculated using a time sequence of images instead of all the subareas in a single image. Since the RMS surface slope is calculated from the portion around the upwind direction in each single image, the variation of RMS surface slope obtained from the upwind direction is negligible between consecutive images. Thus, it does not require two consecutive radar images to be perfectly overlapped, and the ship motion will not affect the result significantly. As with most existing works on the topic, a typical value of 32 images is used here to obtain an average RMS surface slope for wave height estimation.

3. Results

3.1. Data Overview. In order to test the modified method, data provided by Defence Research and Development

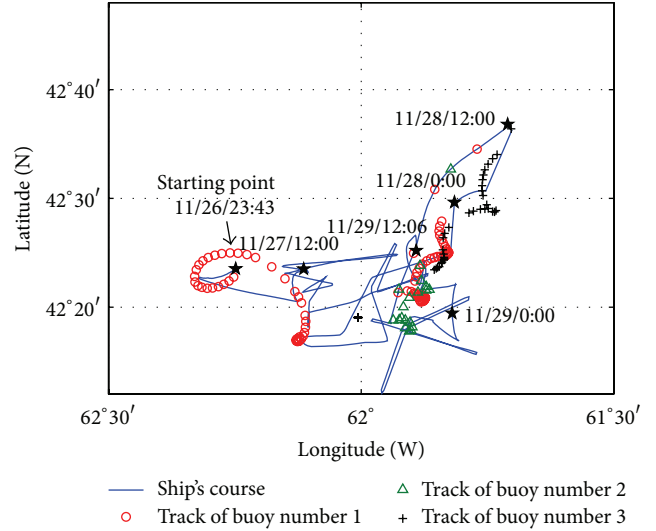


FIGURE 1: Ship's course and track of buoys from 23:43 November 26 UTC to 12:06 November 29 UTC (2008), and every half a day is marked by a black star.

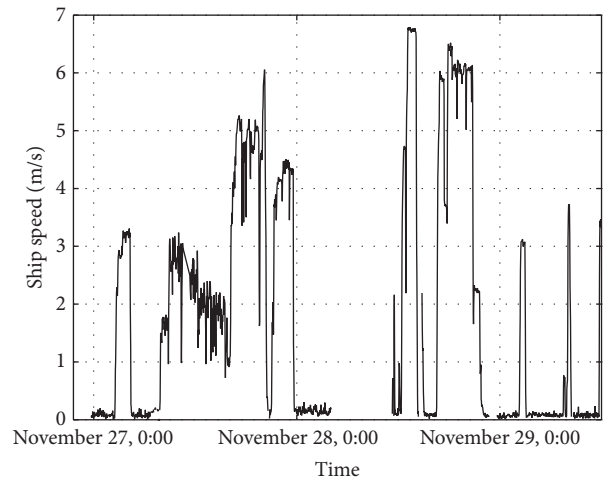


FIGURE 2: Time sequence of ship speed throughout the sea trial.

Canada (DRDC) is used. The data was collected from 23:43 November 26 to 12:06 November 29 (2008), in a sea trial approximately 300 km south-southeast of Halifax, Nova Scotia, Canada. Three free-floating Triaxys directional wave buoys were deployed about 4 to 15 km apart to measure the wave field. The distances between the ship and the buoys were generally less than 10 km, but occasionally up to 15 km throughout the trial. The water depth around the ship and the buoys is about 200 m. Figure 1 depicts the ship's course and the track of the three wave buoys. Figure 2 displays the time sequence of ship speed throughout the sea trial.

The radar utilized in the sea trial was a standard HH-polarized Decca marine radar which operated at 9.41 GHz with a sampling frequency of 20 MHz. The radar covered 360° in azimuth with a beam width of 2° and an antenna rotation speed of 28 rpm. The antenna was installed at a

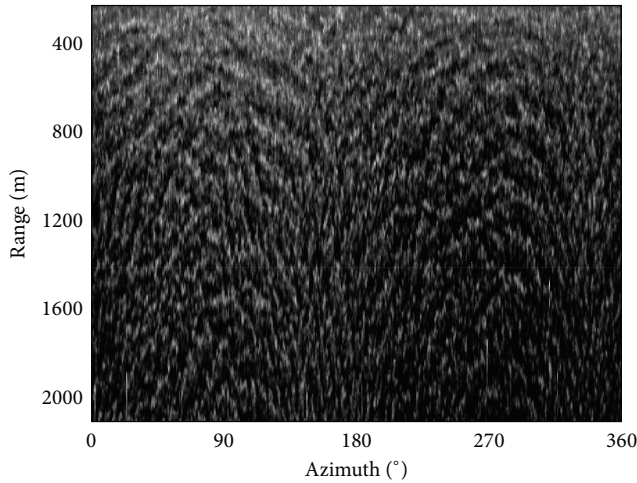


FIGURE 3: B-scan raw radar image.

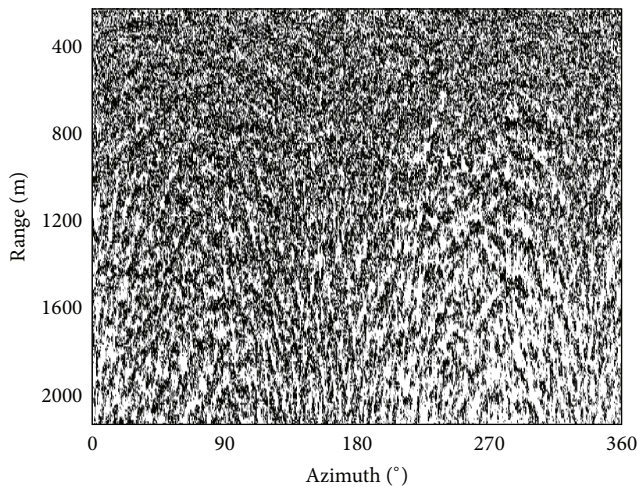


FIGURE 4: Edge image. Edges are black.

height of 21.9 m above the sea level, covering a range from 240 m to 2160 m with a range resolution of 7.5 m. The radar was connected to a Wave Monitoring System II (WaMoS II) [22]. As indicated in Section 2.2.2, the system scaled and stored the radar backscatter power in gray levels from 0 to 255 (8-bit unsigned integers), with 0 corresponding to lowest radar return (black colour in the radar image) and 255 to the maximum radar return (white colour in the radar image).

3.2. Experimental Results. One example of the B-scan (i.e., polar coordinate) raw radar image is shown in Figure 3. The corresponding edge image obtained by edge detection and filtering is depicted in Figure 4, in which edges are shown in black. The threshold values used for the edge detection and filtering in this study are 20% and 5 (τ_F in (3)), respectively. The requirement of a higher threshold for the edge detection than that (10%) in [15] in order to produce robust results was likely due to the different operational parameters including lower antenna height and

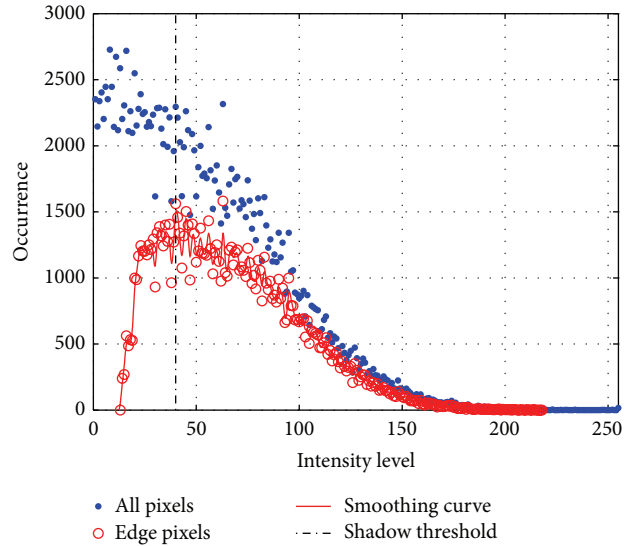


FIGURE 5: Intensity distribution of edge pixels and all image pixels. Smoothed histogram is indicated by solid line and shadow threshold is illustrated by dash-dots.

lower range and azimuth resolutions used here. In [23], an additional filtering process with a constant threshold was introduced to remove those edges located too far away from shadow in order to obtain the reasonable shadow threshold from the edge pixel intensity histogram. However, from the result in [23], it can be seen that filtering with a constant threshold was not robust to variation in sea state. Here, the smoothing process is used instead. The intensity distributions of the edge pixels (red circles), along with the spline-fitted curve (red line), and the entire set of image pixels (blue points) for the image in Figure 3 are shown in Figure 5, in which pixels with zero intensity level are excluded, and the gray level shadow threshold is illustrated by the dash-dot. Note that if no smoothing is used, the shadow threshold will be determined by the outlier for the histogram curve, corresponding to the level intensity of 63 rather than a correct value (40 in Figure 5). It should also be noted that the shadow threshold is estimated for each image. Thus, the ship motion does not have a significant effect on the shadow threshold estimation. After thresholding the raw image in Figure 3, the corresponding shadow image is obtained and shown in Figure 6. In that figure, shadowed areas are shown as black and the subarea used for RMS surface slope calculation is the portion between the dashes-dots. Figure 7 depicts the illumination ratio as a function of grazing angle and the corresponding Smith's function fit for one single subarea (the portion between the dashes-dots in Figure 6). The RMS surface slope σ_{RMS} is estimated by the curve fitting. The threshold that distinguishes the usable data and eliminated data in Figure 7 is sought by gradually eliminating the illumination ratio data used for the σ_{RMS} calculation from the longest range towards the direction of decreasing ranges (i.e., increasing grazing angles). This threshold is determined as the range beyond which the corresponding illumination ratio data is excluded from calculating σ_{RMS} and the σ_{RMS}

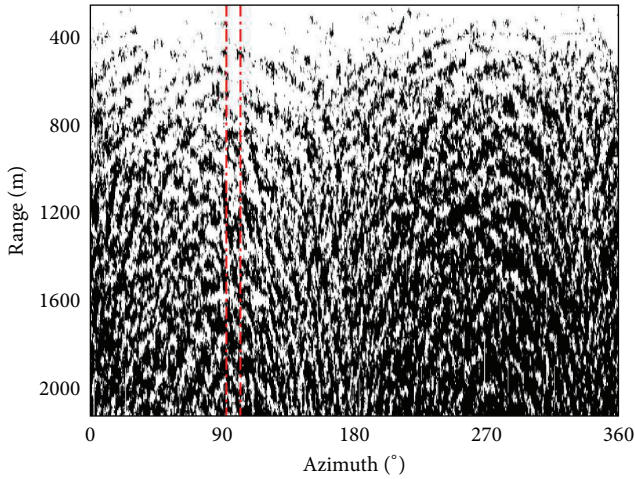


FIGURE 6: Shadow image. Shadowed areas are black. Subarea is the portion between the dash-dots.

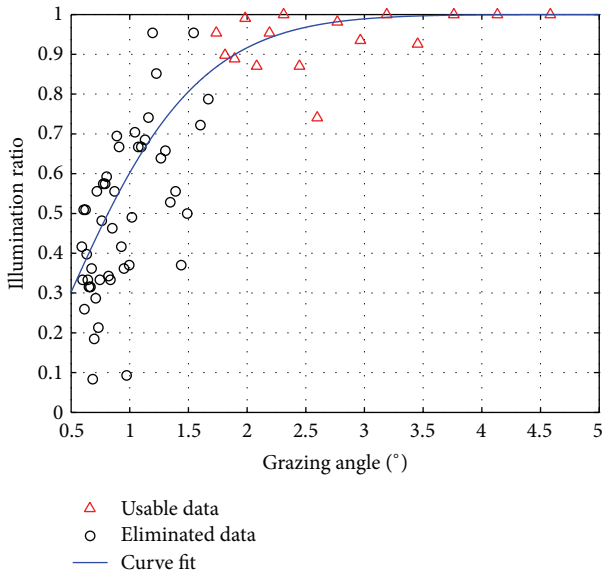


FIGURE 7: Illumination ratio as a function of grazing angle and curve fitted Smith's function for one single subarea.

obtained from the remaining data is the smallest [15]. This is done because the radar backscatter from long ranges may be weak simply due to the decay law for the electromagnetic energy. This causes an overestimation of shadowed areas at long ranges, leading to a corresponding overestimated σ_{RMS} and wave height.

The original and modified shadowing-based algorithms described above are both applied to the quality-controlled Decca radar data, and the results are compared with the reference data measured by the buoys. The comparison of the time sequences of significant wave heights is displayed in Figure 8. It should be noted that a storm appeared between 2:30 and 12:00 on November 28, and radar data was not recorded for most of this period. Moreover, low quality images were discarded by the data quality control process.

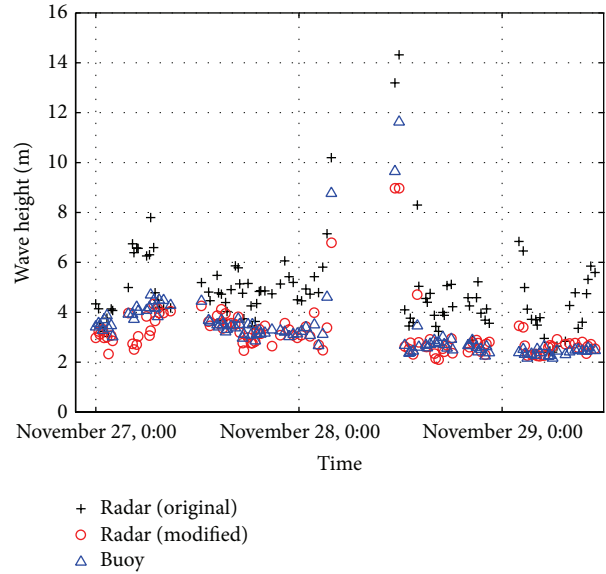


FIGURE 8: Comparison of the time sequences of significant wave heights derived by the original and the modified shadowing-based algorithm and buoys.

It can be observed that the wave heights obtained using the original algorithm are consistently overestimated. The overestimation is mainly due to the overestimated shadow threshold caused by the outliers in the intensity distribution of the edge pixels (see Figure 5). However, the radar results derived from the modified algorithm agree well with the buoy data for most of the period. Differences are observed over some periods. The wave heights were underestimated from 4:20 to 6:30 on November 27 and overestimated from 2:00 to 2:30 on November 29. During these periods, light rain and relatively low wind speed occurred. These conditions were not detected by the data quality control process. Since rain enhanced the image intensity, shadowed areas were reduced. Thus, wave heights were underestimated. However, low wind speed resulted in overestimation of shadowed areas and wave heights. From 2:50 to 3:50 and from 11:20 to 11:50 on November 28, wave heights were high but also underestimated. During this period, a strong swell signature was observed in addition to the wind wave component. An example of the wave frequency spectrum derived from buoy data during this period is given in Figure 9, in which the dual-mode wave field is clearly seen. The peak frequency in Figure 9 is 0.03 Hz which corresponds to a swell wave period of 33.3 s. Therefore, wave height estimation for such a complex sea state needs to be further analyzed. The corresponding scatter plots of the retrieved significant wave heights using the original and modified algorithms with the reference data are shown in Figures 10(a) and 10(b), respectively. With the modification, the correlation coefficient is increased from 0.81 to 0.91, and the RMS difference is reduced significantly from 1.82 m to 0.59 m. By excluding the data with buoy-recorded wave heights larger than 8 m, the correlation coefficients between the buoy-recorded and radar-derived wave heights are 0.47

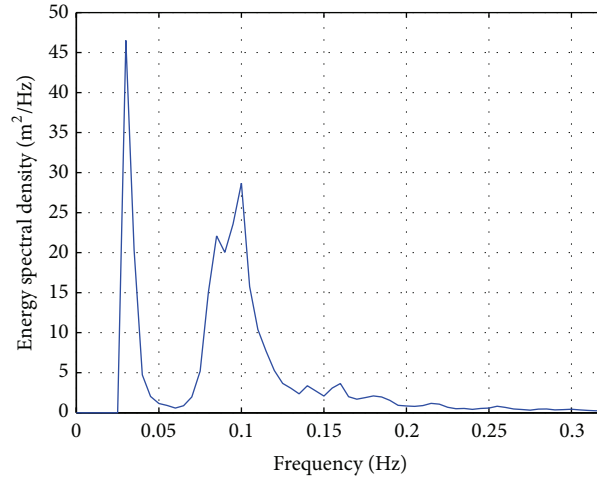


FIGURE 9: Wave frequency spectrum containing wind wave and strong swell components.

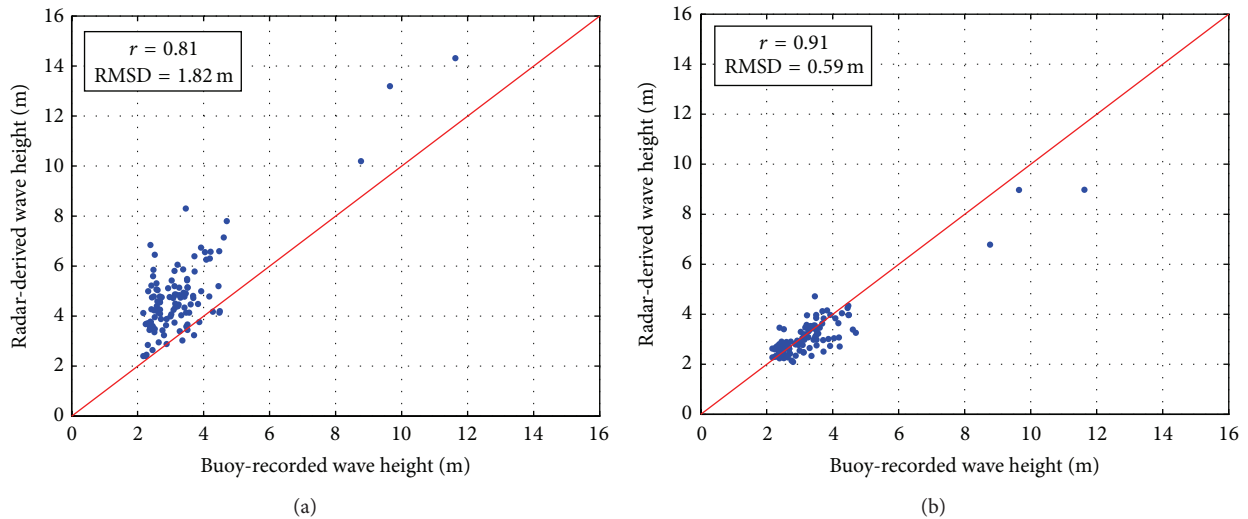


FIGURE 10: Scatter plots of significant wave heights comparing with reference data: (a) original algorithm; (b) modified algorithm.

and 0.68, respectively, for the original and modified algorithms. The corresponding RMS differences are 1.79 m and 0.50 m, respectively.

4. Conclusions and Outlook

In this paper, a modified shadowing-analysis-based wave height estimation method has been applied to X-band nautical radar data. The modifications include (1) a data quality control process to exclude rain cases and low-backscatter images; (2) a scheme for smoothing the edge pixel intensity histogram to determine shadow threshold; and (3) employing of a time sequence of subareas around the upwind direction to calculate the average RMS surface slope. By comparing the radar-derived results and the buoy-measured data, it has been found that the wave height retrieved from the algorithm is underestimated under rain and storm conditions and overestimated under low wind speed. Still, the proposed method produces promising results, with a RMS difference of

0.59 m and a correlation coefficient of 0.91. However, in order to improve the robustness of this wave height algorithm, the effects of rain, low wind speed, and storm conditions with dual-mode wave fields need to be further analyzed. This will be more intensively investigated in the next phase of the work. Moreover, the algorithm needs to be further validated using radar data that can produce good estimation of average zero-crossing wave periods to make it completely independent of external sensors.

Conflict of Interests

The authors declare that there is no conflict of interests regarding the publication of this paper.

Acknowledgments

The work was supported in part by Natural Sciences and Engineering Research Council of Canada (NSERC) under

grants to Weimin Huang (NSERC 402313-2012) and Eric W. Gill (NSERC RGPIN-2015-05289) and by an Atlantic Innovation Fund Award (Eric W. Gill, Principal Investigator). The work was also supported by the Department of Innovation, Business and Rural Development of Newfoundland and Labrador under Grant 30-10921-008. In addition, The authors would like to thank Dr. E. Thornhill at Defence Research and Development Canada (DRDC) for the provision of the radar and buoy data.

References

- [1] K. G. Hessner, J. C. Nieto-Borge, and P. S. Bell, "Nautical radar measurements in Europe: applications of WaMoS II as a sensor for sea state, current and bathymetry," in *Remote Sensing of the European Seas*, pp. 435–446, Springer, Dordrecht, The Netherlands, 2008.
- [2] J. C. Nieto-Borge, G. Rodríguez-Rodríguez, K. Hessner, and P. I. Izquierdo-González, "Inversion of marine radar images for surface wave analysis," *Journal of Atmospheric and Oceanic Technology*, vol. 21, no. 8, pp. 1291–1300, 2004.
- [3] I. R. Young, W. Rosenthal, and F. Ziemer, "A three-dimensional analysis of marine radar images for the determination of ocean wave directionality and surface currents," *Journal of Geophysical Research*, vol. 90, no. 1, pp. 1049–1059, 1985.
- [4] P. Izquierdo, C. Guedes-Soares, J. C. Nieto-Borge, and G. R. Rodríguez, "A comparison of sea-state parameters from nautical radar images and buoy data," *Ocean Engineering*, vol. 31, no. 17–18, pp. 2209–2225, 2004.
- [5] J. C. N. Borge, K. Reichert, and J. Dittmer, "Use of nautical radar as a wave monitoring instrument," *Coastal Engineering*, vol. 37, no. 3–4, pp. 331–342, 1999.
- [6] J. C. Nieto-Borge, K. Hessner, P. Jarabo-Amores, and D. de la Mata-Moya, "Signal-to-noise ratio analysis to estimate ocean wave heights from X-band marine radar image time series," *IET Radar, Sonar & Navigation*, vol. 2, no. 1, pp. 35–41, 2008.
- [7] J. Seemann, F. Ziemer, and C. M. Senet, "Method for computing calibrated ocean wave spectra from measurements with a nautical X-band radar," in *Proceedings of the MTS/IEEE Conference (OCEANS '97)*, vol. 2, pp. 1148–1154, Halifax, Canada, October 1997.
- [8] L. B. Wetzel, "Electromagnetic scattering from the sea at low grazing angles," in *Surface Waves and Fluxes*, pp. 109–172, Kluwer, Boston, Mass, USA, 1990.
- [9] J. R. Buckley and J. Aler, "Estimation of ocean wave height from grazing incidence microwave backscatter," in *Proceedings of the IEEE International Geoscience and Remote Sensing Symposium (IGARSS '97)*, vol. 2, pp. 1015–1017, Singapore, August 1997.
- [10] J. R. Buckley and J. Aler, "Enhancements in the determination of ocean surface wave height from grazing incidence microwave backscatter," in *Proceedings of the IEEE International Geoscience and Remote Sensing Symposium (IGARSS '98)*, vol. 5, pp. 2487–2489, IEEE, Seattle, Wash, USA, July 1998.
- [11] R. Gangeskar, "Wave height derived by texture analysis of X-band radar sea surface images," in *Proceedings of the International Geoscience and Remote Sensing Symposium (IGARSS '00)*, vol. 7, pp. 2952–2959, IEEE, Honolulu, Hawaii, USA, July 2000.
- [12] R. Gangeskar, "Adaptive method for estimation of wave height based on statistics of sea surface images," in *Proceedings of the IEEE International Geoscience and Remote Sensing Symposium (IGARSS '00)*, vol. 1, pp. 255–259, Honolulu, Hawaii, USA, July 2000.
- [13] W. Huang, E. W. Gill, and J. An, "Iterative least-squares-based wave measurement using X-band nautical radar," *IET Radar, Sonar & Navigation*, vol. 8, no. 8, pp. 853–863, 2014.
- [14] J. An, W. Huang, and E. W. Gill, "A self-adaptive wavelet-based algorithm for wave measurement using nautical radar," *IEEE Transactions on Geoscience and Remote Sensing*, vol. 53, no. 1, pp. 567–577, 2015.
- [15] R. Gangeskar, "An algorithm for estimation of wave height from shadowing in X-band radar sea surface images," *IEEE Transactions on Geoscience and Remote Sensing*, vol. 52, no. 6, pp. 3373–3381, 2014.
- [16] B. G. Smith, "Geometrical shadowing of a random rough surface," *IEEE Transactions on Antennas and Propagation*, vol. 15, no. 5, pp. 668–671, 1967.
- [17] W. K. Pratt, *Digital Image Processing*, Wiley, Hoboken, NJ, USA, 1991.
- [18] J. C. Lagarias, J. A. Reeds, M. H. Wright, and P. E. Wright, "Convergence properties of the Nelder-Mead simplex method in low dimensions," *SIAM Journal on Optimization*, vol. 9, no. 1, pp. 112–147, 1998.
- [19] Y. Liu, W. Huang, E. W. Gill, D. K. Peters, and R. Vicen-Bueno, "Comparison of algorithms for wind parameters extraction from shipborne X-band marine radar images," *IEEE Journal of Selected Topics in Applied Earth Observations and Remote Sensing*, vol. 8, no. 2, pp. 896–906, 2015.
- [20] B. Lund, H. C. Graber, and R. Romeiser, "Wind retrieval from shipborne nautical X-band radar data," *IEEE Transactions on Geoscience and Remote Sensing*, vol. 50, no. 10, pp. 3800–3811, 2012.
- [21] H. L. Weinert, *Fast Compact Algorithms and Software for Spline Smoothing*, Springer, Baltimore, Md, USA, 2013.
- [22] *WaMoS II Wave and Surface Current Monitoring System Operating Manual Version 4.0*, OceanWaveS GmbH, Lüneburg, Germany, 2012.
- [23] X. Liu, W. Huang, and E. W. Gill, "Shadowing-analysis-based wave height measurement from ship-borne X-band nautical radar images," in *Proceedings of the MTS/IEEE OCEANS Conference*, Genova, Italy, May 2015.